Instrumentation: Nondestructive Examination for Verification of Canister and Cladding Integrity – FY2014 Status Update

Fuel Cycle Research & Development

Prepared for
U.S. Department of Energy
Used Fuel Disposition Campaign

RM Meyer
JD Suter
AM Jones
RA Mathews

September 12, 2014

FCRD-UFD-2014-000308

PNNL-23600

Reviewed by:

Project Manager   _____
                                                        Name

SUMMARY

This report documents FY2014 efforts to 1) develop nondestructive evaluation (NDE) methods and techniques to verify the integrity of metal canisters for the storage of used nuclear fuel (UNF) and 2) to verify the integrity of internals of dry storage systems.

The first effort focused on developing a multi-frequency eddy current technique for depth sizing of stress corrosion cracks in the confinement boundary (stainless steel canisters). In FY2014, this effort focused on laboratory measurements to validated finite element modeling (FEM) analysis performed in FY2013. In addition, an overview of advanced eddy current instrumentation and concepts was performed to identify potential concepts that could be anticipated to have improved performance over the single coil absolute probe that has been the subject of investigation so far.

The multi-frequency eddy current measurement results presented in this report provide a validation of FEM efforts in FY2013 as measurement data exhibits similar shapes and features as the FEM results. Measurement data was collected on specimens containing sawcut notch defects, electrical discharge machining (EDM) notch defects, and thermal fatigue cracks. A comparison of measurement data obtained from EDM notches with thermal fatigue cracks indicate that the depth of one crack is 3 mm–4 mm and the depth of a second crack is between 4 mm and 7 mm. A comparison of measurement data with the conclusions made based on FEM analysis conducted in FY2013 indicates that the thermal fatigue cracks have a very low effective conductivity, although it is probably not 0%.

An overview is also provided of advanced eddy current instrumentation and concepts in an effort to identify alternative technologies that could result in improved performance. The overview considered different pickup sensor types such as Hall-effect, giant magneto resistive (GMR), and superconducting quantum interference devices. These sensors can provide improved field sensitivity, spatial resolution, and sensitivity to field direction. In addition, advanced concepts are considered, such as pulsed eddy current and eddy current probes with more complex sensor configurations in comparison to the single coil absolute probe that has been the subject of FEM and laboratory assessment. The overview highlights the diversity of eddy current probe concepts and configurations and that eddy current probe design is at least partially an "art." The documented information on environmental tolerance of pickup sensors indicates that Hall effect sensors and GMR sensors exist that should be able to tolerate the temperatures near dry storage canisters. Documentation of radiation tolerance of GMR sensors indicates that they should also be able to survive the gamma radiation. For Hall effect sensors, it is less clear, although specifications for radiation-tolerant Hall sensors indicate that they are insensitive to gamma radiation.

Suggestions for future efforts related to development of an eddy current technology for depth sizing stress corrosion cracks in dry storage canisters include:

- Determine the true state of thermal fatigue cracks for comparison to predictions of crack depth documented here.

**Instrumentation: Nondestructive Examination for Verification of Canister and Cladding Integrity –
FY2014 Status Update**

iv   September 12, 2014

- Collect multi-frequency data on specimens with stress corrosion cracking (SCC). Data obtained to date on thermal fatigue cracks is encouraging, but thermal fatigue cracks are expected to produce eddy current responses that are distinct from SCC. Although SCC and thermal fatigue flaws are similar in that they both can be characterized by a small crack opening displacement, the surface of the crack face for thermal fatigue cracks is smooth, whereas the surface of the crack face for SCC is rough. Thus, there tends to be greater contact between the crack faces of SCC and greater effective conductivity.

- Extend assessment of multi-frequency eddy current technique for crack depth sizing by considering a wider range of frequencies (i.e., greater than 100 kHz).

- Begin to design and assess advanced eddy current probe concepts for sizing, such as probes consisting of multiple Hall-effect or GMR pickup sensors and pulsed eddy current concepts.

The second effort related to the development of techniques to verify the integrity of internals of dry storage systems was limited to proposing a concept for monitoring the integrity of the inside of dry storage canisters in response to a dry storage instrumentation workshop following the Electric Power Research Institute's Extended Storage Collaboration Program meeting in Charlotte, North Carolina, in December 2013. This concept proposed passive optical monitoring of fission gas and water vapor impurities in dry storage casks based on excitation of the gas by gamma rays from the fuel bundles. A feasibility analysis was performed and presented at the American Nuclear Society summer meeting in Reno, Nevada, June 2014. The conference paper is included as Appendix A.

CONTENTS

FIGURES

TABLES

ACRONYMS

AC	alternating current
ANS	American Nuclear Society
COD	crack opening displacement
DOE	U.S. Department of Energy
ECT	eddy current testing
EPRI	Electric Power Research Institute
FEM	finite element modeling
GMR	giant magneto resistive
HDRP	High Burnup Dry Storage Cask Research and Development Project
NDE	nondestructive evaluation
NRC	U.S. Nuclear Regulatory Commission
PEC	pulsed eddy current
SCC	stress corrosion cracking
SFEC	swept-frequency eddy current
SQUID	superconducting quantum interference device
UFDC	Used Fuel Disposition Campaign
UNF	used nuclear fuel

Instrumentation: Nondestructive Examination for Verification of Canister and Cladding Integrity – FY2014 Status Update

1.   INTRODUCTION

The storage and transportation task has been created within the Used Fuel Disposition Campaign (UFDC), to address issues of extended or long-term storage and transportation. The near-term objectives of the storage and transportation task are to use a science-based, engineering-driven approach to:

- develop the technical bases to support the continued safe and secure storage of used nuclear fuel (UNF) for extended periods

- develop the technical bases for retrieval of UNF after extended storage

- develop the technical bases for transport of high burn-up fuel, as well as low and high burn-up fuel after dry storage.

This report documents 1) FY2014 efforts to develop nondestructive evaluation (NDE) methods and techniques to verify the integrity of metal canisters for the storage of UNF and 2) to verify the integrity of internals of dry storage systems.

1.1   NDE for Canister Integrity

Under the former task (FEM modelling effort in 2013), efforts have focused on developing a multi-frequency eddy current technique for depth sizing of stress corrosion cracks in the confinement boundary (stainless steel canisters used to store UNF). The ability to depth size detected flaws in-situ would have significant positive impact on the safety and economics of extended used fuel storage. In FY12, a review of several NDE technologies was performed for potentially monitoring the degradation of stainless steel canisters by stress corrosion cracking (SCC). Several techniques were reviewed including visual, eddy current, bulk ultrasound, guided wave ultrasound, and acoustic emission (Meyer et al. 2013c). An assessment of NDE for dry storage canisters documents some of the requirements of instrumentation such as the environmental (i.e., temperature, radiation) constraints as well as the accessibility and deployment constraints. In addition, this report summarized previous performance assessments involving bulk ultrasound and eddy current techniques (Meyer et al. 2013b). The eddy current technique is already used for inspections in nuclear power plants and is more sensitive to shallow flaws than bulk ultrasound techniques. However, the skin effect of electromagnetic waves has tended to relegate the eddy current technique to applications involving the detection of surface-breaking flaws or shallow subsurface defects. Techniques involving the propagation of bulk ultrasound are primarily used for depth sizing of flaws in reactor components. However, the ability to depth size defects using eddy current techniques would have significant benefit over

bulk ultrasound for this application as eddy current does not require the application of a material for coupling to implement and the transducers can be made compact and rugged.

These efforts have focused on the development of a multi-frequency eddy current technique for depth sizing using a single coil absolute probe. In FY2014, efforts have focused mostly on laboratory activities to help validate finite element modeling (FEM) performed in FY2013, which are documented in the FY2013 status report (Meyer et al. 2013a) and a NACE Corrosion conference paper (Meyer et al. 2014). In addition, some effort was devoted to reviewing advanced eddy current probe configurations and concepts, in an effort to identify concepts that may improve upon the single coil absolute probe configuration that has thus far been the subject of analysis.

1.2   Instrumentation to Monitor Integrity of Internals

In December 2013, multiple laboratory participants were invited, along with personnel from industry and the U.S. Nuclear Regulatory Commission (NRC), to a workshop to discuss potential concepts for improved monitoring of gas impurities (i.e., fission gases, water vapor, and hydrogen) in the Electric Power Research Institute (EPRI)/U.S. Department of Energy (DOE) High Burnup Dry Storage Cask Research and Development Project (HDRP) (Marschman 2014). In support of this effort, a concept was proposed for passive optical monitoring of gas impurities.

1.3   Structure of the Report

The rest of this report is organized into four sections with Section 2 devoted to briefly summarizing the passive optical monitoring concept proposed for monitoring the integrity of internals components. Section 3 summarizes the FEM validation efforts, describing the probes that have been fabricated, specimens, and data collection and analysis procedure. Section 4 includes the review of advanced eddy current probe configurations and concepts, while Section 5 provides some conclusions and suggestions for future work on developing an eddy current technique for sizing of stress corrosion cracks in dry storage canisters. Referenced are included in Section 6.

2.   PASSIVE OPTICAL MONITORING OF INTERNAL INTEGRITY

This section summarizes a concept for monitoring of the integrity inside of dry storage canisters, which was introduced at a workshop following the EPRI Extended Storage Collaboration Program (ESCP) meeting in Charlotte, North Carolina, in December 2013 (Marschman 2014). This concept proposes passive optical monitoring of fission gas and water vapor impurities in dry storage casks based on excitation of the gas by gamma rays from the fuel bundles (see Figure 2-1). For implementation of the concept, a brazed sapphire window viewport is proposed for incorporation into the lid of the monitored cask. The brazed sapphire window was selected because of its resilience to the environmental conditions anticipated (temperature and radiation). To mitigate the risk of window breakage or seal leaking, a redundant seal design is proposed. The proposed concept is advantageous in that it requires no gas sampling, and the monitoring is performed in situ. In addition, it is conceivable that the technique could be implemented to monitor in continuous fashion, minimizing worker exposure. More details of the concept, along with a feasibility analysis, were presented at the American Nuclear Society (ANS) summer meeting in Reno, Nevada, June 2014. The conference paper is included as Appendix A.
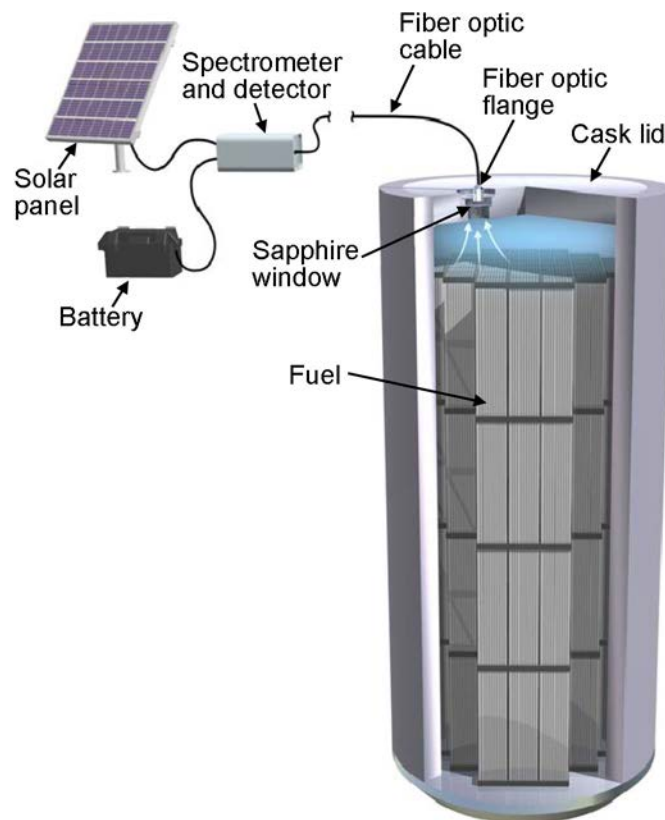

Figure 2-1.   Illustration of Passive Optical Monitoring of Gas Impurities Inside of Dry Storage Cask System

3. EDDY CURRENT FOR DEPTH SIZING

Eddy current methods are being investigated to depth size defects in dry storage canisters as an alternative to conventional depth sizing using ultrasonic techniques. In FY2013, computer modeling was performed (FEM) in an effort to identify features from multi-frequency eddy current signals that could be used for depth sizing (Meyer et al. 2013a). In this case, FEM revealed potential features in curves of the magnitude of the change in impedance due to a defect, $|\Delta Z|$, the change in resistance, ΔR, and the phase of the change in impedance, $\angle \Delta Z$. For FY2014, efforts shifted toward laboratory activities to validate the FEM results and verify such features could be observed in practice. These efforts are documented in the following subsections, including a description of the fabricated probes, specimens used for testing, the data collection and analysis procedure, and the results.

3.1 Probe Descriptions

Several absolute probes were fabricated for the purpose of validating the FEM results for the multi-frequency technique. In this case, probes with air cores (no internal material in coil winding) and ferrite cores (ferrite material in the coil winding to focus magnetic field) were built with resonant frequencies for each at 20 kHz and 50 kHz. Specifications for the probes are provided in Table 3-1. Specifications include the wire gauge, number of turns, coil height, coil width, coil diameter, core diameter, core permeability, coil resistance, and coil inductance. Photographs of probes with ferrite cores and air cores are provided in Figures 3-1 and 3-2. Radiographic images of the probes, in Figure 3-3, show the anatomy of the probes. The air core probes are in the top of Figure 3-3 and show the electrical connector, wires, and two coils. In this case, the coils nearest to the connectors are reference coils and coils farther away from the connectors are the sensing coils, which are visible in Figure 3-2. The ferrite core probes are displayed in the bottom half of Figure 3-3. They are the same as the air core probes except they include ferrite shields surrounding the reference coils and the sensing coils. Also, the reference coils are able to be located closer to the sensing coils because of the ferrite shielding.

Table 3-1.   Specifications for "Standard" Eddy Current Probes Fabricated with Air Cores and Ferrite Cores and at Resonant Frequencies of 20 kHz and 50 kHz for Each Design

	Standard Probes			
	20-kHz Ferrite Core	50-kHz Ferrite Core	20-kHz Air Core	50-kHz Air Core
Wire Gauge	30	28	30	28
# of Turns	96	60	230	148
Coil Height	0.200 in.	0.200 in.	0.118 in.	0.118 in.
Coil Width	0.15 in.	0.15 in.	0.3 in.	0.3 in.
Coil Diameter	0.500 in.	0.5 in.	0.700 in.	0.740 in.
Gap Diameter	0.325 in.	0.325 in.	0.15 in.	0.15 in.
Core Permeability	1500	1500	1	1
Coil Resistance	105 Ω	62 Ω	113 Ω	70 Ω
Coil Inductance	428 μH	160 μH	373 μH	135 μH
H = Henries, Ω = ohms				

Figure 3-1.   Photograph of Standard Absolute Ferrite Core Probes with Resonant Frequencies
                of 20 kHz and 50 kHz
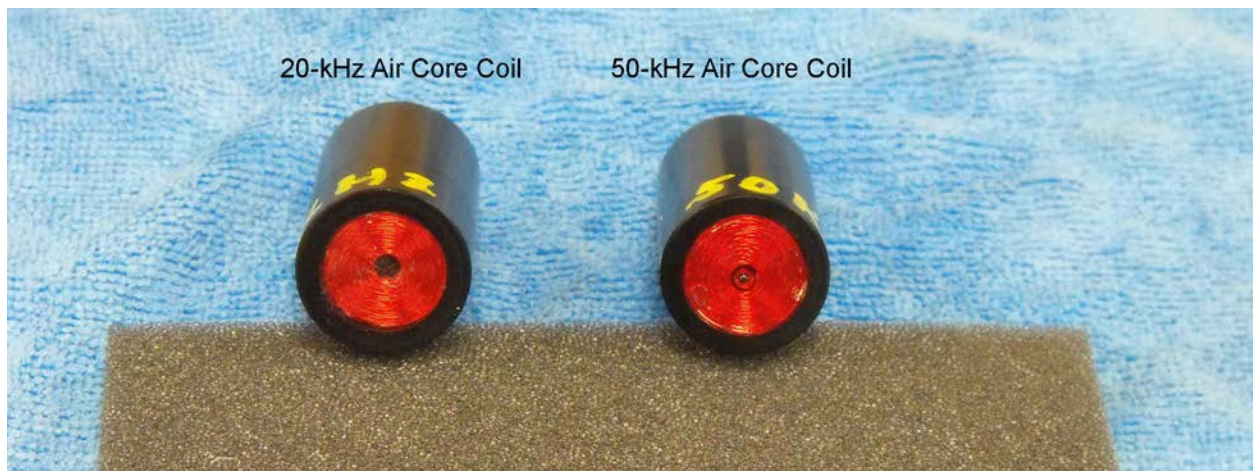
Figure 3-2.   Photograph of Standard Absolute Air Core Probes with Resonant Frequencies of
                20 kHz and 50 kHz

In addition to the standard probes, smaller ferrite core probes were also fabricated with the same
basic coil dimensions as in the larger standard probes, but with much smaller packaging
(Table 3-2). These were fabricated to show that the probe concept could be fabricated in a
compact package that would allow it to access the surface of dry storage canisters. A photograph
of these probes is included in Figure 3-4. The height of these probes is 0.5 in., the width is also
0.5 in., and the length is 1.0 in.

Instrumentation: Nondestructive Examination for Verification of Canister and Cladding Integrity – FY2014 Status Update

6   September 12, 2014
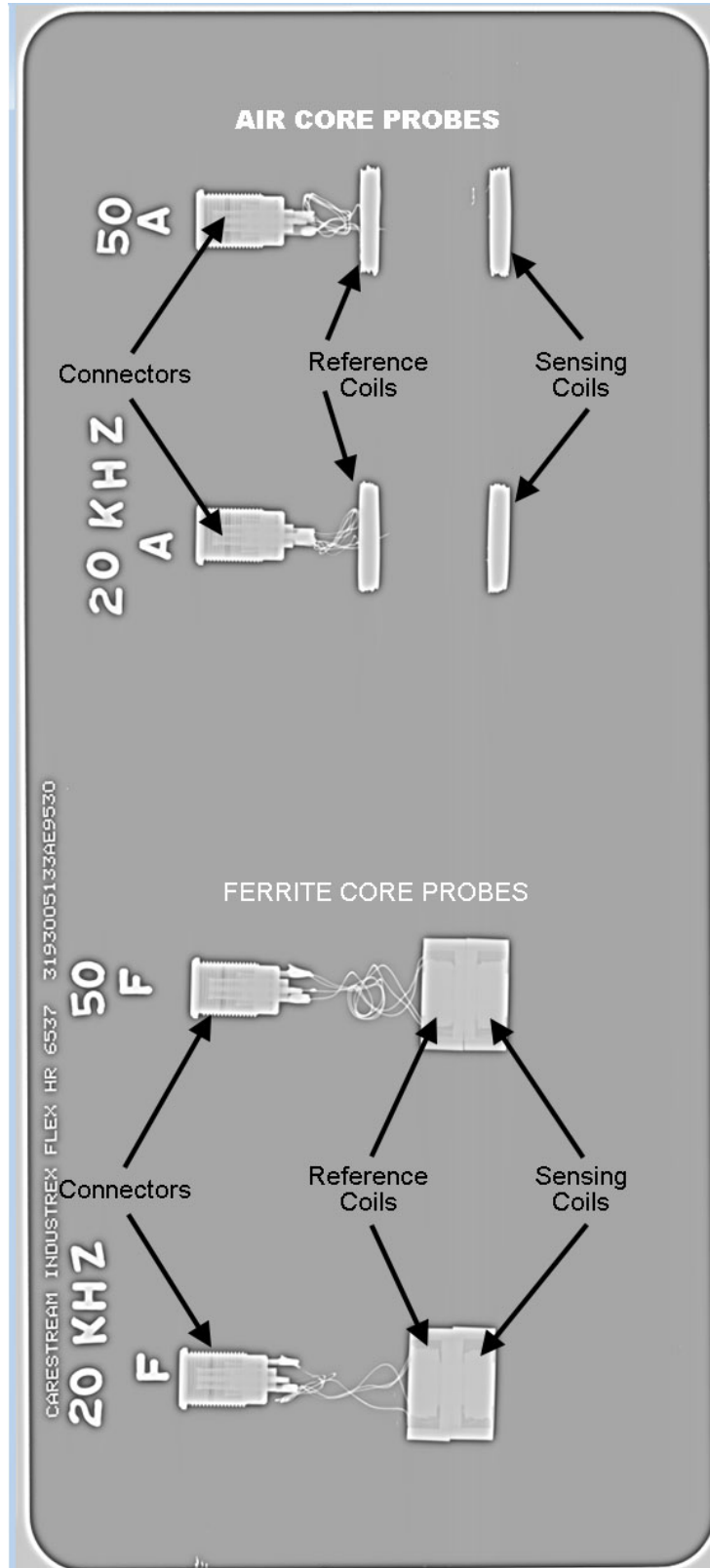
Figure 3-3. Radiographic Images of Standard Absolute Ferrite Core and Air Core Probes

Table 3-2.   Specifications for "Small" Absolute Probes with Resonant Frequencies of 20 kHz and 50 kHz

|	Small Probes	
	20-kHz Ferrite Core	50-kHz Ferrite Core
Wire Gauge	34	34
# of Turns	130	80
Coil Height	0.085 in.	0.085 in.
Coil Width	0.048 in.	0.045 in.
Coil Diameter	0.300 in.	0.280 in.
Gap Diameter	0.180 in.	0.180 in.
Core Permeability	1500	1500
Coil Resistance	4.69 Ω	30 Ω
Coil Inductance	360 μH	152 μH
H = Henries, Ω = ohms		
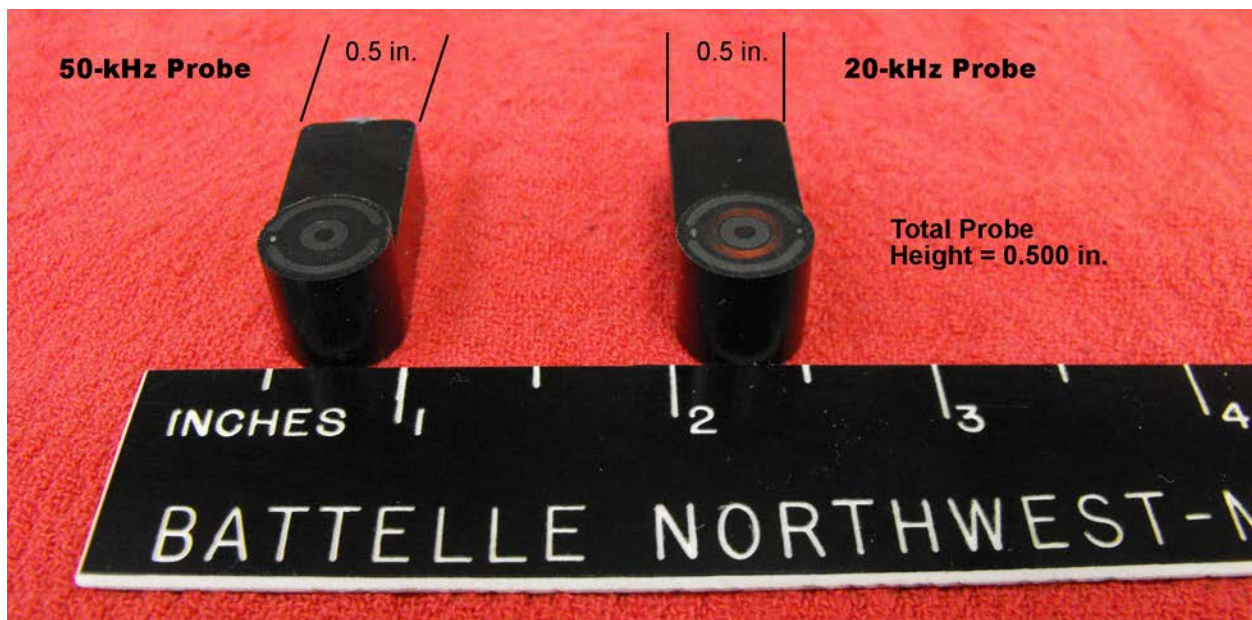
Figure 3-4.   Photograph of the "Small" Absolute Probes with Resonant Frequencies of 20 kHz and 50 kHz

3.2   Specimen Descriptions

Data was collect from several defects in four different specimens. This subsection provides a description of the specimens and the defects from which data was obtained.

3.2.1   Specimen 1 – EDM Notch and Sawcut Notch Specimen

Data was collected from a sawcut notch, referred to as Notch #11, in specimen 1. The specimen is a 304 stainless steel plate with ½-in. thickness and a photograph of the specimen is included in Figure 3-5. The geometry and dimensions of Notch #11 are depicted in Figure 3-6. As the figure depicts, the sawcut defect has a rounded profile, as opposed to a rectangular profile that is characteristic of EDM notches.
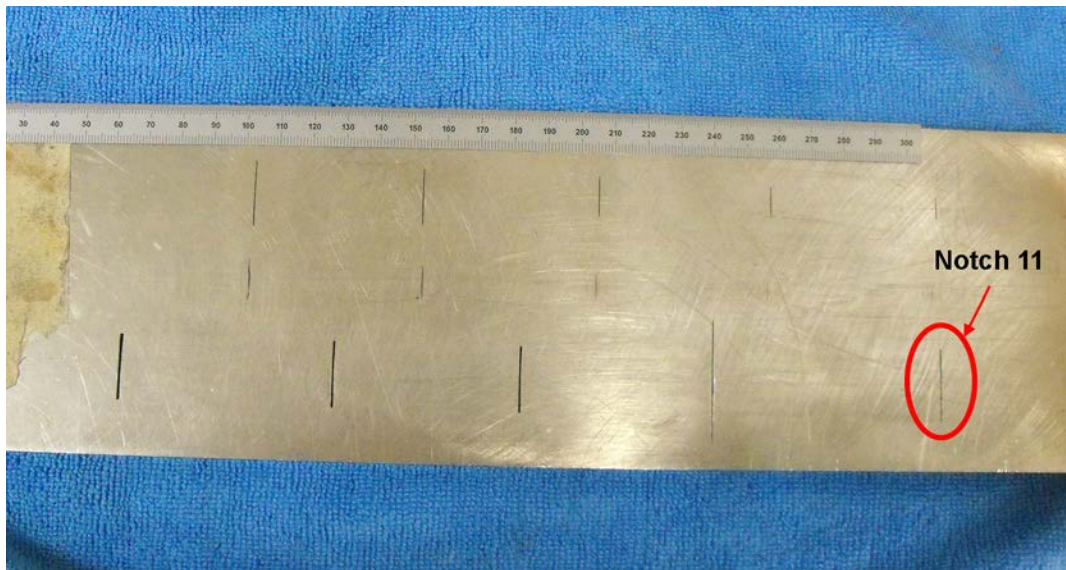

Figure 3-5.   Stainless Steel EDM Notch and Sawcut Notch Plate Specimen. Notch 11 was scanned with the eddy current probes for FEM model validation. Plate thickness is approximately ½ in.
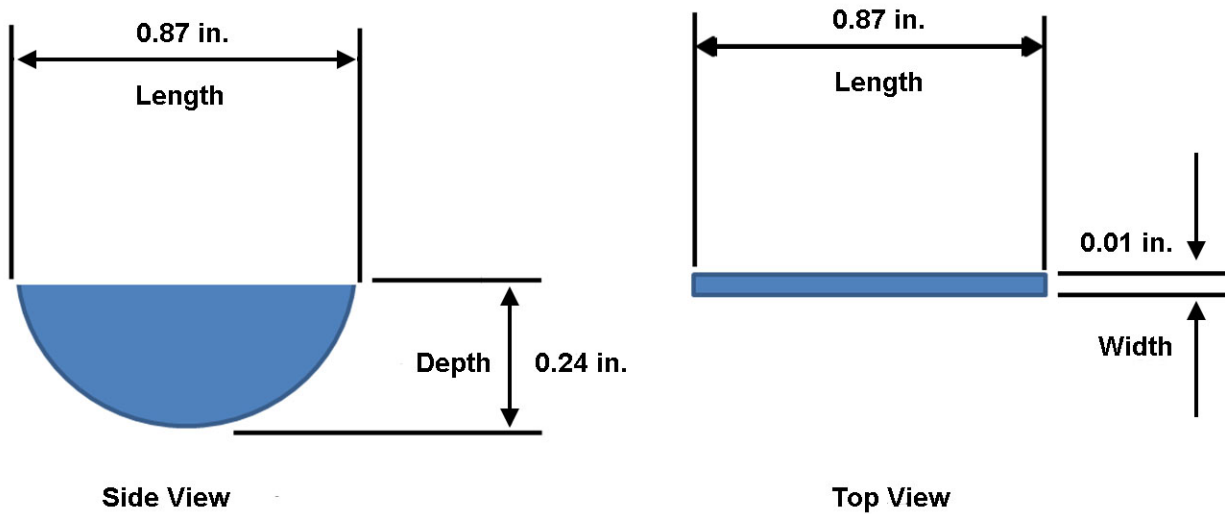
Figure 3-6.   Dimensions of Notch 11 Sawcut Notch from the EDM and Sawcut Notch Plate Specimen

3.2.2   Specimen 2 – EDM Notch Plate

Specimen 2 is also a ½-in.-thick 304 stainless steel plate specimen with several EDM notch specimens. In this case, the specimen contains six EDM notches, evenly spaced along the length of the specimen. Dimensions of the specimen and notches are indicated in Figure 3-7.
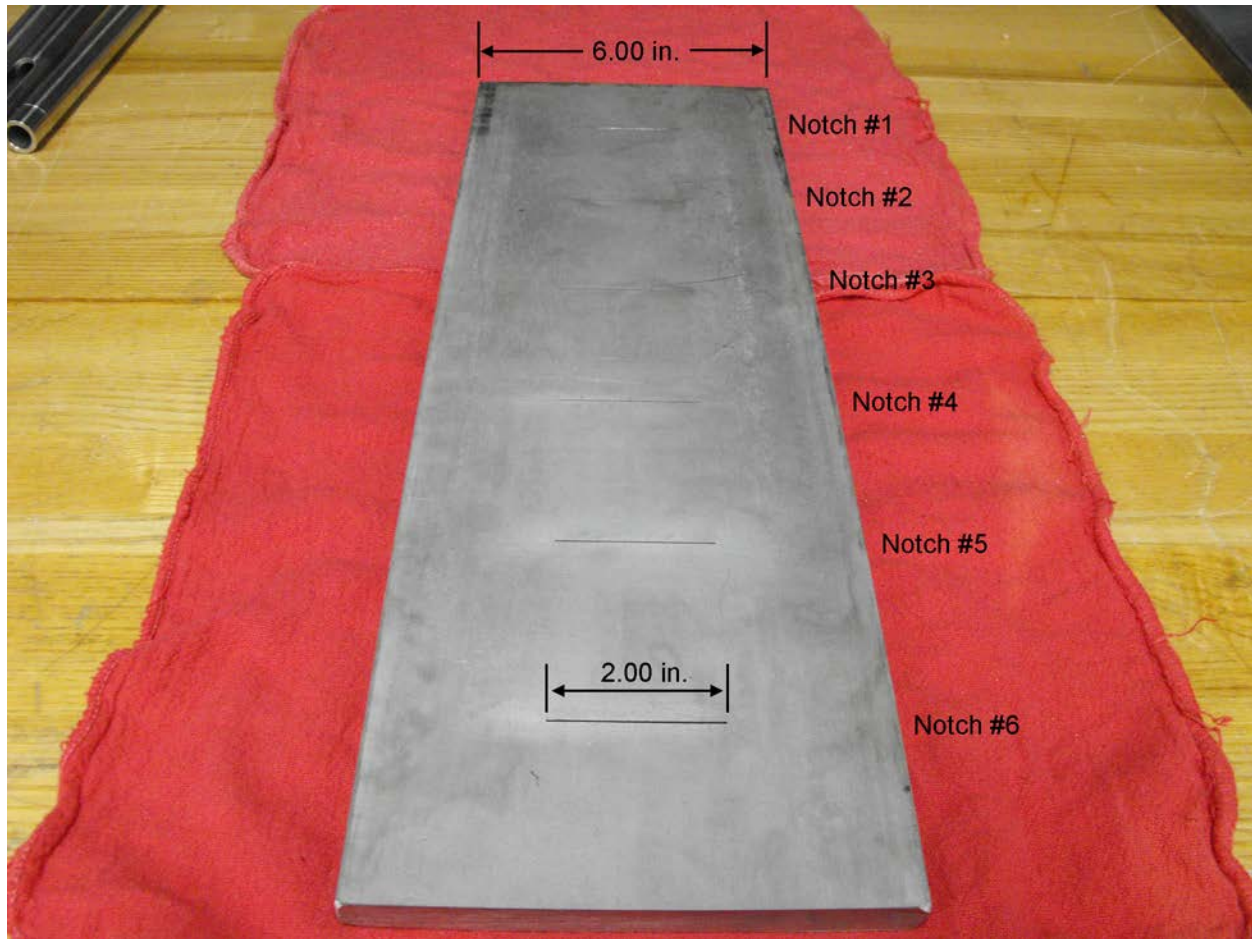
Figure 3-7.   EDM Notch Plate Specimen with Notches of Varying Depth from 2 mm to 10 mm.
Plate thickness is approximately ½ in.

3.2.3   Specimens B118 and B117 (Thermal Fatigue Cracks)

Specimens B118 and B117 are also ½-in.-thick 304 stainless steel plate specimens with thermal
fatigue cracks grown near the center of the specimens. Photographs of the specimens and
thermal fatigue cracks are included in Figures 3-8 and 3-9 for B118 and B117, respectively. The
length of the thermal fatigue cracks, as measured on the surface, is indicated in millimeters in the
figure, along with the nominal crack opening displacements (CODs). As the figures indicate, the
nominal COD for cracks in the specimens is approximately 25 µm. The depths of the cracks are
not known.
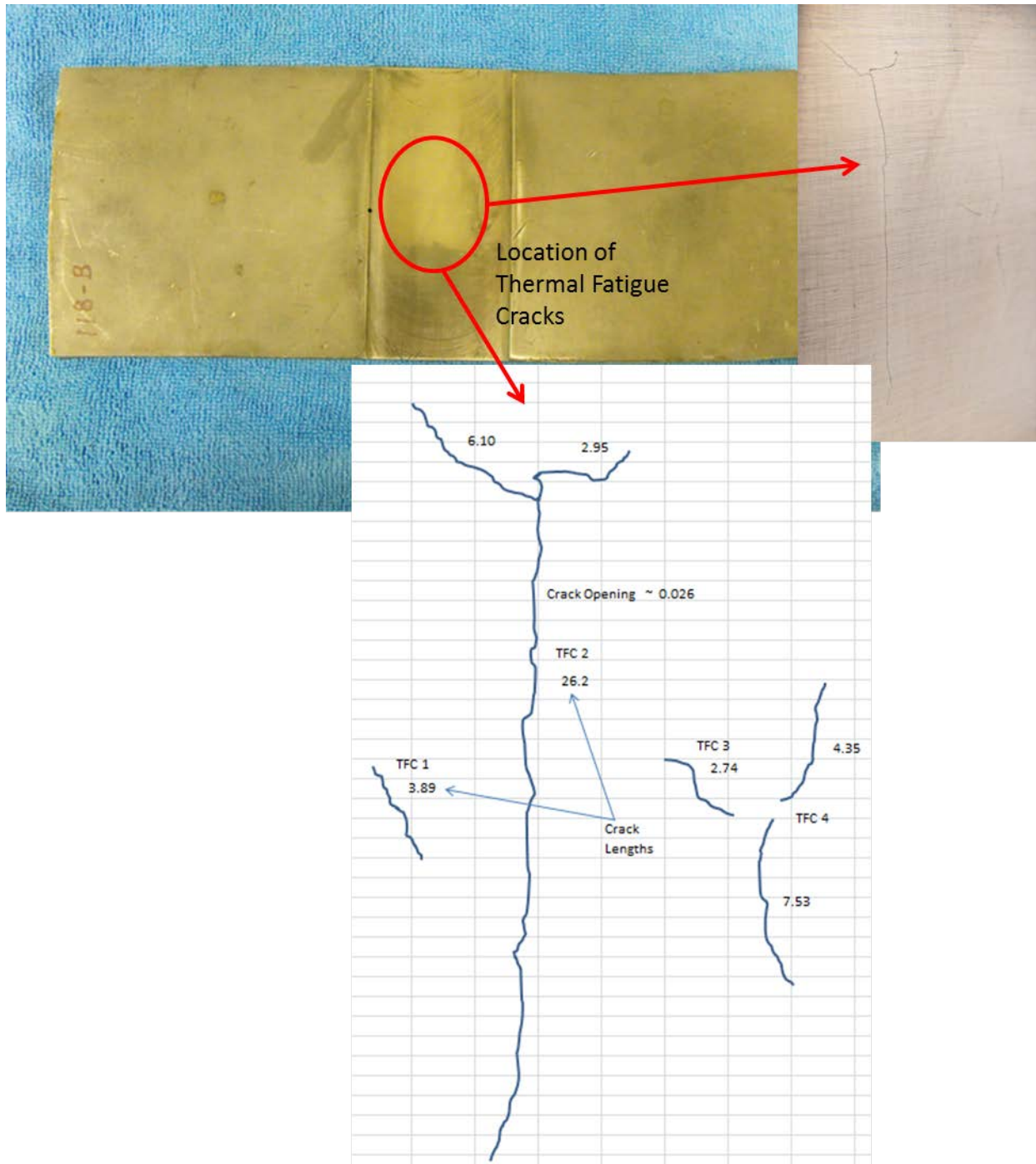
Figure 3-8.   Stainless Steel Plate Specimen B118 with Thermal Fatigue Cracks. Plate thickness is approximately ½ in.
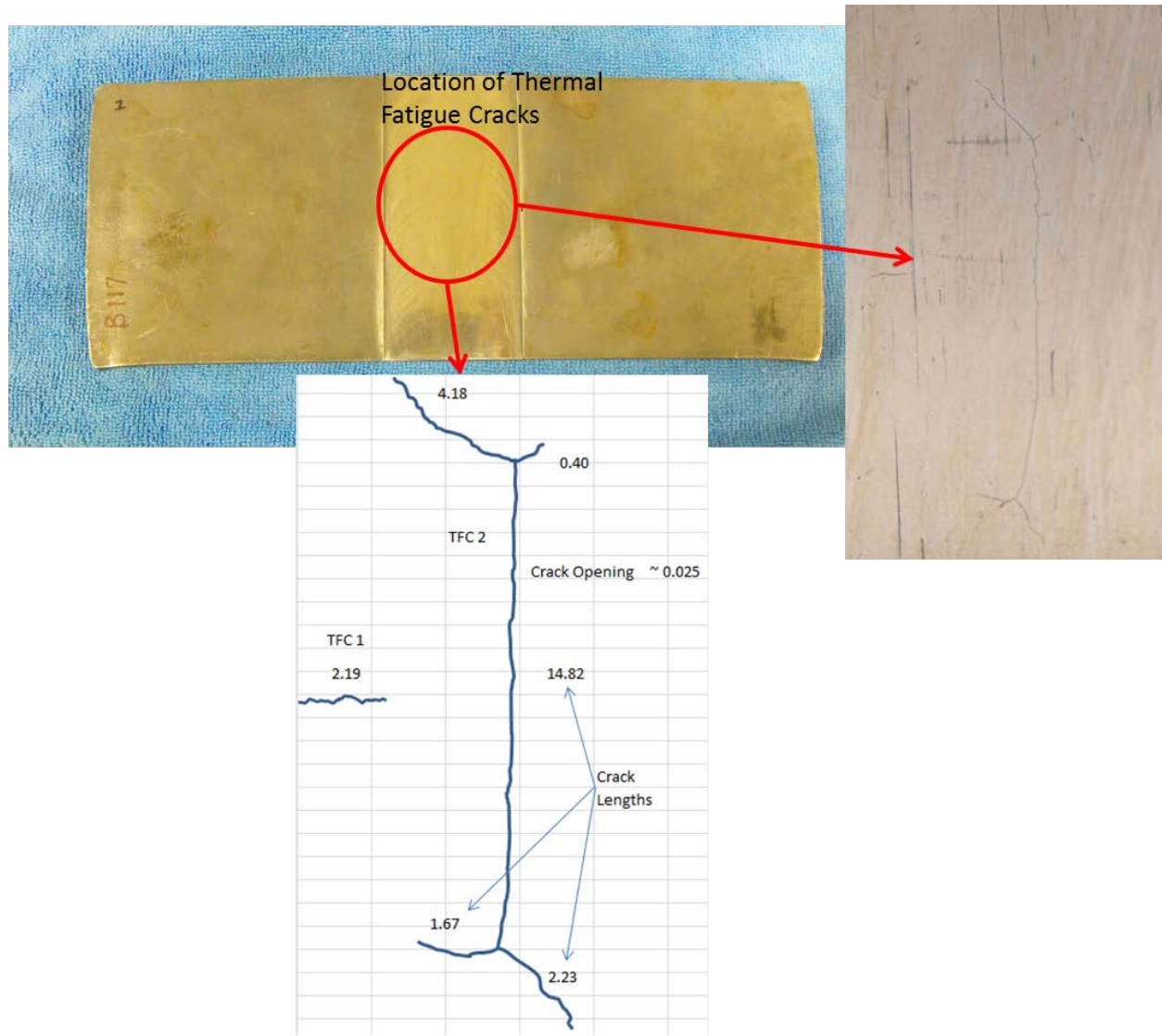
Figure 3-9.   Stainless Steel Plate Specimen B117 with Thermal Fatigue Cracks. Plate thickness
is approximately ½ in.

3.3   Data Collection and Analysis

Data collection is performed by raster scanning eddy current probes over the surface of defects in test specimens with an x-y scanner (Figure 3-10). The probes are driven, the data is read in with an Olympus NORTEC 500D flaw detector, and the data is permanently stored on a PC. This results in a collection of complex values representing impedance for each pixel in the raster scan. The scanning is performed with orientation either vertical or horizontal with respect to the notch and scan pitch of 0.01 in. by 0.01 in. The data is collected for multiple frequencies from 10 kHz to 100 kHz in 10-kHz increments. Data from raster scans performed on all specimens can be observed in Appendix B of this report.
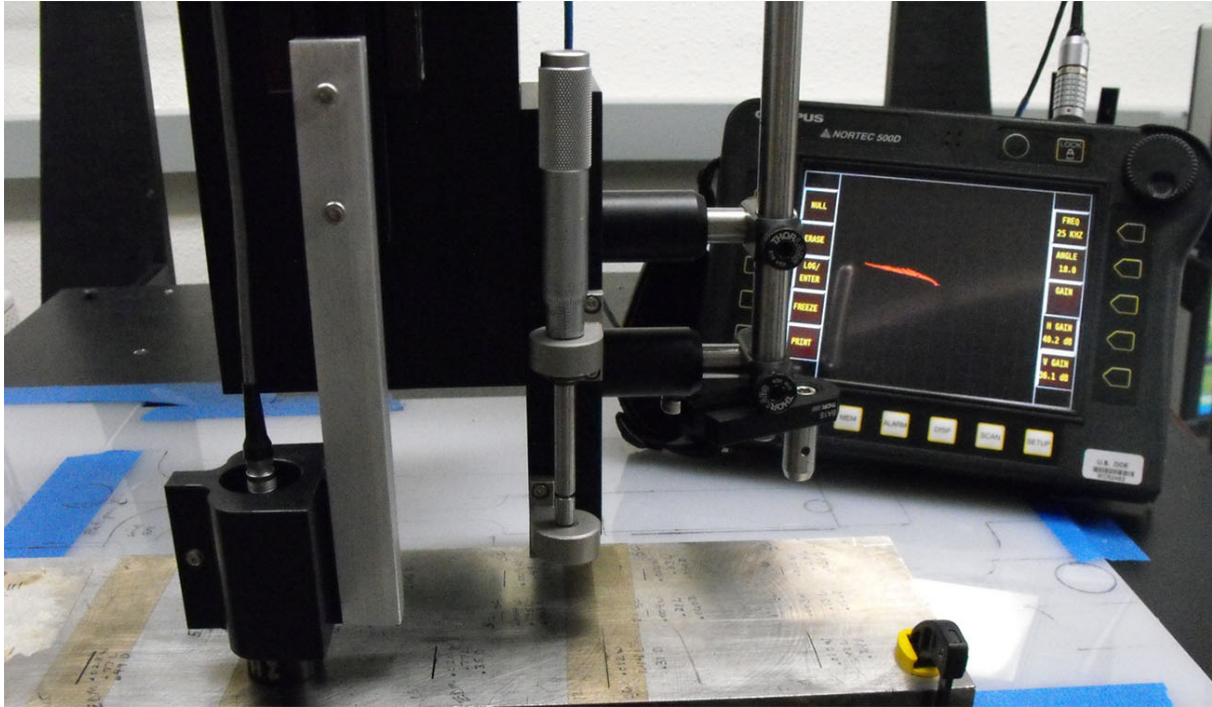
Figure 3-10. Photograph of Eddy Current Probe Raster Scanning (x-y scan) over Specimen

The change in impedance from the defect, ΔZ, is calculated by subtracting the baseline impedance, Z_0, from the impedance observed over the defect, Z_1.

$$\Delta Z = Z_1 - Z_0 = (R_1 - R_0) + j(X_1 - X_0) \qquad (3\text{-}1)$$

In this case, the impedance at the location of the peak in the magnitude of the impedance, $|Z|_{max}$, is selected to represent Z_1, and Z_0 is calculated by averaging over several pixels located at the periphery of the scan region. Thus, $|\Delta Z|$ can be calculated from

$$|\Delta Z| = |Z_1 - Z_0| = \sqrt{(R_1 - R_0)^2 + (X_1 - X_0)^2} \; , \qquad (3\text{-}2)$$

and the phase angle for ΔZ can be computed by

$$\angle \Delta Z = Tan^{-1}\left(\frac{X_1 - X_0}{R_1 - R_0}\right) = Tan^{-1}\left(\frac{\text{Im}(\Delta Z)}{\text{Re}(\Delta Z)}\right). \qquad (3\text{-}3)$$

Prior to each raster scan at each frequency, the eddy current probe is "nulled" over a defect-free portion of the specimen by adjustment of gain and phase angle. Thus, for processing data obtained at multiple frequencies, data must be normalized by correcting for these adjustments. In these efforts, the data is normalized with respect to the lowest frequency measurements (10 kHz).
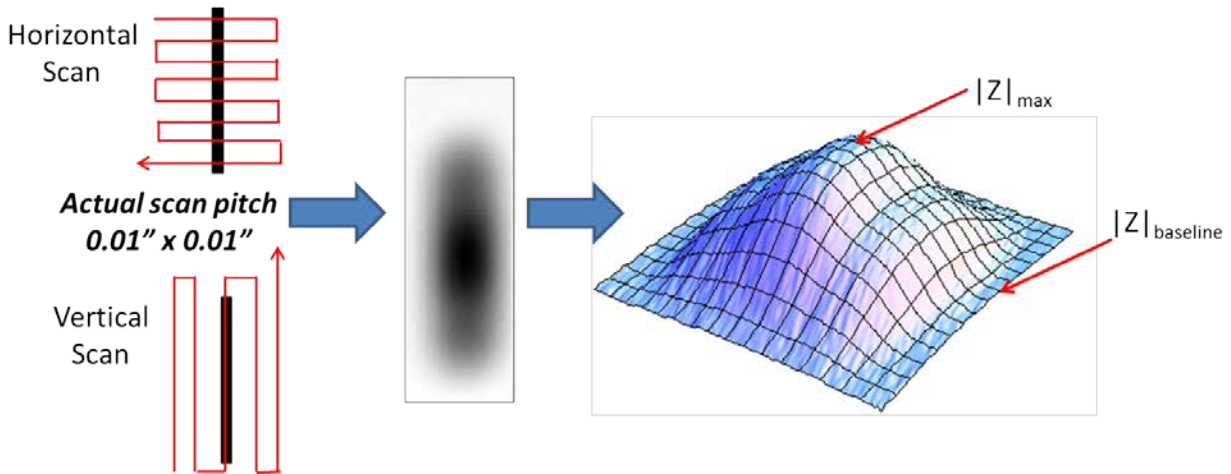
Figure 3-11.   Depiction of Horizontal Versus Vertical Raster Scanning, as well as Density and
3-D Plots of |Z| Obtained from Sawcut Notch #11, with $|Z|_{max}$ and $|Z|_{baseline}$ Shown

3.4   Results

Multi-frequency impedance data are plotted after data processing to observe features that may be useful for depth sizing. The data are presented in a manner consistent with data presented from FEM modeling, and documented in the FY2013 status report (Meyer et al. 2013a). However, the data are not normalized with respect to X_0 as the measured value of X_0 is small and introduces significant error when used in the denominator of a fraction. Plots of $|\Delta Z|$ for the defects described in Subsection 3.2 are provided in Figures 3-12–3-14; plots of $(R_1–R_0)$ are provided in Figures 3-15–3-17; plots of $(X_1–X_0)$ are provided in Figures 3-18–3-20; plots of $\angle\Delta Z$ are provided in Figures 3-21–3-23; and impedance plane plots are provided in Figures 3-24–3-26.
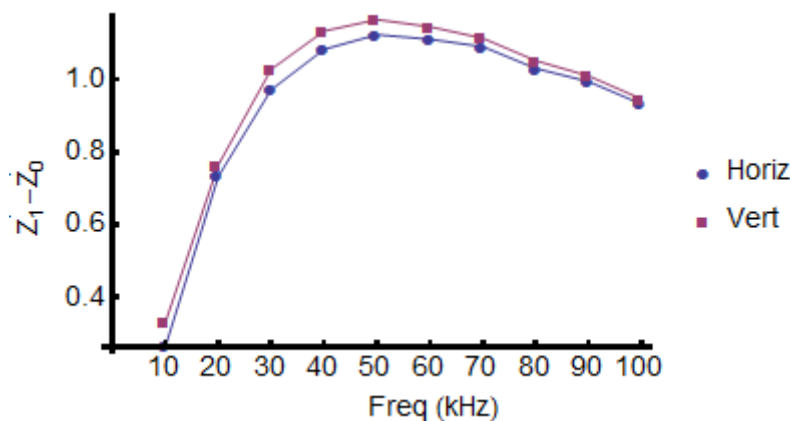

Figure 3-12.   Magnitude of Change in Impedance, $|\Delta Z|$ for Sawcut Notch #11 from Specimen 1.
Vertical and horizontal raster scan data as depicted in Figure 3-11 is included.
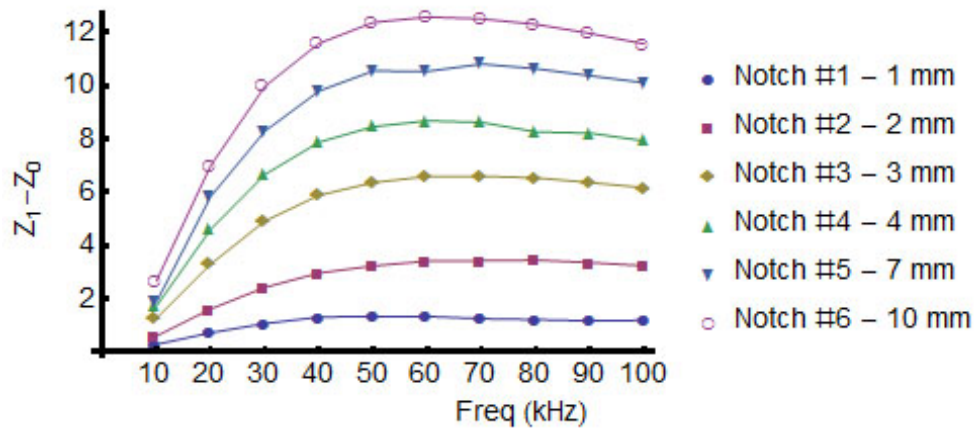
Figure 3-13. Magnitude of Change in Impedance, |ΔZ| for EDM Notches in Specimen 2
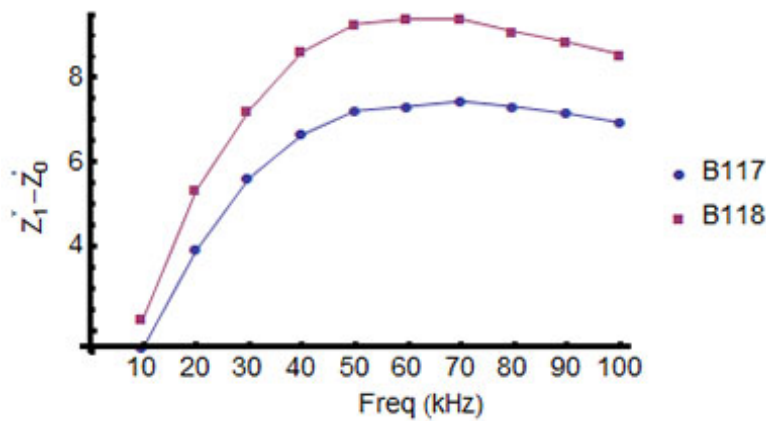
Figure 3-14.   Magnitude of Change in Impedance, |ΔZ| for Thermal Fatigue Cracks in
Specimens B117 and B118
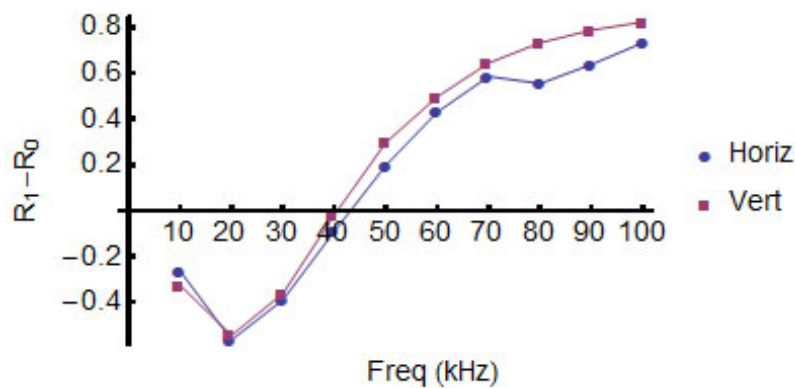
Figure 3-15.   Plot of (R_1–R_0) for Sawcut Notch #11 from Specimen 1. Vertical and horizontal
raster scan data as depicted in Figure 3-11 is included.
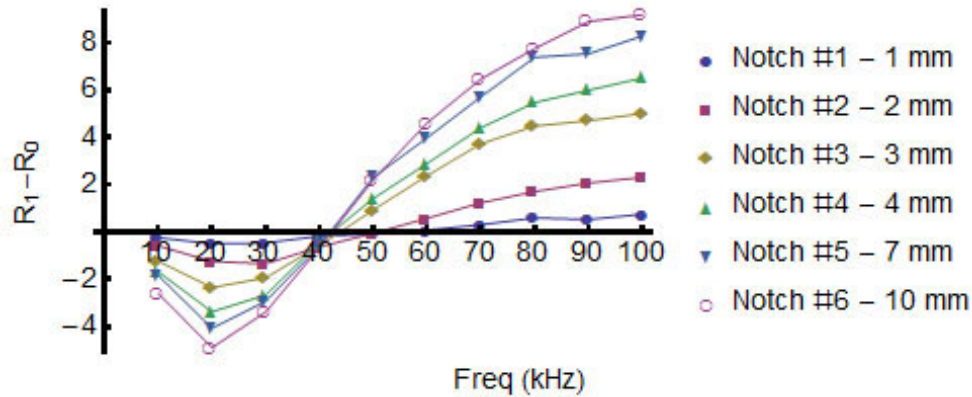
Figure 3-16. Plot of (R_1–R_0) for EDM Notches in Specimen 2
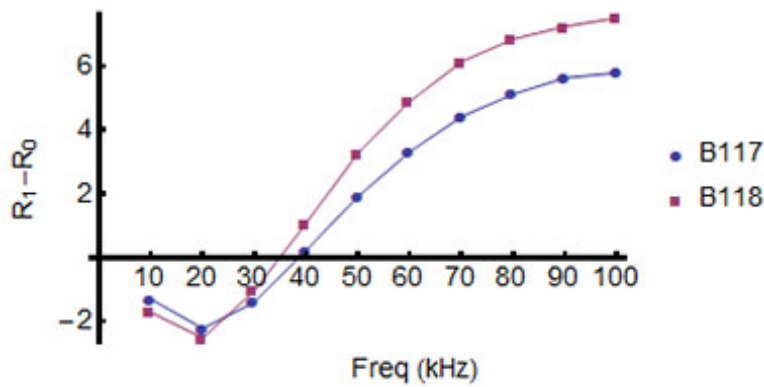
Figure 3-17. Plot of (R_1–R_0) for Thermal Fatigue Cracks in Specimens B117 and B118
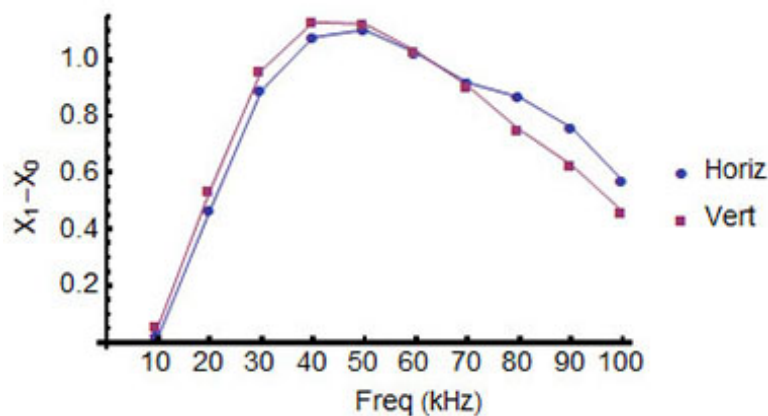
Figure 3-18. Plot of (X_1–X_0) for Sawcut Notch #11 from Specimen 1. Vertical and horizontal raster scan data as depicted in Figure 3-11 is included.
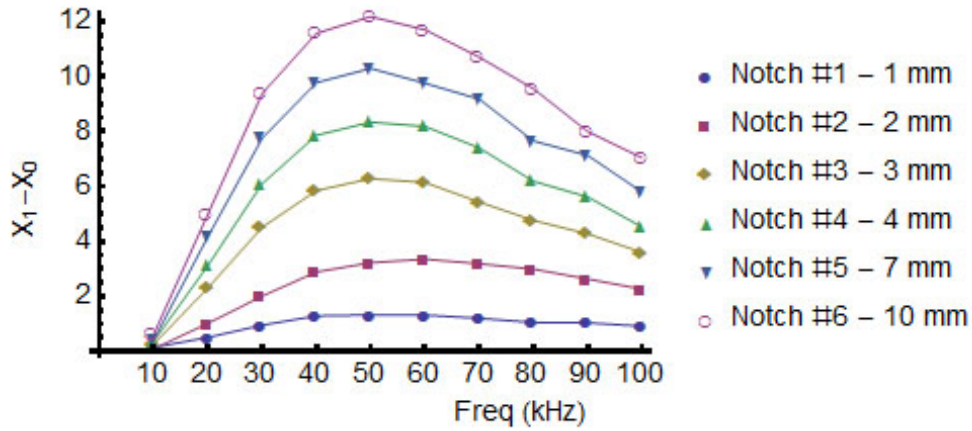
Figure 3-19. Plot of $(X_1 - X_0)$ for EDM Notches in Specimen 2
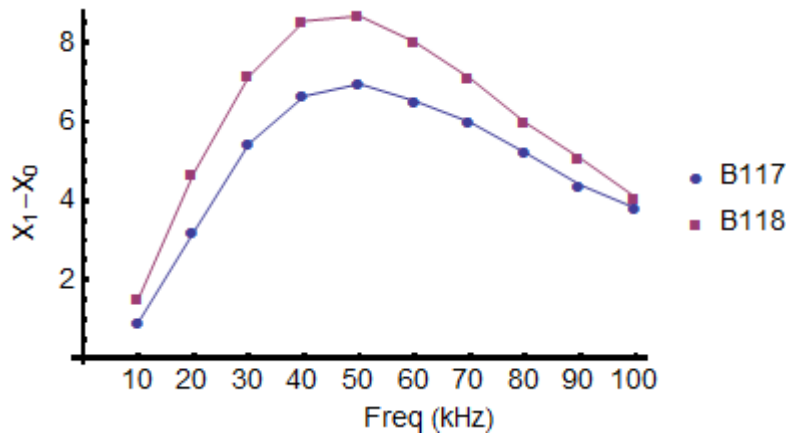
Figure 3-20. Plot of $(X_1 - X_0)$ for Thermal Fatigue Cracks in Specimens B117 and B118
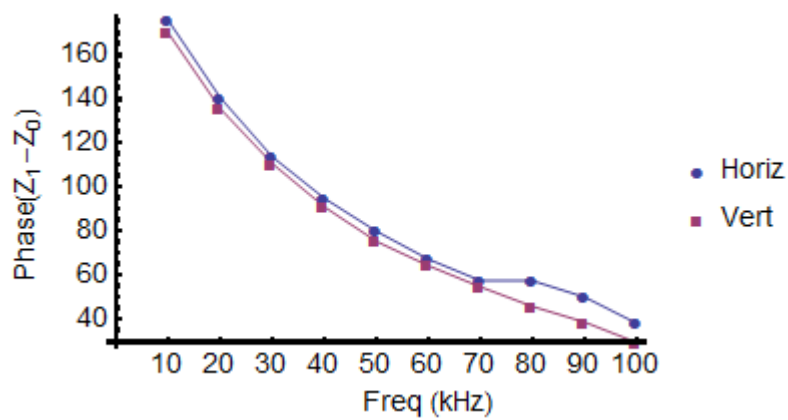
Figure 3-21.   Plot of $\angle \Delta Z$ for Sawcut Notch #11 from Specimen 1. Vertical and horizontal
raster scan data as depicted in Figure 3-11 is included.
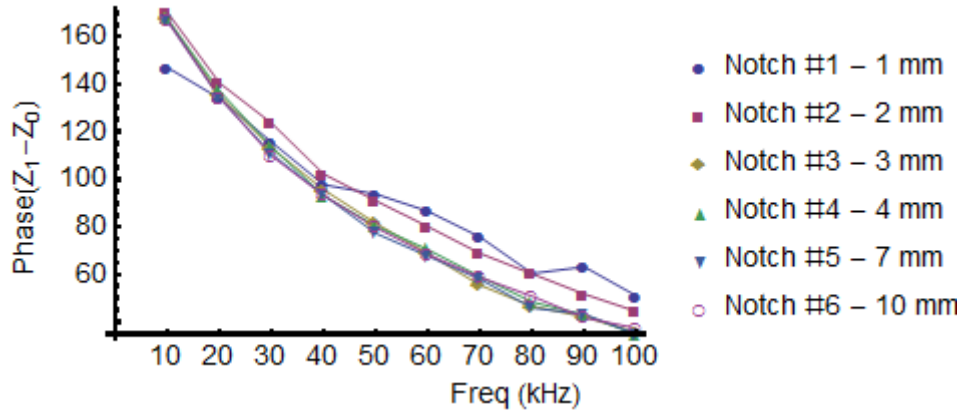
Figure 3-22. Plot of ∠ΔZ for EDM Notches in Specimen 2
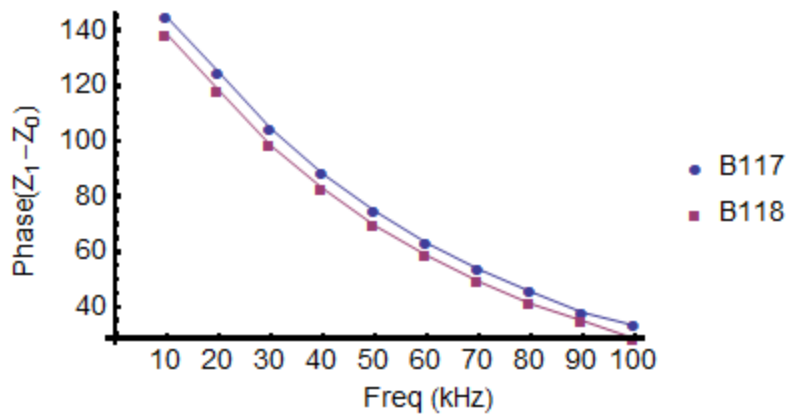
Figure 3-23. Plot of ∠ΔZ for Thermal Fatigue Cracks in Specimens B117 and B118
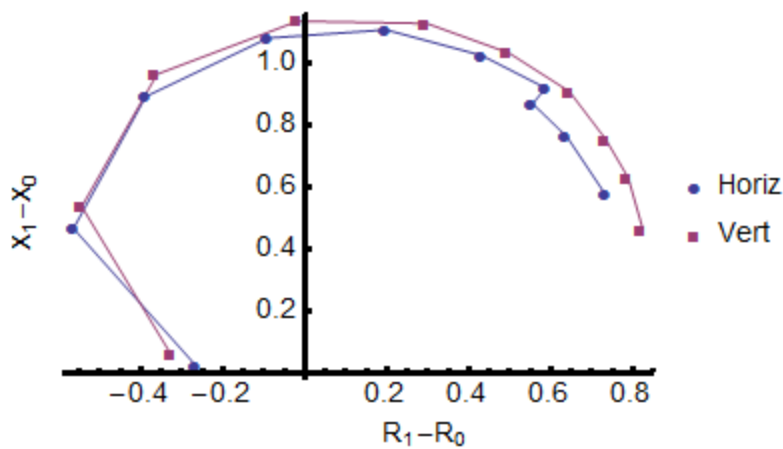
Figure 3-24.   Impedance Plane Plots for Sawcut Notch #11 from Specimen 1. Vertical and
horizontal raster scan data as depicted in Figure 3-11 is included.
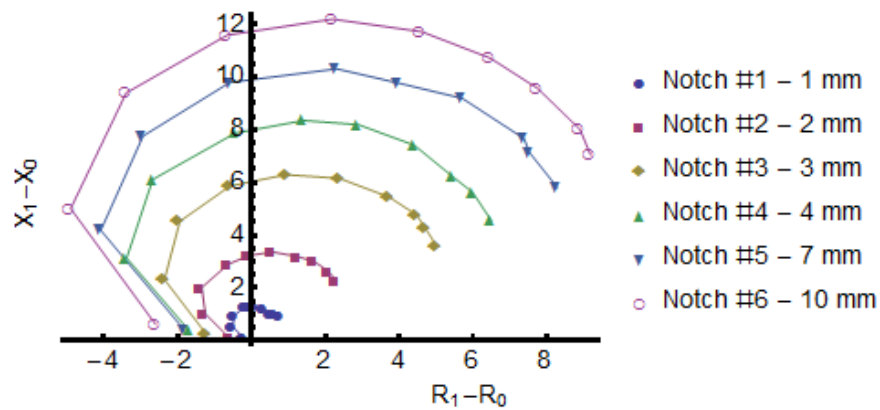
Figure 3-25. Impedance Plane Plots for EDM Notches in Specimen 2
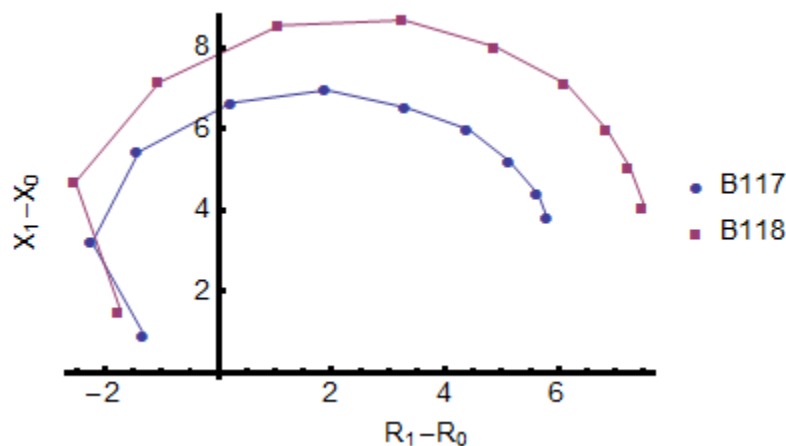
Figure 3-26. Impedance Plane Plots for Thermal Fatigue Cracks in Specimens B117 and B118

3.5   Comparison of EDM Notch Data with Thermal Fatigue Crack Data

Significant similarity is observed between signals from thermal fatigue cracks in specimens B117 and B118 and EDM notches in specimen 2. Thus, data for specimens B117 and B118 is plotted with data for EDM notches for direct comparison in Figures 3-27–3-29. In Figure 3-27, data from specimens B117 and B118 envelops the data obtained from EDM Notch #4, which is 4-mm deep. This plot indicates that the depth of thermal fatigue cracks in specimen B117 is between 3-mm and 4-mm, while cracks in specimen B118 are between 4-mm and 7 mm-deep. In Figure 3-28, the curves for specimens B117 and B118 intercept the frequency axis below 40 kHz, while the curves for EDM notches intercept the frequency axis above 40 kHz. Further, the extremum observed in (R1–R0) near 20 kHz is less pronounced for B117 and B118 data than for EDM notches. Finally, for Figure 3-29, the value of $\angle \Delta Z$ at 10 kHz for data from B117 and B118 is near 140 degrees; whereas, for EDM notches, the value of $\angle \Delta Z$ at 10 kHz is closer to 165 degrees.
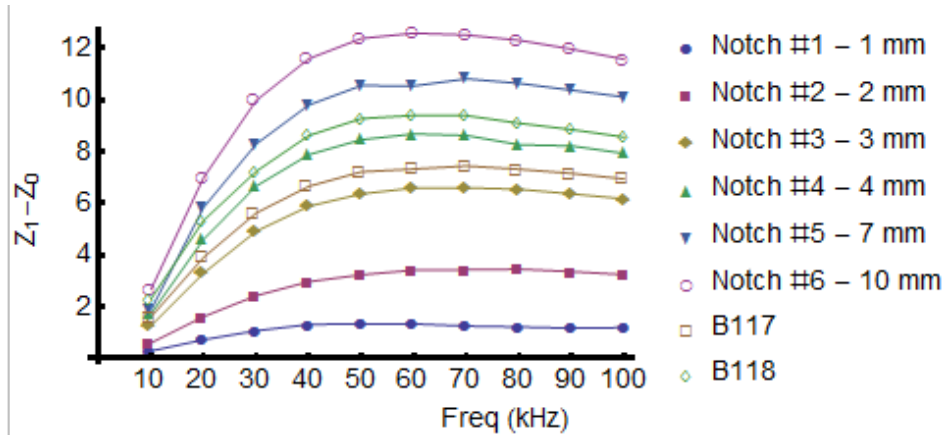
Figure 3-27. Magnitude of Change in Impedance, |ΔZ| for EDM Notches in Specimen 2 and for Thermal Fatigue Cracks in Specimens B117 and B118
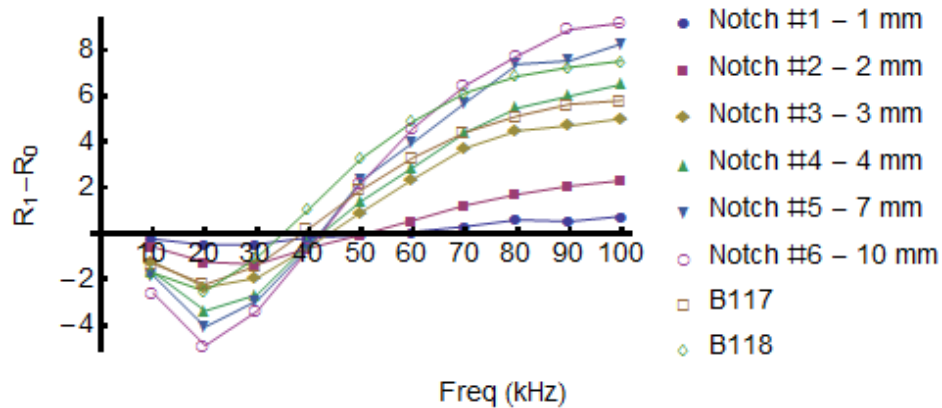
Figure 3-28. Plot of $(R_1 - R_0)$ for EDM Notches in Specimen 2 and for Thermal Fatigue Cracks in Specimens B117 and B118
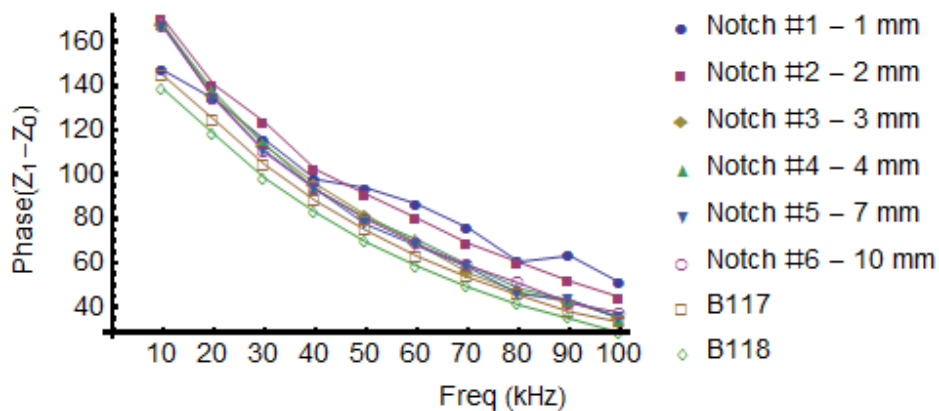
Figure 3-29. Plot of ∠ΔZ for EDM Notches in Specimen 2 and for Thermal Fatigue Cracks in Specimens B117 and B118

3.6   Comparison with FEM

The purpose of these experimental efforts is to validate the FEM performed in FY2013 and
benchmarking of results. Further modeling was required to accurately represent the probes in
Subsection 3.1. In this case, the 20-kHz standard probe with ferrite core was modeled with
ANSYS, as well as the EDM Notch #4 in specimen 2. An illustration of this model is provided
in Figure 3-30. The measurement data are obtained with an Agilent 4294A impedance analyzer
with data collected with the probe centered over the notch and at a point on the defect free
surface of the plate specimen. The measurement data is compared with FEM results by plotting
data in the normalized impedance plane in Figure 3-31.

Figure 3-31 indicates reasonable agreement between measurement and FEM simulation results,
indicating that the eddy current probe can be adequately modeled. From this data, it can be
concluded that FEM is a valid tool for analysis of the multi-frequency eddy current technique for
depth sizing.
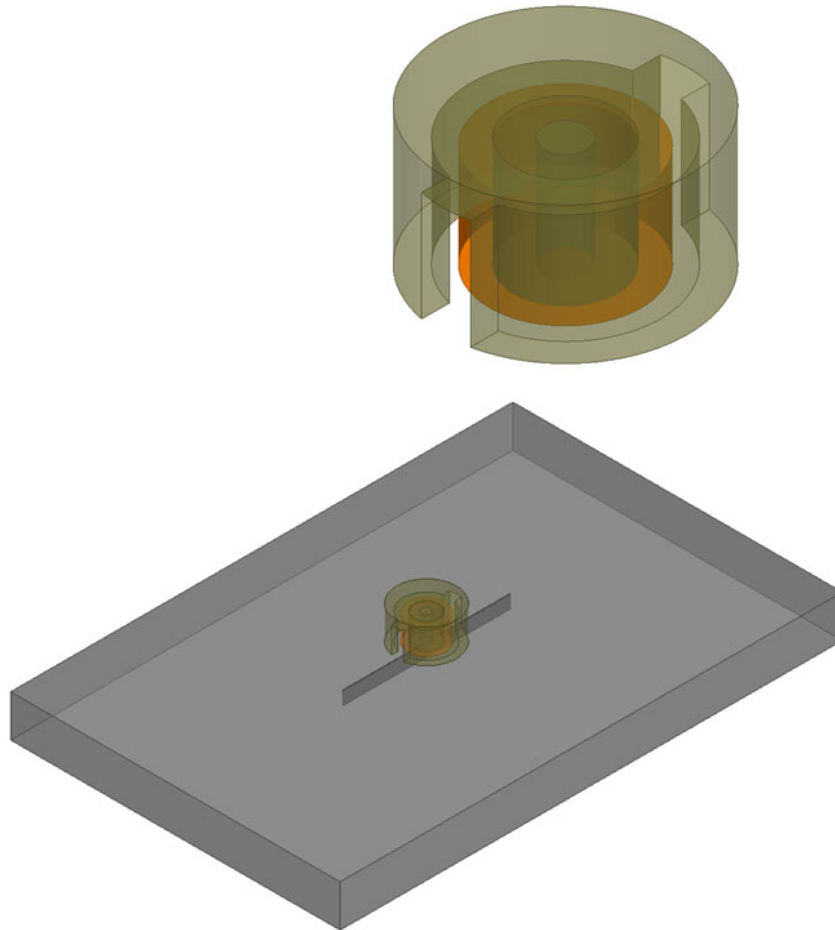
Figure 3-30.   Illustration of FEM Model of 20-kHz Standard Probe with Ferrite Core over
Notch #4 (4-mm depth EDM notch) in Specimen 2
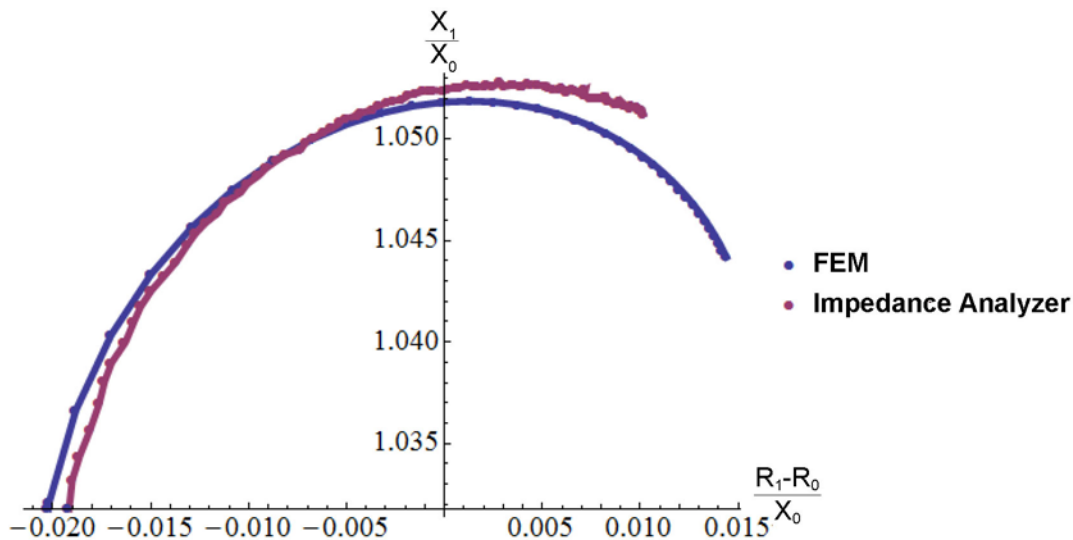
Figure 3-31.   Comparison of FEM Simulation and Measurement Results from Notch #4 in
Specimen 2

3.7   Comparison of Measurements to FY2013 Modeling Effort Conclusions

FEM studies were performed in FY2013 with the goal of identifying eddy current signal features that could be useful for characterizing SCC flaws and to delineate the effects of notch depth, equivalent conductivity, and equivalent width based on models of SCC flaws proposed by Yusa and Miya (2009). Even though FY2013 work focused on "short" notches (with aspect ratio of 3), it is appropriate to revisit these conclusions and asses FY2014 measurement results in the context of these conclusions. For convenience, those conclusions are repeated here (Meyer et al. 2013a):

1. The location of the peak in normalized impedance curves with respect to frequency may be useful for characterizing the equivalent conductivity of a flaw. The frequency at which the peak exists appears to decrease with increasing conductivity.

2. The location of zero crossings for change in normalized resistance (i.e., $\angle \Delta Z = 90°$) versus frequency may be useful for characterizing the equivalent conductivity. The zero crossings are located at lower frequencies for 5% conductivity notches versus 0% conductivity notches.

3. The existence and location of minimum values in the change in normalized resistance curves versus frequency may be useful for characterizing the equivalent conductivity of a flaw. For deeper flaws (i.e., 8.4 mm), this minima exists for 0% conductivity flaws but not 5% conductivity flaws.

4. The phase angle of the change in normalized impedance indicates a monotonic behavior with respect to notch depth over the frequency range considered for 0% conductivity notches. However, for 5% conductivity notches, this trend is not as apparent.

5. A metric defined as the ratio of the phase angle of the change in normalized impedance at 5 kHz to the phase angle of the change in normalized impedance at 100 kHz appears to provide a good discriminator of flaw conductivity regardless of notch depth.

With respect to *Conclusion 1,* no perceptible shift is observed in the peak of $|\Delta Z|$ between the thermal fatigue cracks and EDM notches. This would indicate that the equivalent conductivity of the thermal fatigue cracks is 0%.

With respect to *Conclusion 2,* the zero crossings for $(R_1 - R_0)$ versus frequency are at slightly lower frequencies for thermal fatigue cracks compared to EDM notches. This indicates that the conductivity of thermal fatigue cracks is non-zero. However, the size of the shift suggests the conductivity is much less than 5%.

With respect to *Conclusion 3,* the minima observed in plots of $(R_1 - R_0)$ are less significant for thermal fatigue cracks compared to EDM notches. However, the minima are clearly still present. This indicates that the conductivity of thermal fatigue cracks is small but non-zero.

With respect to *Conclusion 4,* no monotonic trend is observed for $\angle \Delta Z$ versus notch depth for EDM notches.

With respect to *Conclusion 5,* a similar metric can be created for measurement results by taking the ratio of $\angle \Delta Z$ at 10 kHz to 100 kHz. The result shows that there is no perceptible difference between this metric for EDM notches and the thermal fatigue cracks, which would indicate the thermal fatigue cracks have zero, or close to zero, conductivity.

4.   OVERVIEW OF ADVANCED EDDY CURRENT INSTRUMENTATION/ CONCEPTS

Section 3 described FY2014 efforts towards development of a multi-frequency eddy current technique for sizing stress corrosion cracks using an absolute probe. However, more sophisticated eddy current probe instrumentation and concepts could also be developed to facilitate improved flaw characterization. As described below, these improvements may be realized through use of more sophisticated sensors, probe configurations, and/or field excitation signals.

4.1   Send/Receive Eddy Current Probes

Send/receive eddy current surface probes go by several names, including reflection probes, driver-pickup probes, and exciter-pickup probes. Instead of monitoring the impedance on a single coil of wire, a coil is used to induce the eddy current, which is then measured by a separate probe. The measuring probe may be a wire coil (Auld et al. 1989), a hall probe (Tian et al. 2005), a superconducting quantum interference device (SQUID) (Muck et al. 1997; Braginski and Krause 2000; Chieh et al. 2010), or a magnetoresistive sensor (Dogaru and Smith 2001; Yang et al. 2010). Essentially, any technique which is capable of measuring the induced eddy current may be considered. Send/receive configurations, in general, can yield higher gain (meaning stronger signal) and support a larger frequency range than other configurations. Additionally, the pickup and driver elements can be individually customized for specific applications. For instance, driver coils may be relatively large and rectangular in order to produce a straight-edged eddy current that tiles more conveniently into arrays, while the pickup coil can still be very small to maintain high spatial resolution (Fava et al. 2009; He et al. 2010).

4.2   Types of Sensors

4.2.1   Wire Coil

Wire coil pickups are the most common traditional probe type for eddy-current testing (ECT). The eddy current created by a drive coil induces a measurable voltage in the pickup coil. This voltage is either measured directly with a single pickup coil or differentially with a pair of bridged coils, such as the configuration shown in Figure 4-1. When oriented parallel to the surface of the test material, they are commonly referred to as "pancake coils." They may be circular, rectangular, spiral, or even horseshoe-shaped (Garcia-Martin et al. 2011). They are very sensitive to edge effects, which can be confused with material flaws, and they do not detect delamination-type flaws because the eddy currents flow parallel to the surface. Wire coils are also very sensitive to liftoff distances, which can be hard to control under realistic measurement conditions.

However, coil-type pickups are very simple in construction and are compatible with a very large dynamic range of alternating current (AC) frequencies, which are major reasons for their frequent adoption.
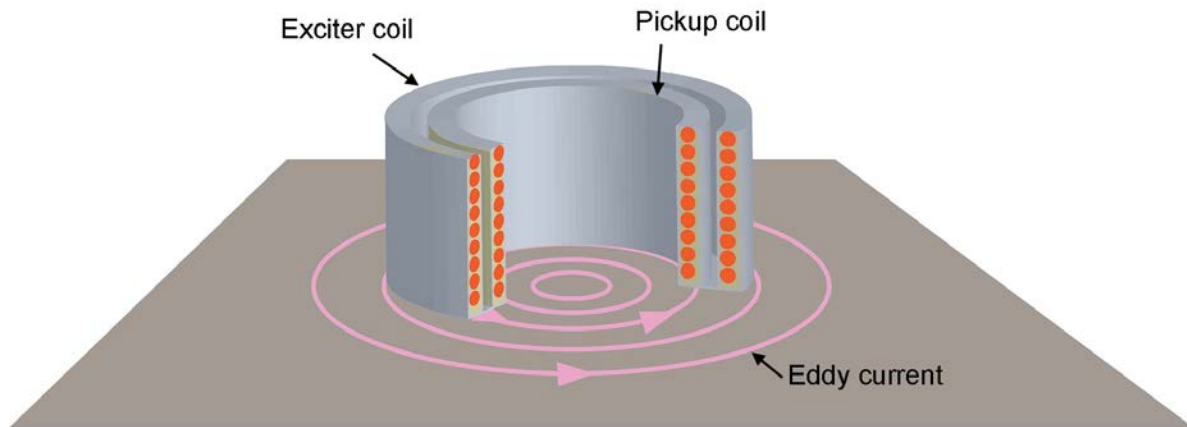
Figure 4-1.   Wire-coil-based Reflection Probe Setup Showing Cross Section of the Two Coils.
                Two circuits are used to drive the two coils, each of which is a pancake-type coil.

4.2.2   Hall Probes

Hall probes provide magnetic field measurements that are very sensitive to direction. A
magnetic field running perpendicular to a current moving through a semiconductor will generate
a voltage potential orthogonal to both magnetic field and current (Serway and Beichner 2000).
The magnitude of this voltage is directly proportional to the strength of the magnetic field. This
is called the Hall Effect and is illustrated in Figure 4-2.
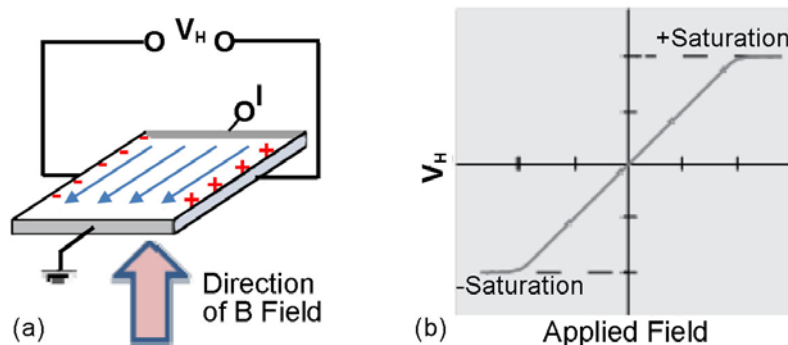
Figure 4-2.   Simple Illustration of a Hall Probe Showing How Voltage Output (VH) Responds
                Orthogonally to Both External B Field and Applied Current (a), and Example of
                Typical VH Behavior Versus B Field (b)

Hall Effect sensors are good for miniaturized probe configurations, and have become extremely
mature solutions for microelectronic circuitry. In ECT applications, Hall probes are usually used
to measure the vertical (or surface normal) component of the magnetic field. They can be very
sensitive to weak magnetic fields, but require work-around solutions to deal with signal-to-noise
issues.

In general, Hall probes are referred to as being "extremely temperature stable," but this is because they work very well from cryogenic temperatures up to around 150°C. Maximum operation ratings below 150°C are often cited, and this is usually because of packaging issues. However, above 150°C, the semiconductor material properties are severely limiting, and magnetic field sensitivities tend to plummet. Some recent papers of academic origin have addressed the problems of operating Hall sensors at high temperatures and in radiological environments by using unique structures based on material sets not found in the commercial environment (Jankowski et al. 2011; Abderrahmane et al. 2012). One study was able to achieve stable performance up to 400°C using a multilayer of AlGaN/GaN (Abderrahmane et al. 2012); however, this material set is not available commercially to our knowledge.

In the commercial landscape, several domestic and foreign vendors sell Hall sensors of various sorts, including ASensor, Lakeshore, Micropac Industries, Honeywell, and others. It is important to note that most off-the-shelf Hall sensors are currently of the digital switching variety, which does not output a scaled voltage. ECT applications demand analogue Hall sensors, which narrows the field significantly.

For-high temperature applications Micropac Industries offers a product that is rated up to 200°C, which is the highest off-the-shelf performance we have seen. None of these vendors provide systems rated for radiation exposure except for Lake Shore Cryotronics, Inc. Lake Shore's website states that Hall probes are relatively insensitive to Gamma radiation, suffer from less than 0.5% change in signal from 10 Mrad of protons, but are sensitive to high doses of neutrons over 10^{15} N/cm^2. Doses of this magnitude may cause 3–5% decrease in magnetic field sensitivity. This agrees fairly well with some older literature that identified significant increases in measurement error from neutron doses above 10^{10} N/cm^2 (Kulke et al. 1989).

4.2.3   Giant Magnetoresistive Sensors (GMR)

Magnetoresistive sensors exhibit a linear relationship between resistance and external magnetic field strength. Although sensitive to small magnetic field changes, they suffer from large thermal noise problems, which can limit their use in some applications. GMRs are sensitive to magnetic field components along a single axis and are insensitive to components orthogonal to this axis. This property can be used to reduce edge-induced noise (Dogaru and Smith 2001).

GMRs, first developed for computer hard drives, are composed of layers of magnetic materials separated by very thin insulating layers. Because of this extensive background, the technology is well understood and they can be purchased now from a large number of commercial vendors including Kodak, Honeywell, Phillips, and others. The resistance measured across these layers is directly proportional to the magnetic field component in that direction and decreases with increasing field strength because of the reorientation of domain polarities (Tamanaha et al. 2008; Germano et al. 2009). A highly simplified illustration of this effect is shown in Figure 4-3. They can be fabricated to micron-scale dimensions, making them well suited for any eddy current probe size (Boltz et al. 1998).
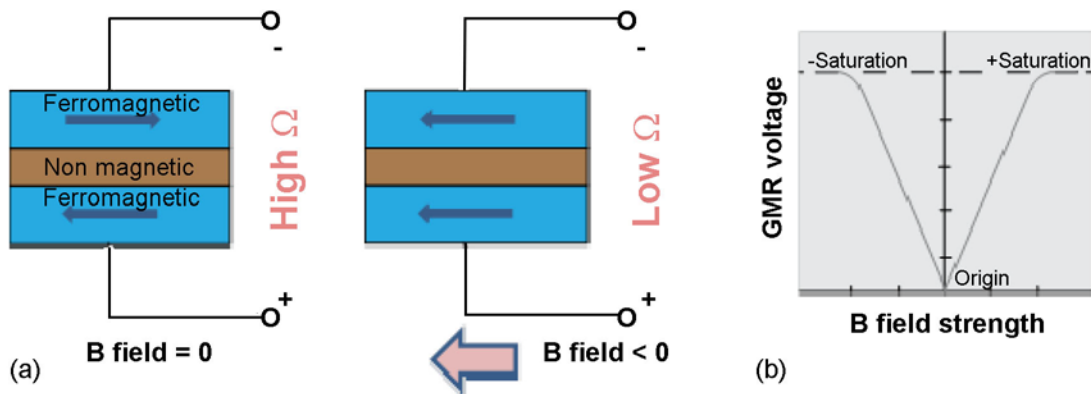
Figure 4-3.   Simplified Illustration of GMR Responding to External B Field (a) and Example of
Typical GMR Voltage Output Versus B Field Strength (b)

Companies that provide GMRs include NVE Corporation, Hitachi Metals, Honeywell, and a few
others. Most vendors sell GMRs as readers for magnetic storage media in computers. NVE
seems to be one of the primary vendors of research GMRs, as most references point back to
them. The temperature limits of GMRs are similar to those of Hall probes, and often top out
around 150°C. Some companies, such as NVE, offer sensors that are rated to 200°C. These
limits, unfortunately, are imposed by the GMR material itself, rather than the packaging. At
temperatures above 200–250°C, hysteresis becomes exaggerated to the point of complete sensor
dysfunction, and magnetic field sensitivity declines sharply. Annealing of the semiconductor
layers post-fabrication seems to extend sensor stability, but only out to 175–200°C.

As with Hall probes, radiation resistance specifications are usually not included for these
sensors, although the choice of materials will make a tremendous difference. One exception is at
Honeywell, where radiation-hardened GMR development has been driven by interest in making
radiation-hardened computers. They quote survivability limits as being 10^{14} N/cm^2 for neutrons
and 10^6 Rad total dose. Most of Honeywell's products appear not to be directly suitable for eddy
current-type deployments, but if their CMOS-integrated systems can survive relatively high
radiation doses, then that implies that there is no fundamental reason that GMRs cannot be
deployed in some harsh environments. Along similar lines, Sandia published results of a study
in 2000 focused on using GMRs on radiation-hardened circuitry and showed excellent
survivability under gamma radiation doses up to 1 Mrad (Myers et al. 2000). This seems to
indicate that typical GMRs can survive a modest dose of radiation.

4.2.4   Superconducting Quantum Interference Detectors (SQUID)

SQUIDs are extremely sensitive to very low magnetic fields compared to any of the above probe
types (Garcia-Martin et al. 2011) and function at frequencies from near DC to the low MHz
range (Braginski and Krause 2000). The technology is based on thin film deposition of
superconducting loops containing so-called Josephson junctions. The loops exhibit a resonance
that is dependent on the resistance across the junctions, and this resistance changes in response to
external magnetic fields causing a change in current output (Koelle et al. 1999).

High sensitivity is achieved by lowering the noise level through cryogenic cooling using liquid nitrogen or helium (Muck et al. 1997). The Josephson Effect requires coupling between superconductors at very low temperature. The cryogenic component makes these sensors by far the most expensive and complicated to execute. For most applications, SQUID-type sensors are not practical or necessary.

Table 4-1. Summary of Eddy Current Probe Types and Characteristics

Probe type	Strengths	Weaknesses
Wire coil	• Simple construction • Large dynamic range	• Susceptible to noise • Low sensitivity ($nT/\sqrt{Hz}$ to $\mu T/\sqrt{Hz}$) • Bad edge effects
Hall probe	• Very small footprint • Medium–high sensitivity	• Low signal-to-noise • Low temperature stability
GMR	• High sensitivity ($pT/\sqrt{Hz}$) • Immune to edge effects • High temperature stability • Large dynamic range • Small footprint	• Susceptible to thermal noise
SQUID	• Highest sensitivity ($fT/\sqrt{Hz}$) • Deep penetration • Large dynamic range	• Expensive • Complicated (requires cryostat)

4.3   Possible Probe Configurations

For a two-coil reflection probe setup, the configuration can be achieved in a number of different geometries, including side-by-side and concentric arrangements (Auld et al. 1989; Chen et al. 2009; Babbar et al. 2012). Figure 4-4(a) shows a concentric arrangement. A driver coil will frequently be used with differential pickup coils (shown in Figure 4-4b–d) such as in the "split-D" configuration that is very sensitive to surface cracks. Some research efforts have explored the use of many small pickup coils inside of a larger driver in order to improve the resolution of crack sizing (Yusa et al. 2014). For all designs that incorporate a differential two-coil pickup, the scanning direction becomes very important. Differential probes exhibit the greatest defect sensitivity when the two pickup coils move over a defect sequentially rather than simultaneously. In order to circumvent this shortcoming, a rotating off-axis differential probe can be employed in some scenarios, although the probe head becomes necessarily much larger in such a case (Linn and Floyd 2007).
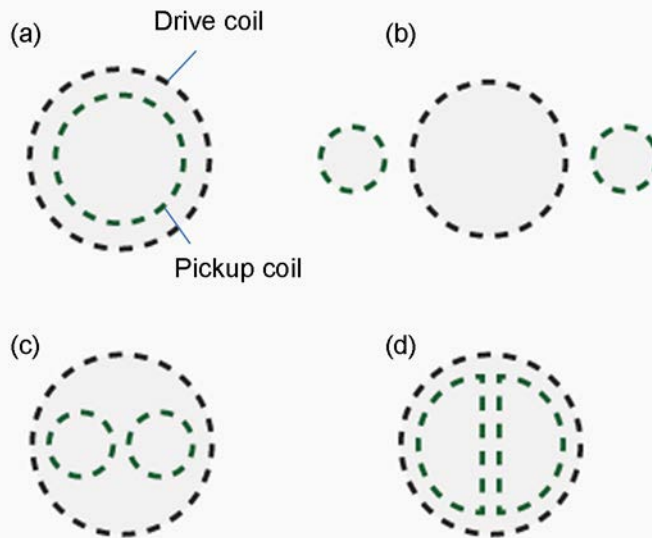
Figure 4-4.   Top View of Different Send/Receive Probe Configurations, including
(a) Concentric Absolute, (b) 180° Opposing Differential, (c) Concentric
Differential, and (d) Split-D Differential

Another manifestation of the send/receive probe is a variant of the so-called plus-point probe,
consisting of two orthogonal wire coils that stand vertically off of the test surface such that their
axes of oration are parallel to that surface. Plus-point probes are effective at detecting cracks
despite geometric and material compositional variations (Diaz et al. 2007). It has advantages of
lower drift from changing conductivity or permeability and reduced, but no eliminated, lift-off
effects (Lamtenzan et al. 2000). This sort of probe excites a much more uniform current within
the test material. Inside these two intersecting coils, it is possible to place a single pancake coil
to act as a pickup (Koyama et al. 2005). The advantage of this approach is that by running AC
current through each plus-point coil out of phase by 90°, the resultant eddy current direction
rotates, varying the directional sensitivity of the measurement.

If these intersecting coils are set side-by-side and coaxial to each other, a different sort of
functionality can be achieved. In this case, the pickup coil is situated between the two driver
coils but slightly off-center so that it is closer to one than the other (Janousek et al. 2008). In this
case, two different eddy current depth profiles exist below the pickup coil at the same time; and
as it records, the signal is deconvoluted and the ratio of the phases from each driver coil can be
correlated to the crack depth.

Another proposed way of measuring crack depth uses a more complicated differential pulsed
eddy current (PEC) method where there are two driver coils with a Hall probe inside each (Park
et al. 2013). The two drive coils, it is claimed, remove the need for a reference signal prior to
PEC measurement, and the Hall sensors measure the resultant magnetic field from the interaction
of the drive coils and eddy currents.

The use of multiple Hall sensors in eddy current probes has been proposed in the literature as a
potential solution to 3D mapping of subsurface defects (Tian et al. 2005). Hall sensors are

sensitive to directional magnetic fields, and so positioning three or more within a probe footprint can help to generate more information about what is happening to the eddy currents inside test materials. However, these approaches are data-processing intensive and convincing results have yet to be shown.

The work being done by Dr. Chady's group at Oita University has presented a number of new NDE approaches. A report from 1999 described a differential sensing method that used a single rectangular excitation coil and 14 small pickup coils to collect high-resolution information on a larger area all at once (Chady and Enokizono 1999). The following year, the same group used another multi-pickup system in multi-frequency operation in order to measure flaws from the opposing side of a notched metal plate (Chady and Enokizono 2000). The innovation of the latter paper is that, much like PEC approaches, their input signal contained a complex frequency spectrum that allowed simultaneous probing of multiple depths. Further development of the data processing using the rich quantity of data generated by this probe platform has led to some encouraging results in terms of reconstructing crack profiles (Chady et al. 2001).

4.4   Pulsed Eddy Current

The penetration depth (δ) of eddy current measurements depend strongly on the AC frequency used (f), as:

$$\delta \approx \frac{1}{\sqrt{\pi f \mu \sigma}}$$ (4-1)

where μ is the magnetic permeability of the test sample and σ is its electrical conductivity.

It is often desirable to probe deeply beneath the surface of a test material, but deeper penetration requires using a lower frequency. With this in mind, send/receive probes may be used in several operational modes, including single- or multi-frequency modes, swept-frequency mode (SFEC) (Hanysz 1958), and pulsed eddy current modes. PEC has the advantage of deeper field penetration into the test material, improved signal-to-noise ratio, lower power consumption, and richer information yield (He et al. 2010). PEC also avoids energy dissipation problems inherent to low-frequency AC (Lebrun et al. 1997). Both SFEC and PEC generate a greater quantity and breadth of data and are able to probe a range of different depths; however, PEC avoids the delays caused by the duration of the frequency sweep required for SFEC. Thus, PEC scans can be orders of magnitude faster (Moulder et al. 1996).

A great deal of recent literature has been focused on PEC for NDE (Abidin et al. 2009; Chen et al. 2009; He et al. 2010; Yang et al. 2010). A single square-wave PEC pulse contains a superimposed spectrum of low to high frequencies. Whereas traditional eddy current NDE is limited by shallow skin depths to only a couple of millimeters (Helifa et al. 2006), PEC can probe depths up to 30 mm (Lee et al. 2012). It works by replacing AC current with low duty cycle current pulses, which are repeated at frequencies between 20–100 Hz (Lebrun et al. 1997). Selection of the frequency is often not clearly justified, although one source claims that as long as the repetition period is much longer than the time constant of the square wave (often in the hundreds of microseconds) (Morozov et al. 2010). Nonetheless, at least one paper reports using

a very high repetition rate (125 kHz) with no justification or explanation (Smetana et al. 2008). The penetration depth can be tuned by changing the duty cycle of these pulses, with wider pulses containing stronger low-frequency components (Abidin et al. 2009). Thus, the larger the duty cycle, the larger the penetration depth will be. Duty cycles between 20% and 50% are commonly used (Lebrun et al. 1997; Yang et al. 2010).

In order to execute PEC measurements, a relatively modest set of equipment is required. Figure 4-5 shows what a typical configuration might look like. A function generator is needed for generating the square-wave form. The low frequencies required for PEC are not a challenge for most basic commercial models. A power amplifier is needed to increase the current to the optimal drive current, which may be as much as a few amperes (Park et al. 2013). The amplifier will be connected to the probe drive coil, and the output current of this coil, in addition to the output voltage of the pickup, will feed into a data acquisition system or oscilloscope with an analogue-to-digital converter. From there, data processing approaches are extremely diverse, depending on the user's application and preferences. For scanning purposes, many systems also make use of a 2D scanning stage in order to perform well-controlled surface scans.
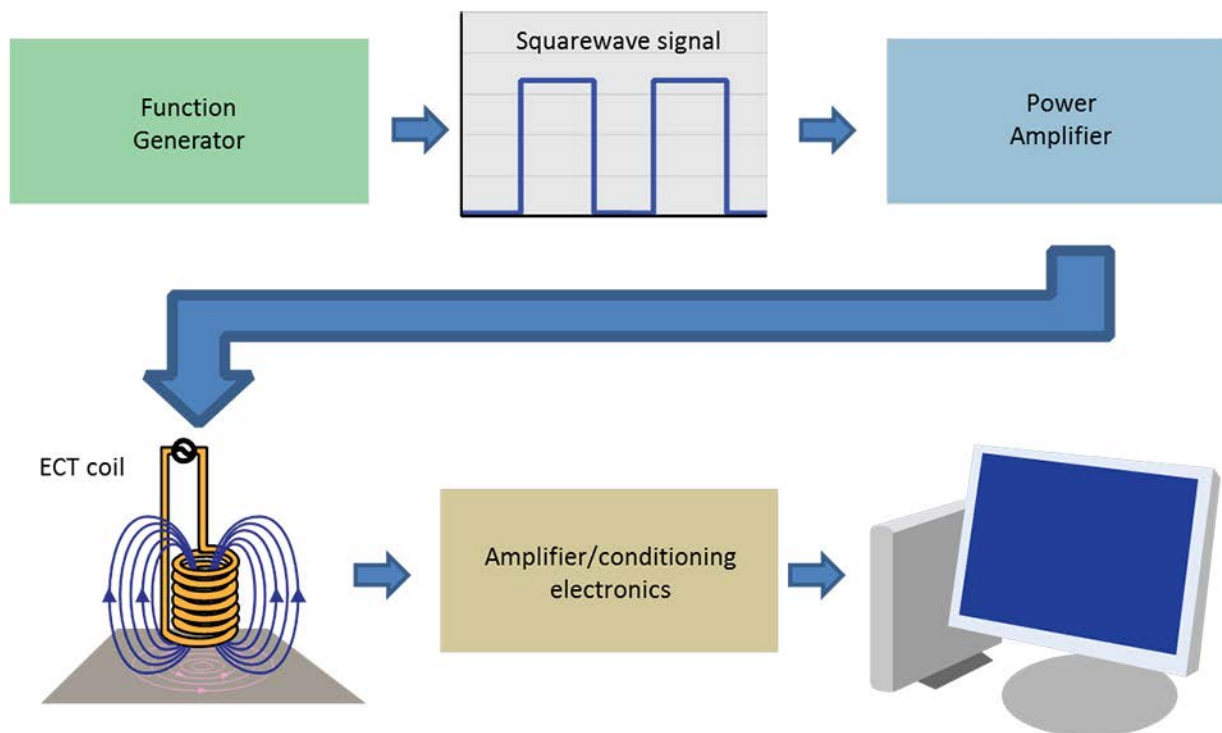
Figure 4-5.   Schematic Showing Configuration for a Typical PEC System Using Pancake Coil Probe

A summary of some key PEC papers with their key parameters and finding is below:

- Yang et al. (2010): GMR probe, double square coil drivers, detects flaws 10-mm deep

- Tian and Sophian (2005): Study of liftoff effect, probe type not specified

- Tian et al. (2013): Hall probe, rectangular driver coil, 50% duty cycle

- Tian et al. (2005): Hall probe, three probes oriented 120° from each other generate information that can be used to look at subsurface defects and classify flaws—3D imaging is suggested but not demonstrated

- Park et al. (2013): Double-D configuration using two driver coils each with a Hall probe inside, subsurface cracks sized resolving 0.5-mm depth difference

- Smetana et al. (2008): Single pancake coil as both driver and pickup, measures a single notch 0.4-mm deep, about 31% duty cycle at 125 kHz.

- He et al. (2010): Uses large rectangular drive coil with small pancake pickup coil, drive coil axis is parallel to surface, 50% duty cycle at 100 Hz, measures defects of different widths, same depths

- Moulder et al. (1996): Talks about time gating C-scan data in order to isolate specific depth information. They use a coil probe rastered over a large surface achieving 3-mm spatial resolution.

- Morozov et al. (2010): Uses rectangular coil on its side for excitation with a Hall sensor probe to measure strain in aluminum wire. 50% pulse duty cycle at 200, 250, and 500 Hz.

- Lebrun et al. (1997): One of the early PEC papers. Uses about 20% duty cycle at 20 Hz with a 26-mm diameter excitation coil and two Hall sensor pickups. Argues that Hall sensors are better than pickup coils because they directly measure magnetic field instead of its derivative. Observes cracks at 5-mm depth that are as narrow as 1.4 mm.

- Kral et al. (2013): Used excitation coil wrapped around GMR to explore lift-off.

- Chen et al. (2009): Uses concentric excitation and pickup coils to estimate aluminum plate thicknesses from 1 to 7 mm with accuracy to a few percent. Uses 10% duty cycle with 25-Hz repetition.

5.   SUMMARY, CONCLUSIONS, AND FUTURE EFFORTS

In FY2014, laboratory work was performed in an effort to validate 2013 FEM modeling analysis of a multi-frequency eddy current technique for crack depth sizing. In FY2013, the goal of FEM analysis was identifying eddy current signal features that could be useful for characterizing SCC flaws and to delineate the effects of notch depth, equivalent conductivity, and equivalent width based on models of SCC flaws proposed by Yusa and Miya (2009). The measurement results presented in this report were performed to verify the curve features observed in FEM results and to validate FEM modeling as a tool for exploring eddy current for crack depth sizing. Reasonably good agreement has been observed between FEM data and laboratory measurements, showing that the physical eddy current probes can be accurately modeled in FEM software. Further, the measurement data collected confirms features and trends in curves of impedance versus frequency, which is observed in FEM results reported in FY2013. A comparison of measurement data obtained from EDM notches with thermal fatigue cracks in specimens B117 and B118 indicate that the depth of the crack in B117 is 3 mm–4 mm and the depth of the crack in B118 is between 4 mm and 7 mm. A comparison of measurement data with the conclusions made based on FEM analysis conducted in FY2013 indicates that the thermal fatigue cracks have a very low effective conductivity, although it is probably not 0%.

An overview is also provided of advanced eddy current instrumentation and concepts in an effort to identify alternative technologies that could result in improved performance. The overview considered different pickup sensor types such as Hall-effect, GMR, and SQIDs. These sensors can provide improved field sensitivity, spatial resolution, and sensitivity to field direction. In addition, advanced concepts are considered, such as pulsed eddy current and eddy current probes with more complex sensor configurations in comparison to the single coil absolute probe that has been the subject of FEM and laboratory assessment. The overview highlights the diversity of eddy current probe concepts and configurations and that eddy current probe design is very much an "art." The documented information on environmental tolerance of pickup sensors indicates that Hall effect sensors and GMR sensors exist that should be able to tolerate the temperatures near dry storage canisters. Documentation of radiation tolerance of GMR sensors indicates that they should also be able to survive the gamma radiation. For Hall effect sensors, it is less clear, although specifications for radiation-tolerant Hall sensors indicate that they are insensitive to gamma radiation, although it is not quantitatively defined.

Suggestions for future efforts related to development of an eddy current technology for depth sizing stress corrosion cracks in dry storage canisters include:

- Determine the true state of thermal fatigue cracks in specimens B117 and B118 for comparison to predictions of crack depth documented here.

- Collect multi-frequency data on specimens with SCC. Data obtained to date on thermal fatigue cracks is encouraging, but thermal fatigue cracks are expected to produce eddy current responses that are distinct from SCC. Although SCC and thermal fatigue flaws are similar in that they both can be characterized by a small COD, the surface of the crack face for thermal fatigue cracks is smooth, whereas the surface of the crack face for SCC is rough. Thus, there tends to be greater contact between the crack faces of SCC and an expected greater effective conductivity.

- Extend assessment of multi-frequency eddy current technique for crack depth sizing by considering a wider range of frequencies (i.e., greater than 100 kHz).

- Begin to design and assess advanced eddy current probe concepts for sizing, such as probes consisting of multiple Hall-effect or GMR pickup sensors and pulsed eddy current concepts.

Instrumentation: Nondestructive Examination for Verification of Canister and Cladding Integrity – FY2014 Status Update

September 12, 2014   35

6. REFERENCES

Abderrahmane A, S Koide, S-I Sato, T Ohshima, A Sandhu and H Okada. 2012. "Robust Hall Effect Magnetic Field Sensors for Operation at High Temperatures and in Harsh Radiation Environments." *IEEE Transactions on Magnetics* 48:4421-4423.

Abidin IZ, C Mandache, GY Tian and M Morozov. 2009. "Pulsed Eddy Current Testing with Variable Duty Cycle on Rivet Joints." *NDT & E International* 42:599-605.

Auld BA, JC Moulder, S Jefferies, PJ Shull, S Ayter and J Kenney. 1989. "Eddy-Current Reflection Probes: Theory and Experiment." *Research in Nondestructive Evaluation* 1:1-11.

Babbar VK, PP Whalen and TW Krause. 2012. "Pulsed Eddy Current Probe Development to Detect Inner Layer Cracks near Ferrous Fasteners Using COMSOL Modeling Software." In *2012 COMSOL Conference*, Boston, MA.

Boltz ES, DW Culter and TC Tiernan. 1998. "Low-Frequency Magnetoresistive Eddy-Current Sensors for NDE of Aging Aircraft." *Proceedings of SPIE* 3397:39-49.

Braginski AI and H-J Krause. 2000. "Nondestructive Evaluation Using High-temperature SQUIDs." *Physica C* 335:179-183.

Chady T and M Enokizono. 1999. "Crack Detection and Recognition Using an Eddy Current Differential Probe." *IEEE Transactions on Magnetics* 35:1849-1852.

Chady T and M Enokizono. 2000. "Multi-frequency Exciting and Spectrogram-based ECT Method." *Journal of Magnetism and Magnetic Materials* 215-216:700-703.

Chady T, M Enokizono, R Sikora, T Todaka and Y Tsuchida. 2001. "Natural Crack Recognition Using Inverse Neural Model and Multi-Frequency Eddy Current Method." *IEEE Transactions on Magnetics* 37:2797-2799.

Chen D, Q Ji, H Zhang and L Zhao. 2009. "Application of Pulsed Eddy Current in Plate Thickness Evaluation." In *4th IEEE Conference on Industrial Electronics and Applications*, pp. 3277-3279 Xian, China. IEEE.

Chieh JJ, IS Lin, HE Horng, C-Y Hong, SY Yang and HC Yang. 2010. "Scanning Waveform Analysis of a Room-temperature-probe SQUID NDE System." *NDT & E International* 43:586-590.

Diaz AA, RA Mathews, J Hixon and SR Doctor. 2007. *Assessment of Eddy Current Testing for the Detection of Cracks in Cast Stainless Steel Reactor Piping Components*. NUREG/CR-6929, Pacific Northwest National Laboratory, Richland, Washington.

Dogaru T and ST Smith. 2001. "Giant Magnetoresistance-Based Eddy-Current Sensor." *IEEE Transactions on Magnetics* 37:3831-3838.

Fava JO, L Lanzani and MC Ruch. 2009. "Multilayer Planar Rectangular Coils for Eddy
Current Testing: Design Considerations." *NDT & E International* 42:713-720.

Garcia-Martin J, J Gomez-Gil and E Vazquez-Sanchez. 2011. "Non-Destructive Techniques
Based on Eddy Current Testing." *Sensors* 11:2525-2565.

Germano J, VC Martins, FA Cardoso, TM Almeida, L Sousa, PP Freitas and M Piedade. 2009.
"A Portable and Autonomous Magnetic Detection Platform for Biosensing." *Sensors* 9:4119-
4137.

Hanysz EA. 1958. "Swept Frequency Eddy Current Device to Measure Overlay Thickness."
Review of Scientific Instruments 29:411-415.

He Y, F Luo and M Pan. 2010. "Defect Characterisation Based on Pulsed Eddy Current
Imaging Technique." *Sensors and Actuators A* 164:1-7.

Helifa B, A Oulhadj, A Benbelghit, IK Lefkaier, F Boubenider and D Boutassouna. 2006.
"Detection and Measurement of Surface Cracks in Ferromagnetic Materials Using Eddy Current
Testing." *NDT & E International* 39:384-390.

Jankowski J, S El-Ahmar and M Oszwaldowski. 2011. "Hall Sensors for Extreme
Temperatures." *Sensors* 11:876-885.

Janousek L, K Capova, N Yusa and K Miya. 2008. "Multiprobe Inspection for Enhancing
Sizing Ability in Eddy Current Nondestructive Testing." *IEEE Transactions on Magnetics*
44:1618-1621.

Koelle D, R Kleiner, F Ludwig, E Dantsker and J Clarke. 1999. "High-transition-temperature
Superconducting Quantum Interference Devices." *Reviews of Modern Physics* 71:631-686.

Koyama K, H Hoshikawa and Y Naruse. 2005. "Detecting Weld Line of Steel Material through
Anticorrosion Paint by an Electromagnetic Induction Probe." *Electrical Engineering in Japan*
153:797-802.

Kral J, R Smid, HMG Ramos and AL Ribeiro. 2013. "The Lift-Off Effect in Eddy Currents on
Thickness Modeling and Measurement." *IEEE Transactions on Instrumentation and
Measurement* 62:2043-2049.

Kulke B, R Frye and F Penko. 1989. "Effects of Irradiation on Hall Probe Sensitivity." In *IEEE
Particle Accelerator Conference*, pp. 1993-1995 Chicago, Illinois. IEEE.

Lamtenzan D, G Washer and M Lozev. 2000. "Detection and Sizing of Cracks in Structural
Steel Using the Eddy Current Method."

Lebrun B, Y Jayet and J-C Baboux. 1997. "Pulsed Eddy Current Signal Analysis: Application
to the Experimental Detection and Characterization of Deep Flaws in Highly Conductive
Materials." *NDT & E International* 30:163-170.

Lee J-H, JP Singer and EL Thomas. 2012. "Micro-/Nanostructured Mechanical Metamaterials."
Advanced Materials 24:4782-4810.

Linn JR and JF Floyd. 2007. "High Frequency Rotary Eddy Current Probe Device." Patent
Number US7256577 B2.

Marschman SC. 2014. *Instrumentation Workshop with Industry*. FCRD-UFD-2014-000475,
U.S. Department of Energy, Office of Used Nuclear Fuel Disposition Research and
Development, Fuel Cycle Research & Development, Washington, D.C.

Meyer R, AM Jones, AF Pardini, KM Denslow, SL Crawford and M Larche. 2013a.
*Instrumentation: Nondestructive Examination for Verification of Canister and Cladding
Integrity – FY2013 Status Update*. PNNL-22734, FCRD-UFD-000337, Pacific Northwest
National Laboratory, Richland, Washington.

Meyer R, A Pardini, J Cuta, H Adkins, A Casella, A Qiao, MR Larche, A Diaz and SR Doctor.
2013b. *NDE to Manage Atmospheric SCC in Canisters for Dry Storage of Spent Fuel: An
Assessment*. PNNL-22495, Pacific Northwest National Laboratory, Richland, Washington.
ADAMS Accession No. ML13276A196.

Meyer R, A Pardini, B Hanson and K Sorenson. 2013c. *Review of NDE Methods for Detection
and Monitoring of Atmospheric SCC in Welded Canisters for the Storage of Used Nuclear Fuel*.
PNNL-22158, FCRD-UFD-000085, Pacific Northwest National Laboratory, Richland,
Washington.

Meyer RM, AM Jones and AF Pardini. 2014. "Eddy Current for Sizing Cracks in Canisters for
Dry Storage of Used Nuclear Fuel." In *Proceedings of NACE International Corrosion 2014*.
March 9-13, 2014, San Antonio, Texas. NACE International, Houston, Texas. Paper No. 4166.

Morozov M, GY Tian and PJ Withers. 2010. "The Pulsed Eddy Current Response to Applied
Loading of Various Aluminum Alloys." *NDT & E International* 43:493-500.

Moulder JC, JA Bieber, WW Ward and JH Rose. 1996. "Scanned Pulsed Eddy Current
Instrument for Nondestructive Inspection of Aging Aircraft." *Proceedings of SPIE* 2945:2-13.

Muck M, M von Kreutzbruck, U Baby, J Troll and C Heiden. 1997. "Eddy Current
Nondestructive Material Evaluation based on HTS SQUIDs." *Physica C* 282-287:407-410.

Myers DR, JR Jessing, OB Spahn and MR Shaneyfelt. 2000. *Investigations of the Impact of the
Process Integration of Deposited Magnetic Films for Magnetic Memory Technologies on
Radiation Hardened CMOS Devices and Circuits*. SAND2000-0218, Sandia National
Laboratories, Albuquerque, New Mexico.

Park D-G, CS Angani, BPC Rao, G Vertesy, D-H Lee and K-H Kim. 2013. "Detection of the
Subsurface Cracks in a Stainless Steel Plate Using Pulsed Eddy Current." *Journal of
Nondestructive Evaluation* 32:350-353.

Serway RA and RJ Beichner. 2000. *Physics for Scientists and Engineers*. Saunders College Publishing, Orlando, Florida.

Smetana M, T Strapacova and L Janousek. 2008. "Pulsed Excitation in Eddy Current Non-destructive Testing of Conductive Materials." *Advances in Electrical and Electronic Engineering* 7:326-329.

Tamanaha CR, SP Mulvaney, JC Rife and LJ Whitman. 2008. "Magnetic Labeling, Detection, and System Integration." *Biosensors and Bioelectronics* 24:1-13.

Tian GY, M Morozov and S Takahashi. 2013. "Pulsed Eddy Current Testing of Thermally Aged and Cold-Rolled Fe-Cu Alloys." *IEEE Transactions on Magnetics* 49:517-523.

Tian GY and A Sophian. 2005. "Reduction of Lift-off Effects for Pulsed Eddy Current NDT." *NDT & E International* 38:319-324.

Tian GY, A Sophian, D Taylor and J Rudlin. 2005. "Multiple Sensors on Pulsed Eddy-Current Detection for 3-D Subsurface Crack Assessment." *IEEE Sensors Journal* 5(1):90-96.

Yang G, A Tamburrino, L Udpa, SS Udpa, Z Zeng, Y Deng and P Que. 2010. "Pulsed Eddy-Current Based Giant Magnetoresistive System for the Inspection of Aircraft Structures." *IEEE Transactions on Magnetics* 46:910-917.

Yusa N, H Hashizume, R Urayama, T Uchimoto, T Takagi and K Sato. 2014. "An Arrayed Uniform Eddy Current Probe Design for Crack Monitoring and Sizing of Surface Breaking Cracks with the Aid of a Computation Inversion Technique." *NDT & E International* 61:29-34.

Yusa N and K Miya. 2009. "Discussion on the Equivalent Conductivity and Resistance of Stress Corrosion Cracks in Eddy Current Simulations." *NDT & E International* 42(1):9-15.

Instrumentation: Nondestructive Examination for Verification of Canister and Cladding Integrity – FY2014 Status Update

September 12, 2014   A-1

Appendix A: Passive Optical Impurity Monitoring of Dry Storage Containers for Spent Fuel

Passive Optical Impurity Monitoring of Dry Storage Containers for Spent Fuel

Ryan M. Meyer, Andrew M. Casella, Jonathan D. Suter, Hong Qiao, Norm C. Anheier

Pacific Northwest National Laboratory: 902 Battelle Blvd., Richland, WA, 99354, Ryan.Meyer@pnnl.gov

Mark A. Prelas

University of Missouri-Columbia: E2433 Lafferre Hall, Columbia, MO, 65211, PrelasM@missouri.edu

INTRODUCTION

This paper proposes a technique for passively monitoring impurities in dry storage containers (DSCs) for spent nuclear fuel. This method is based on the measurement of optical emission induced by gamma rays coming from the bundled fuel elements. The principles of this method have been demonstrated in the field of nuclear pumped lasers. Low level optical emissions from gases being excited by ionizing radiation are at the center of this method, and a body of work is available in which low level optical emission has been used to identify specific lines from atoms or molecules present in gas mixtures [1-6].

Impurities of interest for monitoring in DSCs include water vapor and fission gases. In DSCs, spent fuel elements are immersed in an inert gas atmosphere (usually He) to inhibit corrosion of the fuel cladding. This maintains the structural integrity of the spent fuel and prevents the release of fuel element contents. The eventual retrieval process of spent fuel from DSCs can be significantly impacted by cladding failures and potential dispersion of fuel rod contents. The potential for corrosion of fuel rod cladding exists as a result of imperfect drying procedures that may leave some water remaining in DSCs after they have been sealed. Timely detection of water vapor products and fission gases, as a result of cladding degradation, can facilitate engineering the retrieval of fuel elements at the end of the dry storage term.

The technical background for the proposed technique is provided in the next section followed by modeling and simulation analysis to illustrate the feasibility of the concept. Implementation is a significant challenge for most monitoring techniques proposed for DSCs, thus, a discussion of potential implementation strategies is also provided.

TECHNICAL BACKGROUND

In DSCs back filled with helium gas, gamma radiation inside the canister will ionize the helium gas to produce helium ions and electrons [5]. The helium ions undergo a complex set of reactions, which are dependent on the impurities in the gas mix. Once the gamma radiation interacts with the helium, the dominant channel leads to the formation of the helium metastable state. The series of plasma kinetic equations that leads to spontaneous emissions from Kr and water vapor impurities starts with the reaction for producing He_2^+ ions,

$$He^+ + 2\,He \rightarrow He_2^+ + He. \qquad (1)$$
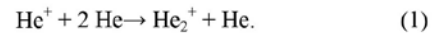
$He(2^3S)$ and $He(2^1S)$ are metastable states, however, the $He(2^1S)$ state quickly converts to the $He(2^3S)$ state through collisions [2]. The reaction for producing the $He(2^3S)$ metastable (He*) state is,

$$He_2^+ + e^- \rightarrow He^* + He. \qquad (2)$$
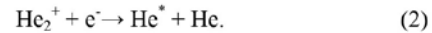
The metastable He then ionizes the impurities to produce Kr ions and H ions,

$$He^* + Kr \rightarrow Kr^+ + e^- + He, \qquad (3)$$
$$He^* + H_2O \rightarrow H^+ + OH^- + He. \qquad (4)$$
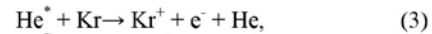
Three-body recombination involving Kr and H ions produces neutral excited states in Kr and H which decay by spontaneous emission. Table I summarizes the rate constants for the reactions in equations (1) – (4) [6–8].

Table I. Rate constants for equations (1) – (4) [6-8].

Equation	Rate Constant
(1)	8.7×10^{-32} $cm^3 s^{-1}$
(2)	1.8×10^{-8} $cm^3 s^{-1}$
(3)	2.2×10^{-10} $cm^3 s^{-1}$
(4)	7.8×10^{-10} $cm^3 s^{-1}$

The production rates for helium ions and helium metastable states are based on the power deposited in the helium fill gas by gamma radiation. These production rates can be expressed as,

$$\text{Helium Ion Production Rate} = P_d/W, \text{ and,} \qquad (5)$$

$$\text{Helium Metastable Production Rate} = P_d/W^*. \qquad (6)$$

P_d is power density, W is the average energy to produce an ion pair, and W^* is the average energy to produce a metastable atom. For helium, W has a value of

**Instrumentation: Nondestructive Examination for Verification of Canister and Cladding Integrity –
FY2014 Status Update**

A-2   September 12, 2014

30 eV/ion-pair, and W^* has a value of 90eV/metastable [2,6].

INITIAL FEASIBILITY ASSESSMENT

Monte Carlo N-Particle eXtended (MCNPX) calculations indicate that 0.05% - 0.27% of the gamma energy released from the spent fuel in the container will be deposited in the backfill He gas over a pressure range of 1-5 atm. Table II summarizes the results of these MCNPX calculations. This data indicates that the power deposition is essentially proportional to the He pressure and the deposited power varies from approximately 10 $\mu W/cm^3$ to 0.1 $\mu W/cm^3$ from storage periods from 5 to 100 years, respectively.

The data from Table II is combined with Eqs. (1) – (6) to estimate the amount of spontaneous emission from Kr impurities varying in concentration from 0.4 parts per trillion to 4 parts per million. This is shown in Figure 1

for three scenarios based on power densities ranging from 0.1 $\mu W/cm^3$ to 10 $\mu W/cm^3$ to represent spent fuel storage from 5 to 100 years. The amount photons collected by the detector is estimated assuming a 2.54 cm radius window in a port in the canister looking down a chord approximately 180 cm long. The light will be collected using a lens focused on a fiber optic cable.

The minimum detectable signal is limited by sources of noise for the detectors and the quantum efficiency. In this application, background light sources should have minimal influence and dark current will be the major contribution. To be conservative, 1×10^8 photons/sec is set as the detectable signal level threshold for this analysis and is represented by the bottom line of the y axis in Figure 1. The model shows that Kr can be detected at very low concentrations even at a power density of 0.1 $\mu W/cm^3$.

Table II. Power density deposition for several potential dry storage conditions.

Time (year)	$\mu W/cm^3$, 1 atm of He	$\mu W/cm^3$, 2 atm of He	$\mu W/cm^3$, 5 atm of He
0	8.04E+01	1.61E+02	4.01E+02
5	1.62E+00	3.24E+00	8.09E+00
10	9.69E-01	1.94E+00	4.84E+00
30	5.27E-01	1.05E+00	2.63E+00
50	3.30E-01	6.59E-01	1.65E+00
100	1.09E-01	2.19E-01	5.46E-01
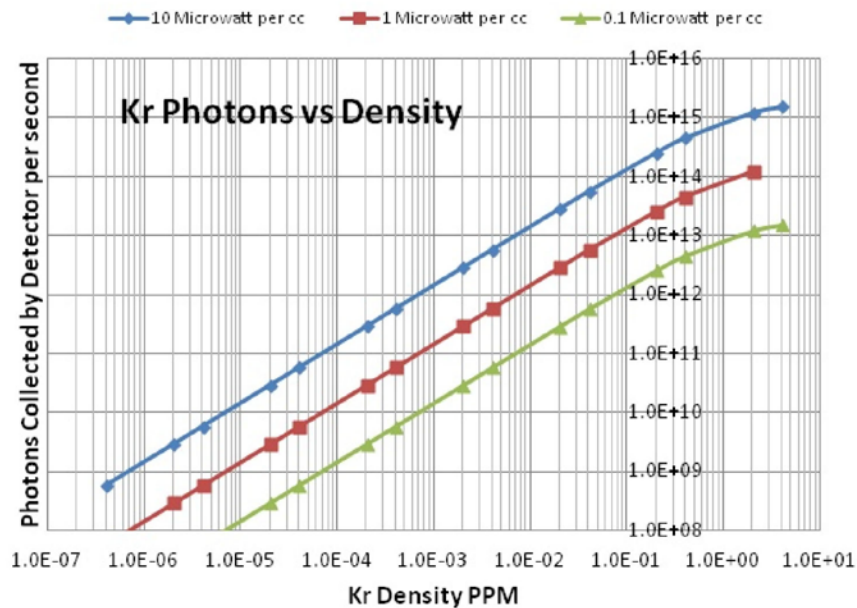
Fig. 1. Krypton photons collected for Kr concentration varying from 0.4 parts per trillion to 4 parts per million.

IMPLEMENTATION

The predominant excited states of Kr produced in a weak plasma will have strong neutral lines in the range of 500 nm to 900 nm [9]. These lines will be monitored by using a spectrometer with CCD array that is designed to look at a broad spectrum, from 300 nm to 1070 nm. Strong singly ionized emission lines are also present below 500 nm. Trace amounts of water vapor can also be monitored by looking at hydrogen lines from 300 nm to 700 nm [9].

An extensive review of commercial optical materials and measurement systems has been performed for application to advanced small modular reactors [10]. This knowledge can be leveraged for developing concepts to provide optical access to DSCs. A sapphire window is a feasible choice for DSC monitoring, although lower cost silica windows may also be suitable. The commercial-off-the-shelf (COTS) availability of sapphire windows is rated very high along with windows fabricated from CVD diamond and fused silica. Sapphire windows are much less expensive than CVD diamond windows and are known to be more resistant to radiation damage than fused silica. Sapphire exhibits no measureable optical absorption under gamma radiation exposure up to doses of 10^{10} Rad [11]. Silica is transparent into the near infrared, while sapphire and diamond transmit well into the mid infrared or beyond (in the case of diamond).

The most common commercial solution for sealing sapphire viewports is optical-to-metal brazing. Brazed sapphire viewports are available as COTS products that can usually tolerate temperatures up to 450°C and pressures up to tens of MPa. Brazed seal designs do not rely on compressional forces to form the hermitic seal. The metal viewport flange must have a coefficient of thermal expansion (CTE) nearly matched with sapphire so that the brazed joint can sustain full temperature fluctuations without failure. For this reason, viewport windows are seldom brazed directly to a metal steel flange.   An intermediate transition metal sleeve, with closely matching CTE, is brazed to sapphire and laser- or electron-beam welded to the stainless steel flange. The metal sleeve is flexible and is formed in a variety of shapes to accommodate differential expansion and contraction.   An illustration of a proposed sapphire window port to facilitate optical access to the interior of a DSC is provided in Figure 2.

Figure 3 provides an illustration of how the window port and monitoring system may be implemented on a DSC. In this case, a fiber optic cable flange is attached above the sapphire window port. A lens helps focus emissions through the window into the fiber optic cable. The fiber optic cable allows the spectrometer and detector components to be located remotely from the window viewport. The thickness of the fiber optic cable flange may be varied to help mitigate concerns related to worker dose. Alternatively, an additional shield flange could be installed above the fiber optic flange and/or a thick window could be installed.
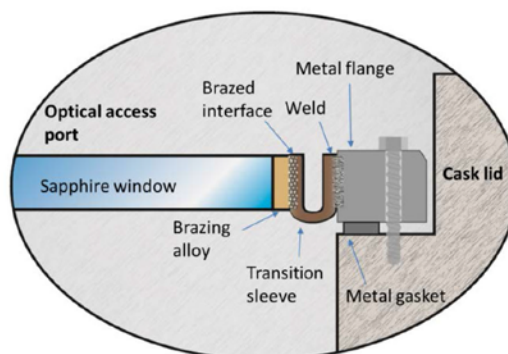
Fig. 2. Illustration of a proposed sapphire window port to enable optical access to the interior of DSCs.
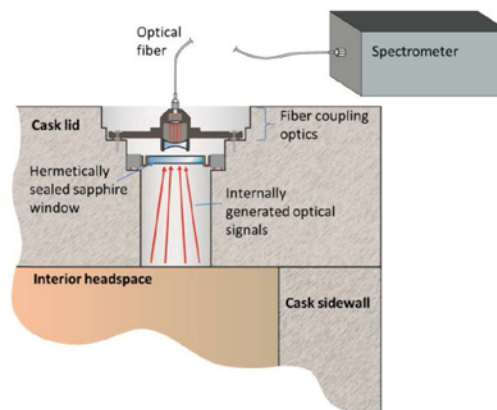
Fig. 3. Depiction of fiber optic cable flange and optical window port implemented in a DSC lid. Use of fiber optic cable enables remote locating of the spectrometer and detector components with respect to the window port.

Retrofitting existing DSCs in the field to accommodate optical window access is unlikely. Thus, opportunities for deployment of this technology should focus on future container designs that may be able to incorporate window viewports. In this case, it may still not be viable to implement optical windows on DSCs on a wide-scale. However, opportunities for implementation on a small sample of DSCs could still be considered. Demonstration projects provide unique opportunities for deployment of the proposed technology [12,13]. In addition, implementation of optical windows on a small sample of DSCs in the field is also conceivable.

Instrumentation: Nondestructive Examination for Verification of Canister and Cladding Integrity – FY2014 Status Update

A-4   September 12, 2014

CONCLUSIONS

Passive optical impurity monitoring of DSCs for spent fuel can help ensure public safety during storage and the effective retrieval of spent fuel at the end of storage periods. Laboratory scale testing is needed to validate the results of the analysis presented in this paper and to assess COTS instrumentation performance for this application (e.g. spectrometers, detectors). In addition, calibration procedures to enable quantification of impurity concentrations over relevant ranges can be developed. Accessibility is a key challenge to the deployment of this technology on DSCs. Implementation strategies must balance the safety implications of enabling optical access to the internal of DSCs with the benefits provided by optical impurity monitoring.

ACKNOWLEDGEMENTS

REFERENCES

1. M.A. PRELAS and G.H. MILEY, "Dynamics of the Nuclear and Electrical Pumped 1.45 micrometer Atomic Carbon Laser in Mixtures of He-CO_2," *Nuclear Tech./Fusion,* **1**(3), 473-483 (1981).

2. M.J. LECOURS, M.A. PRELAS, S. GUNN, C. EDWARDS, and G. SCHLAPPER, "The Design, Construction and Testing of a Nuclear-Pumping Facility at the University of Missouri Research Reactor," *Rev. Sci. Instrum.*, **53**(7), 952-956 (1982).

3. F.P. BOODY and M.A. PRELAS, "Absolutely Calibrated Spectra of Nuclear-Driven Rare Gases, 400-950 nm," Proceedings of Specialist Conference on Physics of Nuclear Induced Plasmas and Problems of Nuclear-Pumped Lasers, Institute of Physics and Power Engineering, Obninsk, USSR (May 26-28, 1992) [http://prelas.nuclear.missouri.edu/Publications/NPL%20 Symposium%201992%20Vol%202%20Absolutely%20C alibrated%20Spectra%20FPB-MAP.pdf].

4. F.P. BOODY and M.A. PRELAS, "Efficient Visible Nuclear-Driven Fluorescer Sources," *Proceedings of Specialist Conference on Physics of Nuclear Induced Plasmas and Problems of Nuclear-Pumped Lasers,* Institute of Physics and Power Engineering, Obninsk, USSR (May 26-28, 1992) [http://prelas.nuclear.missouri.edu/Publications/NPL%20 Symposium%201992-

2%20Efficient%20Light%20Transport%20FPB-MAP.pdf].

5. R. SCHOTT, C. WEAVER, M. PRELAS, J. ROTHENBERGER, R. TOMPSON and D. WISNEWSKI, "Photon Intermediate Direct Energy Conversion Using a Sr-90 Beta Source", *Nuclear Technology*, **181**(2), 349-353 (2013).

6. F.P. BOODY and M.A. PRELAS, "Kinetics Model for Pulsed Nuclear-Driven Fluorescers, with Comparison to Experiment," *Proceedings of Specialist Conference on Physics of Nuclear Induced Plasmas and Problems of Nuclear-Pumped Lasers,* Institute of Physics and Power Engineering, Obninsk, USSR (May 26-28, 1992) [http://prelas.nuclear.missouri.edu/Publications/NPL%20 Symposium%201992%20Kinetic%20Model%20FPB-MAP.pdf].

7. D.S. ONG, T.Y. TOU, and K.S. LOW, "Kinetics modelling of a self-sustained discharge KrF laser", *Journal of Physics D: Applied Physics*, **29**, 2586-2594 (1996).

8. C.B. COLLINS and F.W. LEE, "Measurement of the rate coefficients for the bimolecular and termolecular deexcitation reactions of He(23 S) with selected atomic and molecular species", *The Journal of Chemical Physics*, **70**, 1275-1285 (1979).

9. J.E. SANSONETTI and W.C. MARTIN, *Handbook of Basic Atomic Spectroscopic Data*, National Institute of Standards and Technology, http://www.nist.gov/pml/data/handbook/index.cfm

10. N.C. ANHEIER, J.D. SUTER, A. QIAO, E.S. ANDERSON, E.J. BERGLIN, M. BLISS, B.D. CANNON, R. DEVANATHAN, A. MENDOZA, and D.M. SHEEN, "Technical Readiness and Gaps Analysis of Commercial Optical Materials and Measurement Systems for Advanced Small Modular Reactors," SMR/ICHMI/PNNL/TR-2013/04, Pacific Northwest National Laboratory, Richland, WA, (2013).

11. A.K. ISLAMOV, E.M. IBRAGIMOVA and I. NURITDINOV, "Radiation-Optical Characteristics of Quartz Glass and Sapphire," *Journal of Nuclear Materials*, **362**, 222-226 (2007).

12. "The CASTOR-V/21 PWR Spent Fuel Storage Cask: Testing and Analyses," EPRI NP-4887, PNL-5917, Interim Report, prepared by Virginia Power Company, published by the Electric Power Research Institute, Palo Alto CA, (1986).

13. "DOE Issues EPRI Plan for Spent Fuel Storage Demo," http://www.nei.org/News-Media/News/News-Archives/DOE-Issues-EPRI-Plan-for-Spent-Fuel-Storage-Demo, retrieved on January 7, 2014.

Appendix B: Plots of |Z| Obtained from Specimens

B.1   Horizontal Scan Data for EDM Notch #11
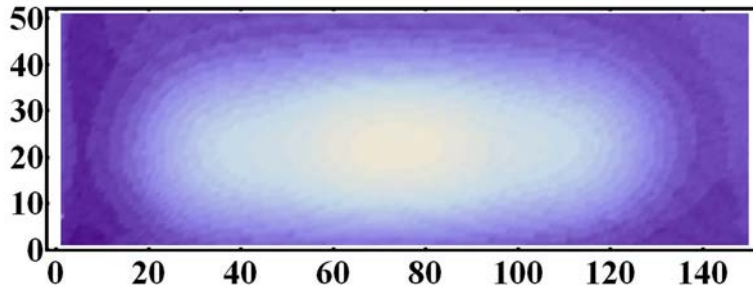
Figure B-1.   Density Plot of |Z| Obtained from Raster Scan of 20 kHz Ferrite Core Probe over
   Notch #11 in Horizontal Direction at 10 kHz
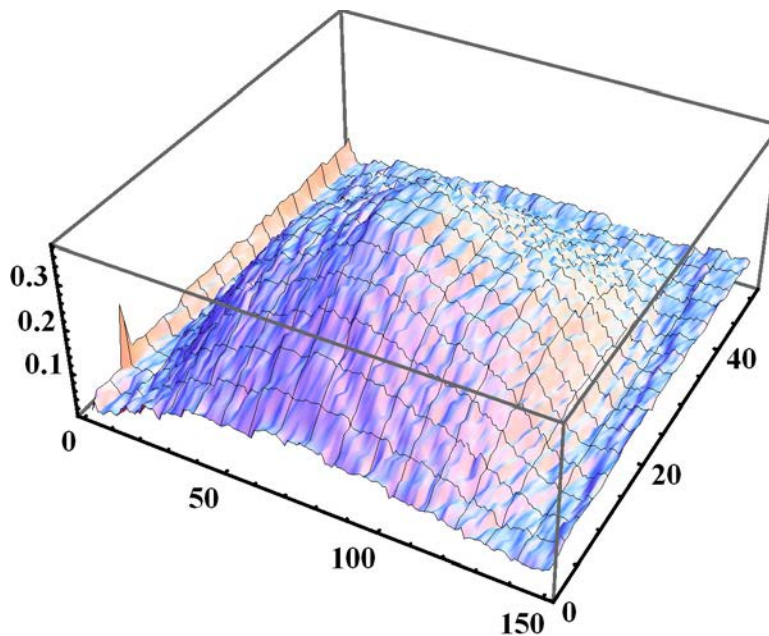
Figure B-2.   3-D Plot of |Z| Obtained from Raster Scan of 20-kHz Ferrite Core Probe over
   Notch #11 in Horizontal Direction at 10 kHz

Instrumentation: Nondestructive Examination for Verification of Canister and Cladding Integrity – FY2014 Status Update

B-2   September 12, 2014
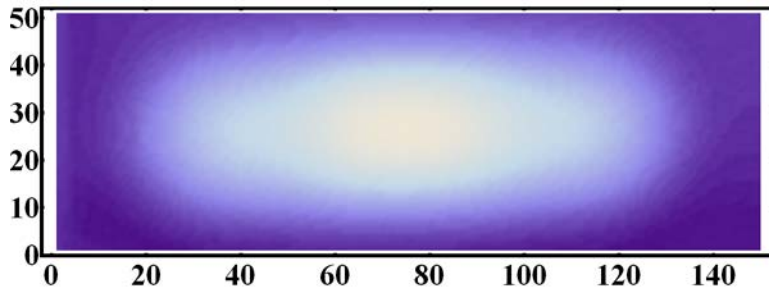
Figure B-3.   Density Plot of |*Z*| Obtained from Raster Scan of 20-kHz Ferrite Core Probe over Notch #11 in Horizontal Direction at 20 kHz
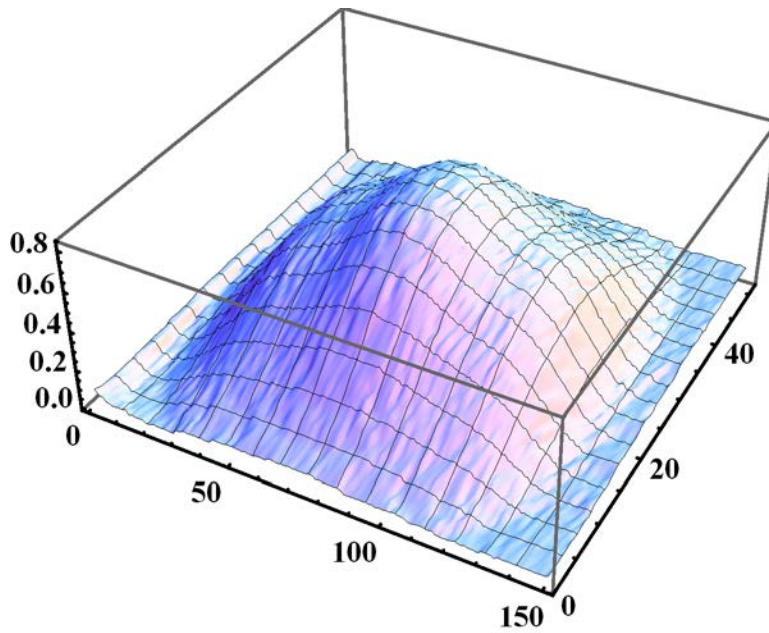

Figure B-4.   3-D Plot of |*Z*| Obtained from Raster Scan of 20-kHz Ferrite Core Probe over Notch #11 in Horizontal Direction at 20 kHz
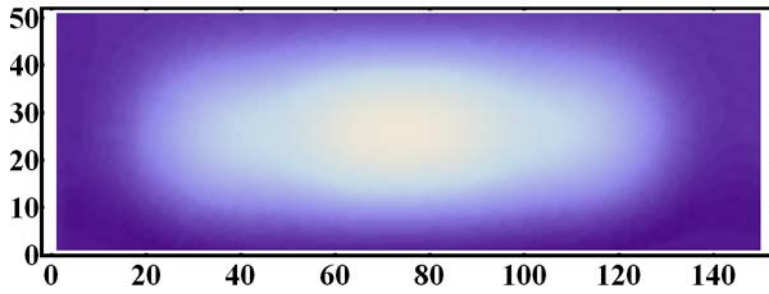
Figure B-5.   Density Plot of |Z| Obtained from Raster Scan of 20-kHz Ferrite Core Probe over
Notch #11 in Horizontal Direction at 30 kHz
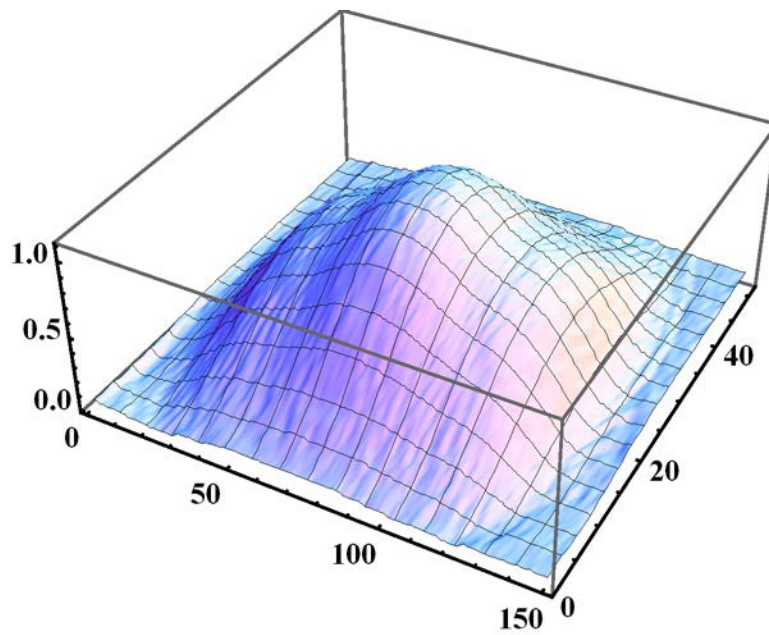
Figure B-6.   3-D Plot of |Z| Obtained from Raster Scan of 20-kHz Ferrite Core Probe over
Notch #11 in Horizontal Direction at 30 kHz
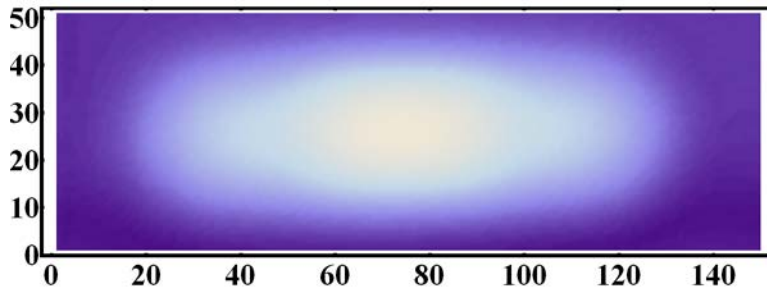
Figure B-7.   Density Plot of |Z| Obtained from Raster Scan of 20-kHz Ferrite Core Probe over Notch #11 in Horizontal Direction at 40 kHz
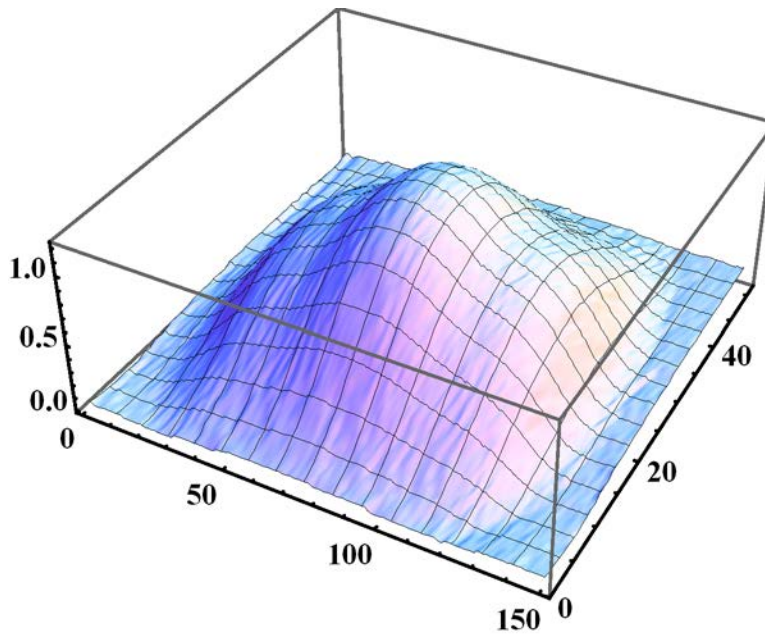
Figure B-8.   3-D Plot of |Z| Obtained from Raster Scan of 20-kHz Ferrite Core Probe over Notch #11 in Horizontal Direction at 40 kHz
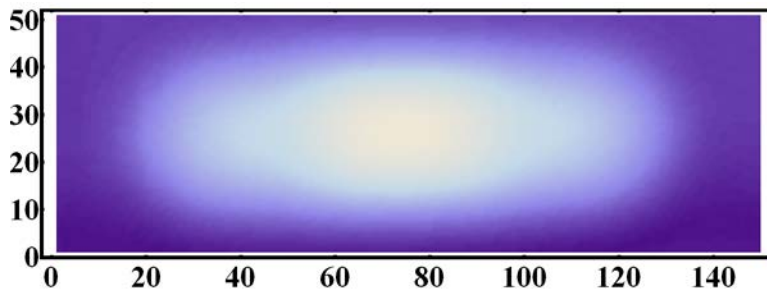
Figure B-9.   Density Plot of |Z| Obtained from Raster Scan of 20-kHz Ferrite Core Probe over Notch #11 in Horizontal Direction at 50 kHz
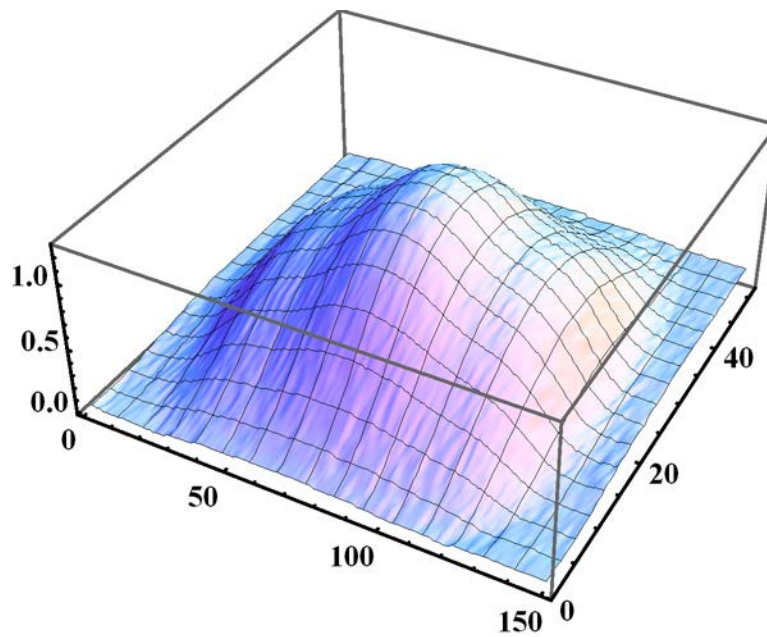

Figure B-10.   3-D Plot of |Z| Obtained from Raster Scan of 20-kHz Ferrite Core Probe over Notch #11 in Horizontal Direction at 50 kHz
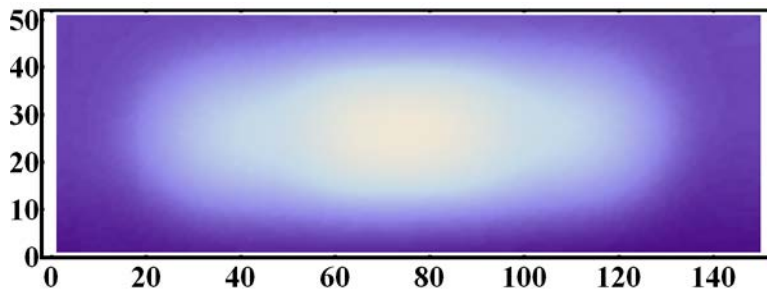
Figure B-11.   Density Plot of |Z| Obtained from Raster Scan of 20-kHz Ferrite Core Probe over
Notch #11 in Horizontal Direction at 60 kHz
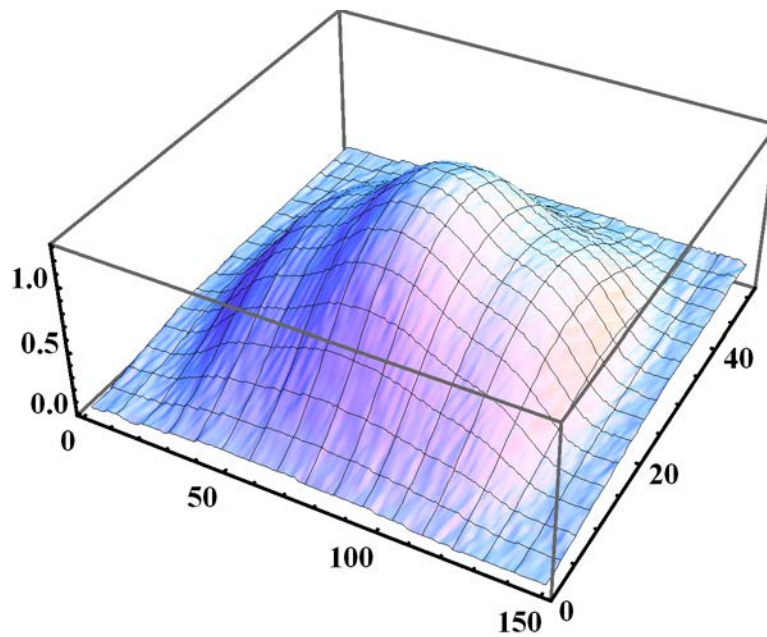
Figure .B-12   3-D Plot of |Z| Obtained from Raster Scan of 20-kHz Ferrite Core Probe over
Notch #11 in Horizontal Direction at 60 kHz
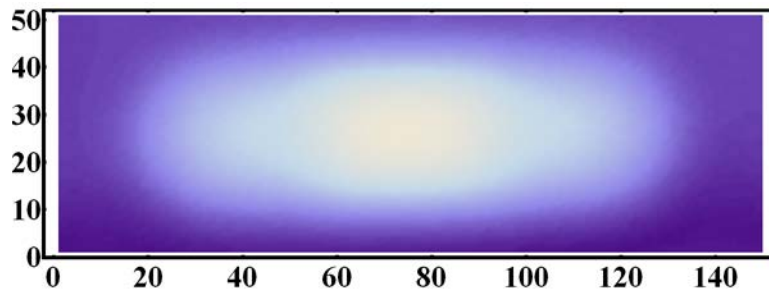
Figure B-13.   Density Plot of |Z| Obtained from Raster Scan of 20-kHz Ferrite Core Probe over Notch #11 in Horizontal Direction at 70 kHz
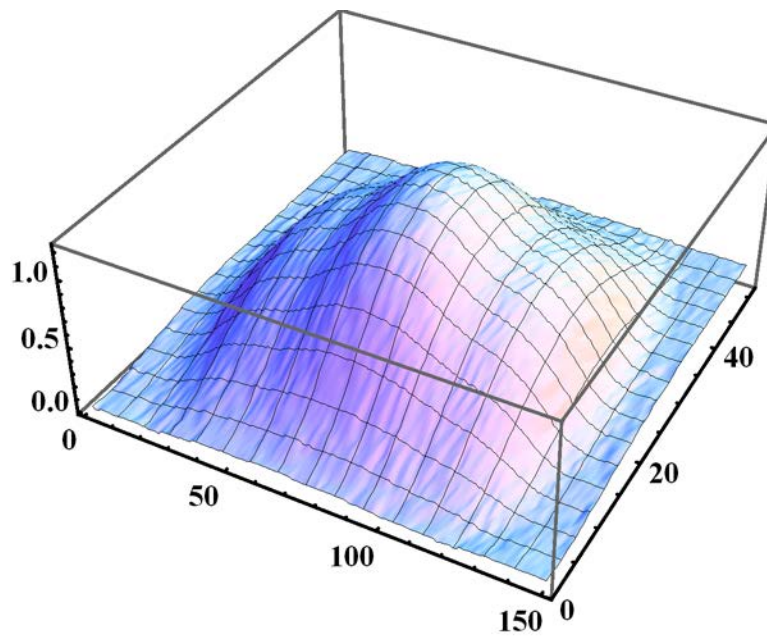
Figure B-14.   3-D Plot of |Z| Obtained from Raster Scan of 20-kHz Ferrite Core Probe over Notch #11 in Horizontal Direction at 70 kHz
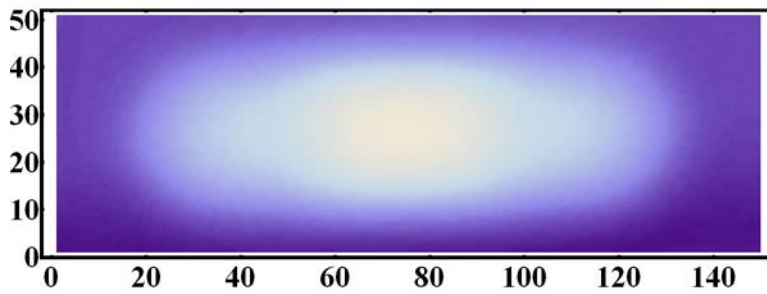
Figure B-15.   Density Plot of |Z| Obtained from Raster Scan of 20-kHz Ferrite Core Probe over
Notch #11 in Horizontal Direction at 80 kHz
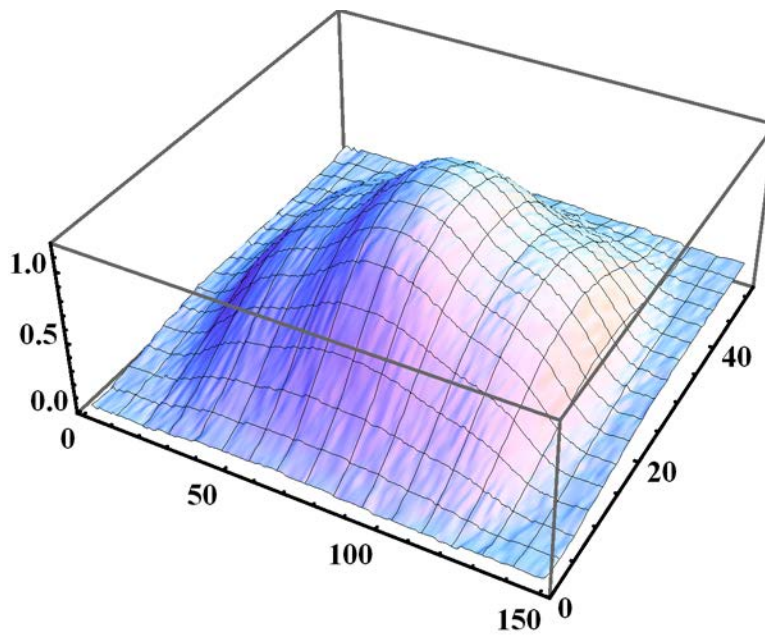
Figure B-16.   3-D Plot of |Z| Obtained from Raster Scan of 20-kHz Ferrite Core Probe over
Notch #11 in Horizontal Direction at 80 kHz
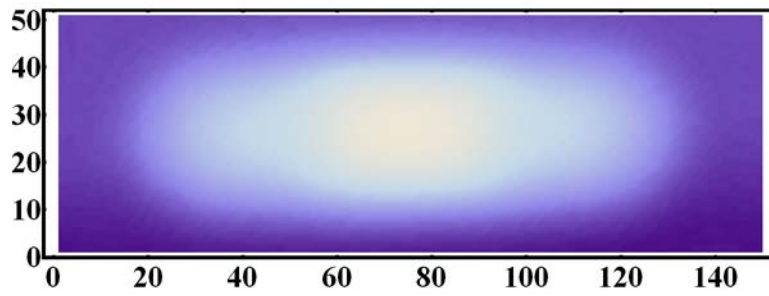
Figure B-17.   Density Plot of |Z| Obtained from Raster Scan of 20-kHz Ferrite Core Probe over Notch #11 in Horizontal Direction at 90 kHz
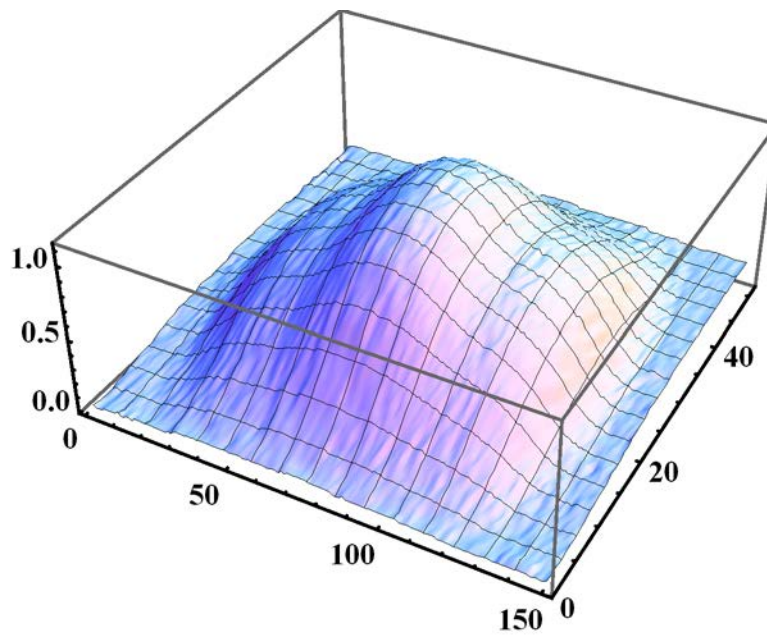

Figure B-18.   3-D Plot of |Z| Obtained from Raster Scan of 20-kHz Ferrite Core Probe over Notch #11 in Horizontal Direction at 90 kHz
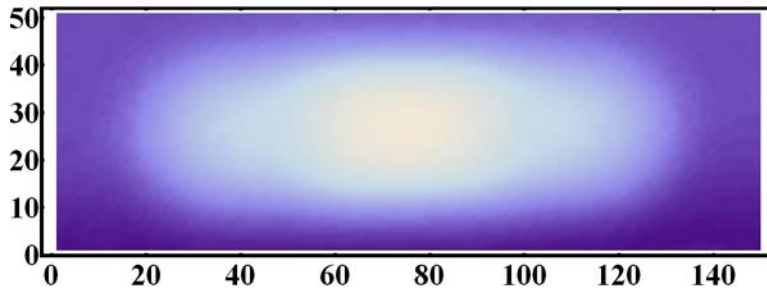
Figure B-19.   Density Plot of |Z| Obtained from Raster Scan of 20-kHz Ferrite Core Probe over
Notch #11 in Horizontal Direction at 100 kHz
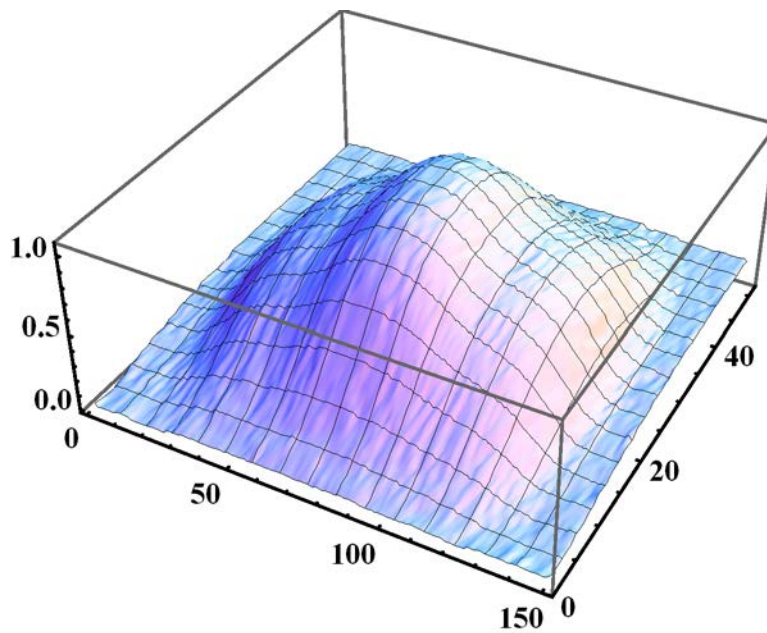
Figure B-20.   3-D Plot of |Z| Obtained from Raster Scan of 20-kHz Ferrite Core Probe over
Notch #11 in Horizontal Direction at 100 kHz

B.2 Vertical Scan Data for EDM Notch #11
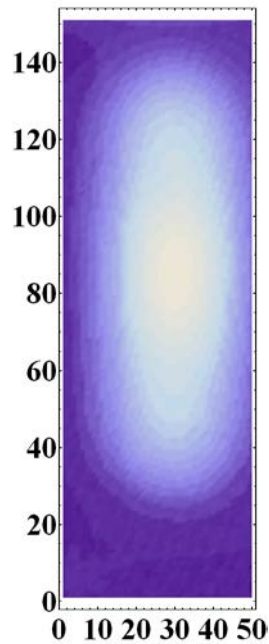
Figure B-21.   Density Plot of |Z| Obtained from Raster Scan of 20-kHz Ferrite Core Probe over Notch #11 in Vertical Direction at 10 kHz
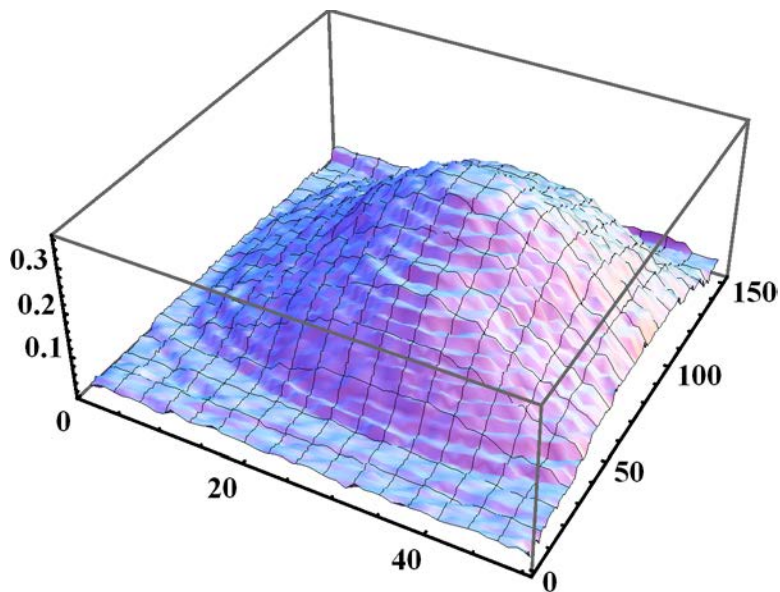

Figure B-22.   3-D Plot of |Z| Obtained from Raster Scan of 20-kHz Ferrite Core Probe over Notch #11 in Vertical Direction at 10 kHz
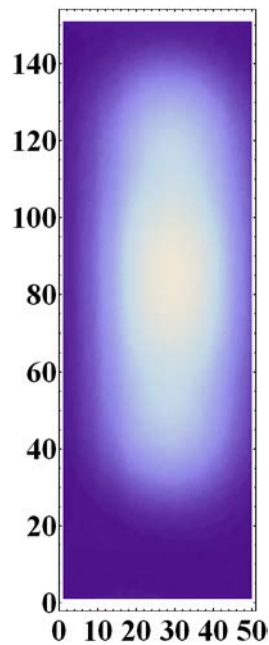
Figure B-23.   Density Plot of |Z| Obtained from Raster Scan of 20-kHz Ferrite Core Probe over
Notch #11 in Vertical Direction at 20 kHz
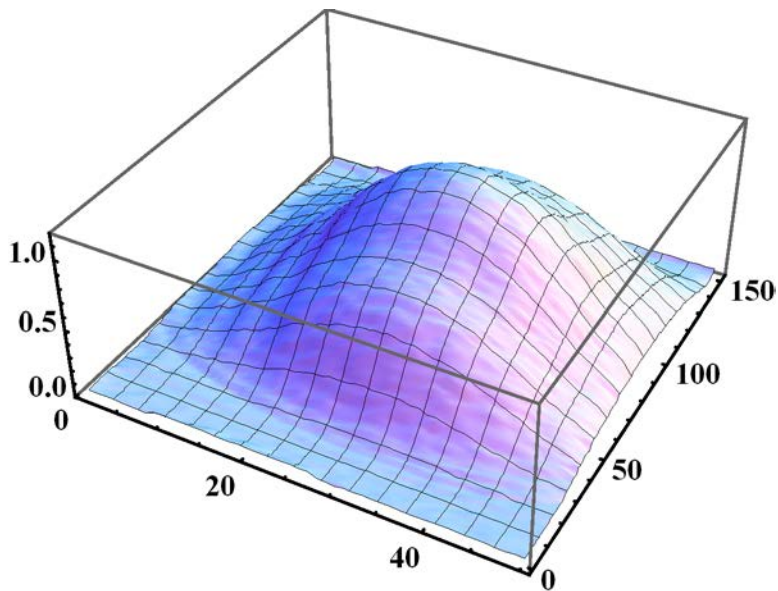
Figure B-24.   3-D Plot of |Z| Obtained from Raster Scan of 20-kHz Ferrite Core Probe over
Notch #11 in Vertical Direction at 20 kHz
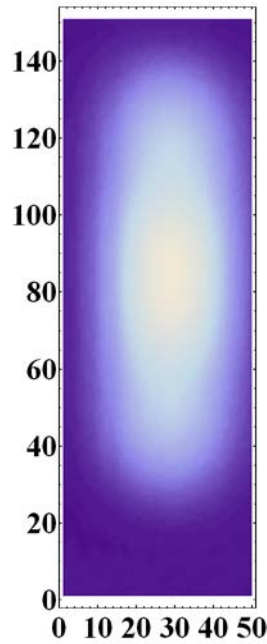
Figure B-25.   Density Plot of |*Z*| Obtained from Raster Scan of 20-kHz Ferrite Core Probe over Notch #11 in Vertical Direction at 30 kHz
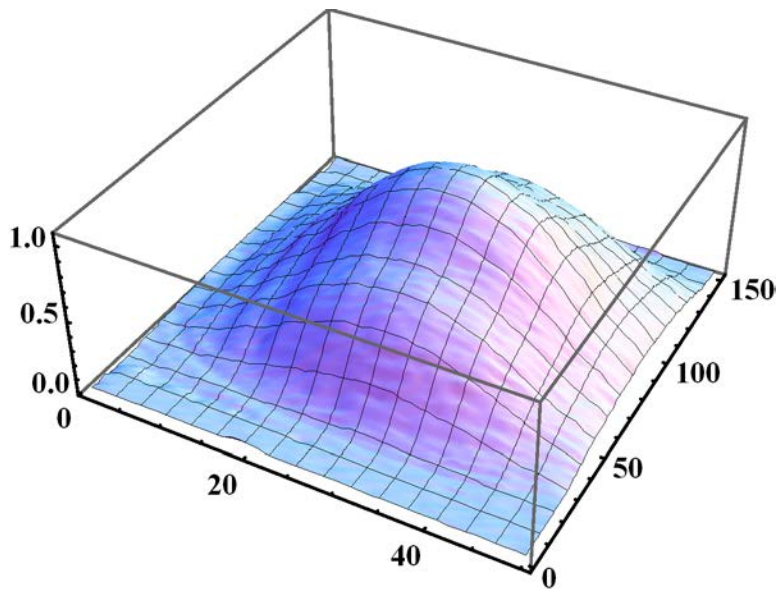
Figure B-26.   3-D Plot of |*Z*| Obtained from Raster Scan of 20-kHz Ferrite Core Probe over Notch #11 in Vertical Direction at 30 kHz

Instrumentation: Nondestructive Examination for Verification of Canister and Cladding Integrity – FY2014 Status Update

B-14   September 12, 2014
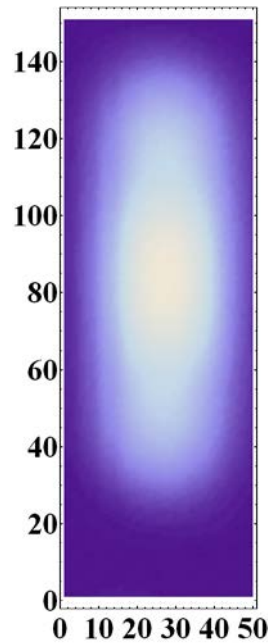
Figure B-27.   Density Plot of |Z| Obtained from Raster Scan of 20-kHz Ferrite Core Probe over Notch #11 in Vertical Direction at 40 kHz
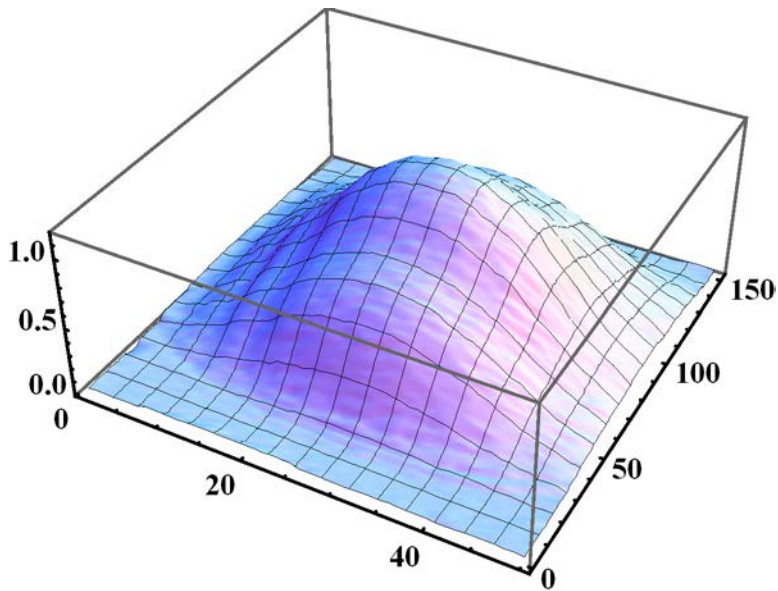

Figure B-28.   3-D Plot of |Z| Obtained from Raster Scan of 20-kHz Ferrite Core Probe over Notch #11 in Vertical Direction at 40 kHz
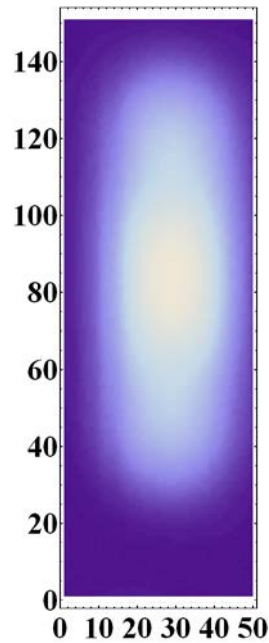
Figure B-29.   Density Plot of |*Z*| Obtained from Raster Scan of 20-kHz Ferrite Core Probe over Notch #11 in Vertical Direction at 50 kHz
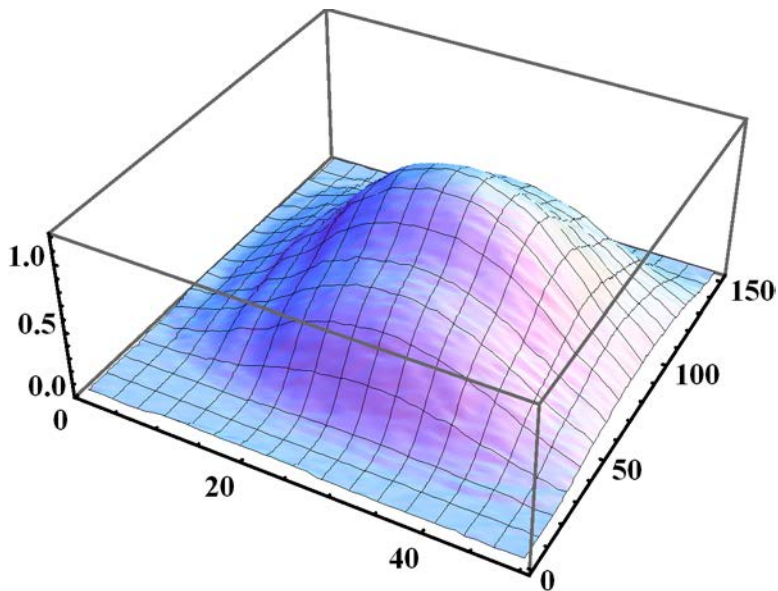
Figure B-30.   3-D Plot of |*Z*| Obtained from Raster Scan of 20-kHz Ferrite Core Probe over Notch #11 in Vertical Direction at 50 kHz

Instrumentation: Nondestructive Examination for Verification of Canister and Cladding Integrity – FY2014 Status Update

B-16   September 12, 2014
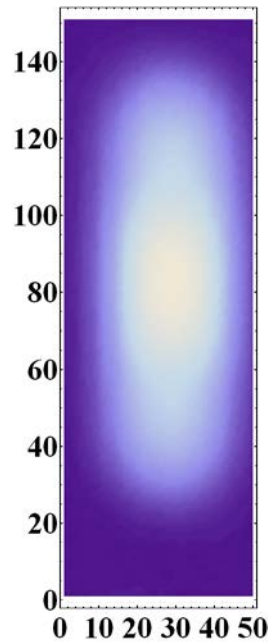
Figure B-31.   Density Plot of |*Z*| Obtained from Raster Scan of 20-kHz Ferrite Core Probe over Notch #11 in Vertical Direction at 60 kHz
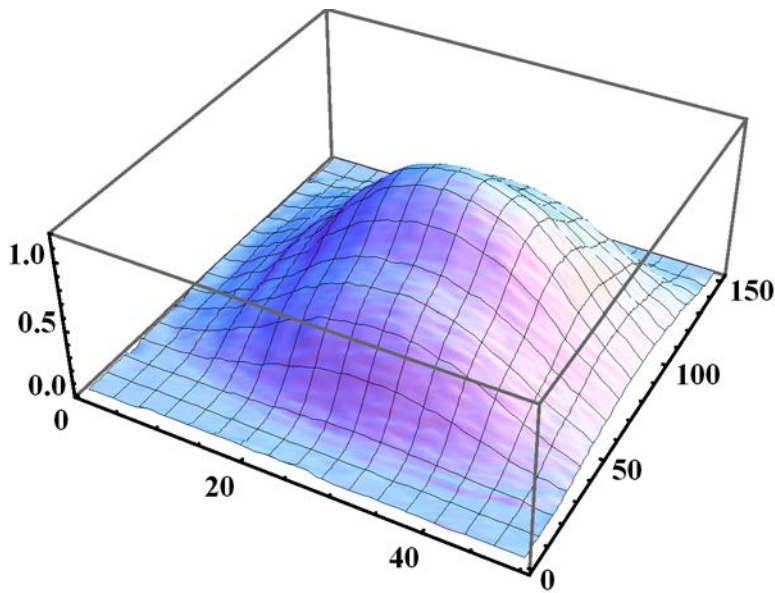
Figure B-32.   3-D Plot of |*Z*| Obtained from Raster Scan of 20-kHz Ferrite Core Probe over Notch #11 in Vertical Direction at 60 kHz
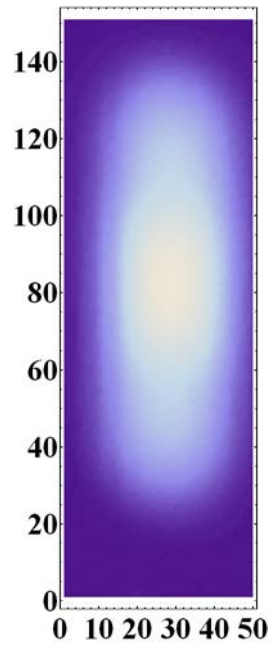
Figure B-33.   Density Plot of |Z| Obtained from Raster Scan of 20-kHz Ferrite Core Probe over Notch #11 in Vertical Direction at 70 kHz
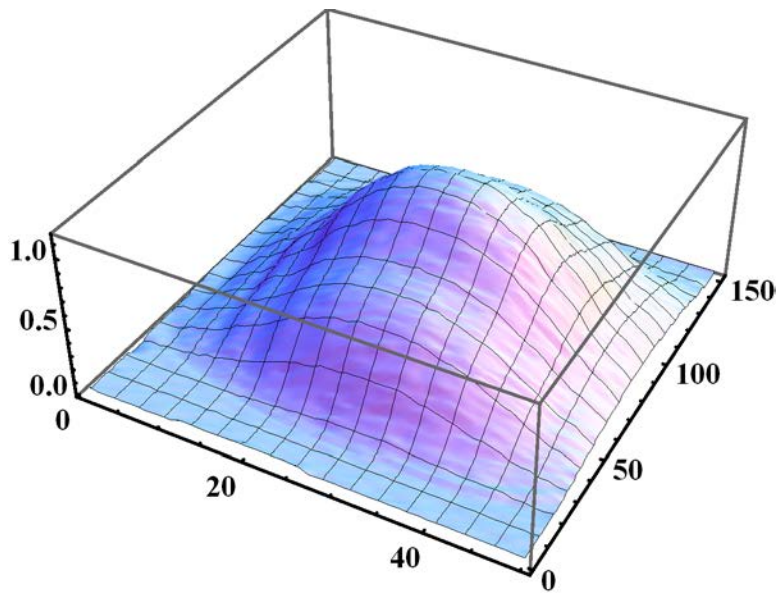

Figure B-34.   3-D Plot of |Z| Obtained from Raster Scan of 20-kHz Ferrite Core Probe over Notch #11 in Vertical Direction at 70 kHz
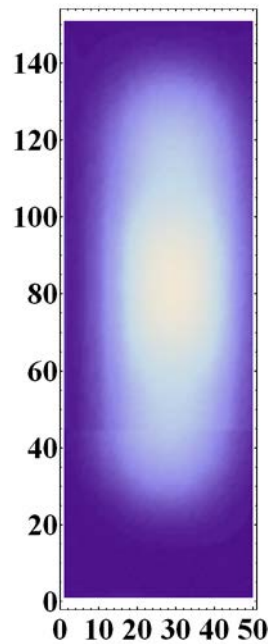
Figure B-35. Density Plot of |*Z*| Obtained from Raster Scan of 20-kHz Ferrite Core Probe over
Notch #11 in Vertical Direction at 80 kHz
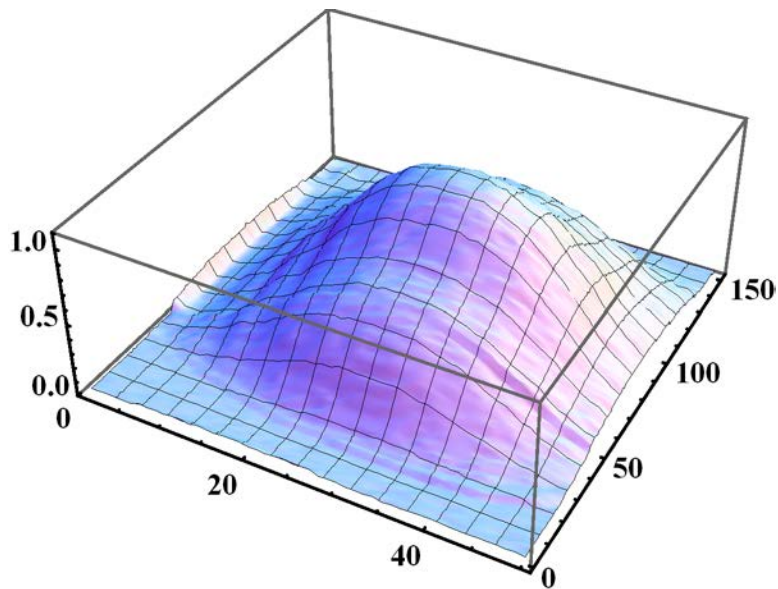
Figure B-36. 3-D Plot of |*Z*| Obtained from Raster Scan of 20-kHz Ferrite Core Probe over
Notch #11 in Vertical Direction at 80 kHz
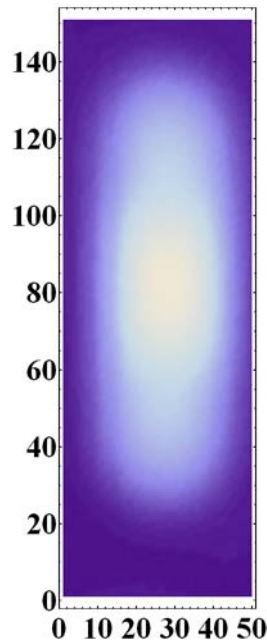
Figure B-37.   Density Plot of |Z| Obtained from Raster Scan of 20-kHz Ferrite Core Probe over Notch #11 in Vertical Direction at 90 kHz
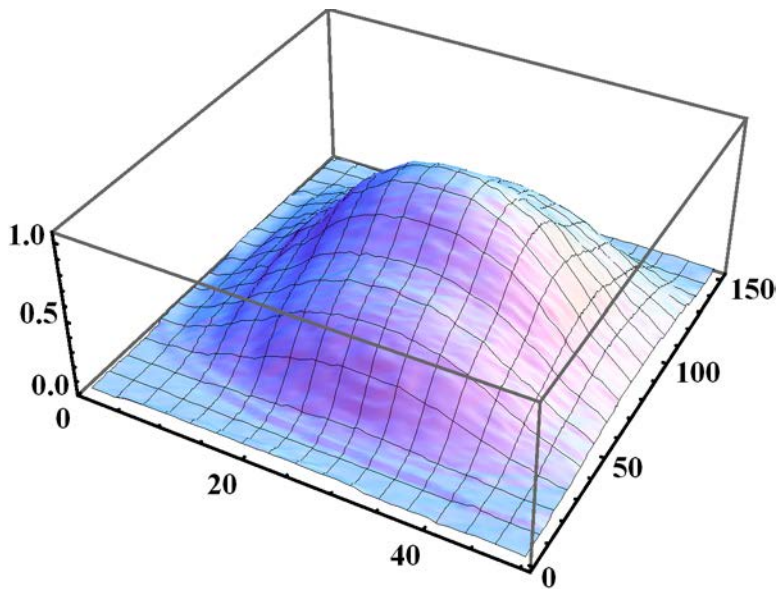
Figure B-38.   3-D Plot of |Z| Obtained from Raster Scan of 20-kHz Ferrite Core Probe over Notch #11 in Vertical Direction at 90 kHz
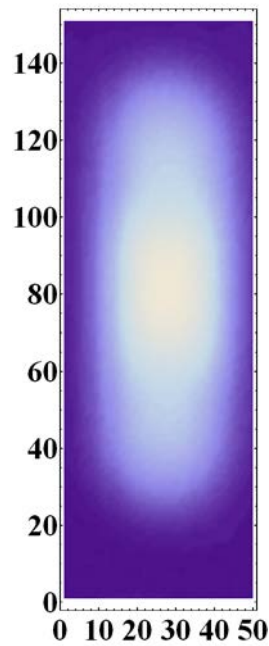
Figure B-39.   Density Plot of |Z| Obtained from Raster Scan of 20-kHz Ferrite Core Probe over
   Notch #11 in Vertical Direction at 100 kHz
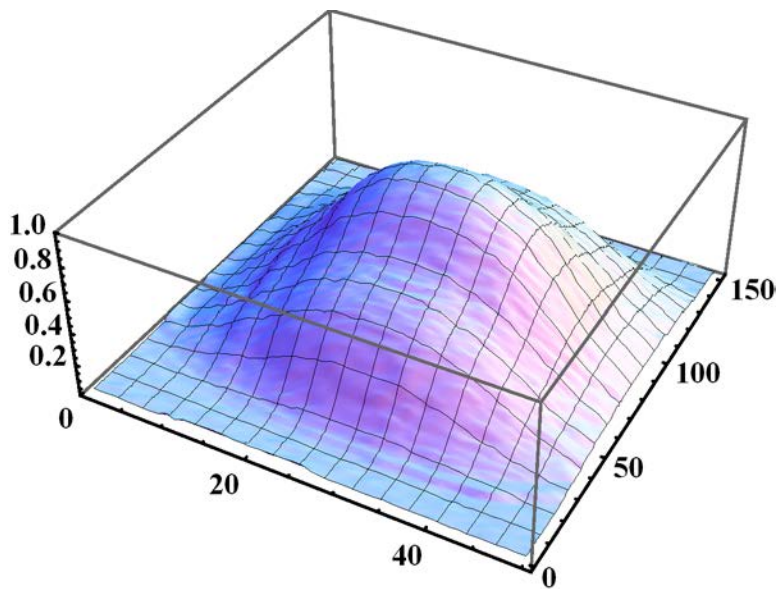
Figure B-40.   3-D Plot of |Z| Obtained from Raster Scan of 20-kHz Ferrite Core Probe over
   Notch #11 in Vertical Direction at 100 kHz

B.3   Data for EDM Notch #1
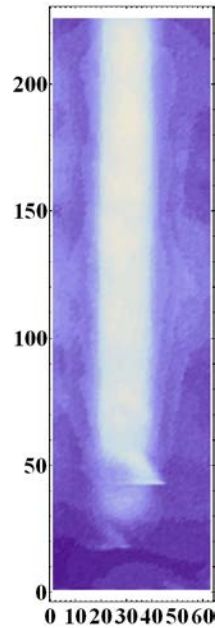
Figure B-41.   Density Plot of |Z| Obtained from Raster Scan of 20-kHz Ferrite Core Probe over Notch #1 in Vertical Direction at 10 kHz
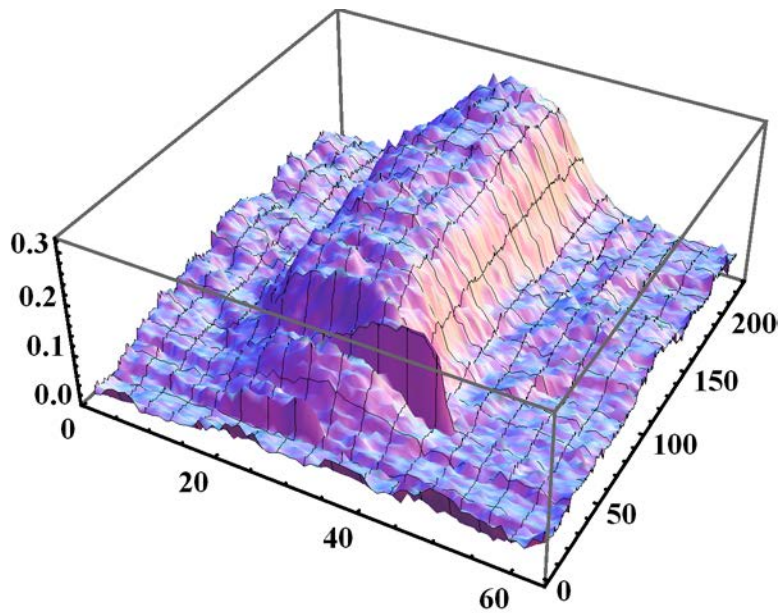

Figure B-42.   3-D Plot of |Z| Obtained from Raster Scan of 20-kHz Ferrite Core Probe over Notch #1 in Vertical Direction at 10 kHz

Instrumentation: Nondestructive Examination for Verification of Canister and Cladding Integrity –
FY2014 Status Update

B-22   September 12, 2014
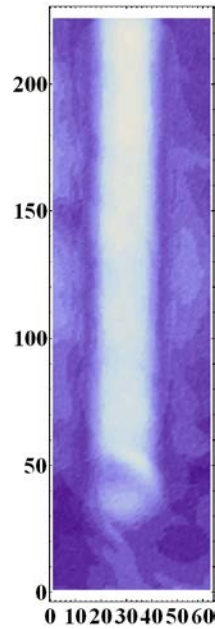
Figure B-43. Density Plot of |*Z*| Obtained from Raster Scan of 20-kHz Ferrite Core Probe over Notch #1 in Vertical Direction at 20 kHz
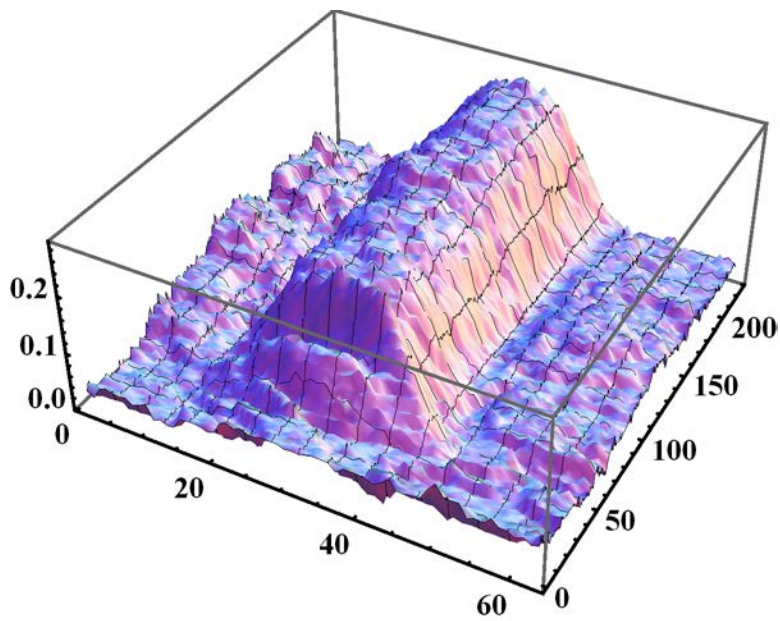
Figure B-44. 3-D Plot of |*Z*| Obtained from Raster Scan of 20-kHz Ferrite Core Probe over Notch #1 in Vertical Direction at 20 kHz

Instrumentation: Nondestructive Examination for Verification of Canister and Cladding Integrity – FY2014 Status Update

September 12, 2014   B-23
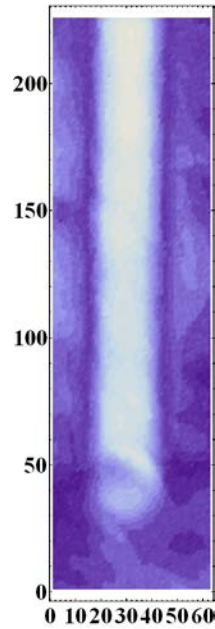
Figure B-45.   Density Plot of |*Z*| Obtained from Raster Scan of 20-kHz Ferrite Core Probe over Notch #1 in Vertical Direction at 30 kHz
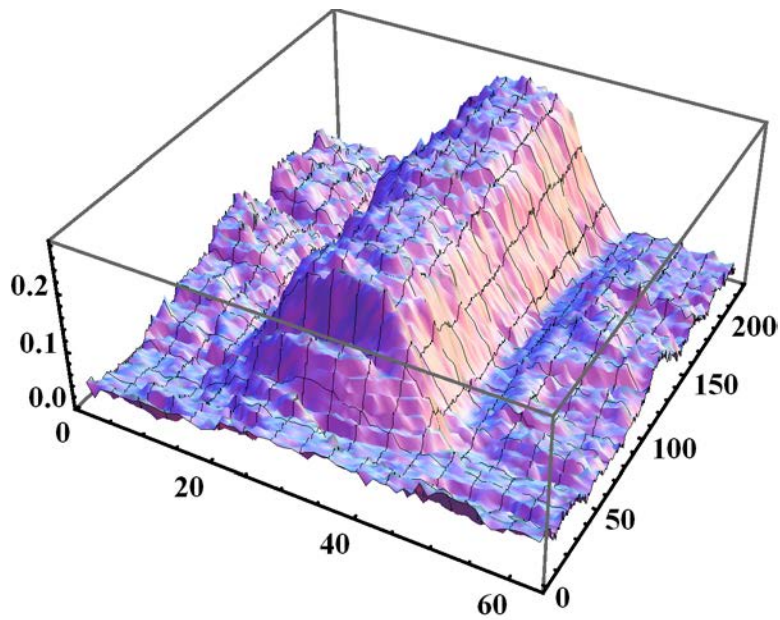
Figure B-46.   3-D Plot of |*Z*| Obtained from Raster Scan of 20-kHz Ferrite Core Probe over Notch #1 in Vertical Direction at 30 kHz
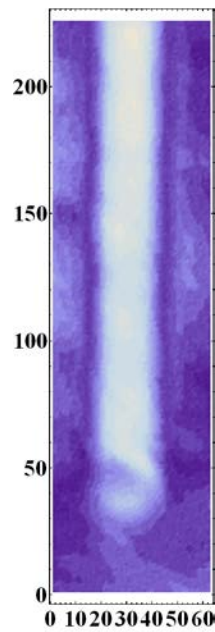
Figure B-47.   Density Plot of |Z| Obtained from Raster Scan of 20-kHz Ferrite Core Probe over
Notch #1 in Vertical Direction at 40 kHz
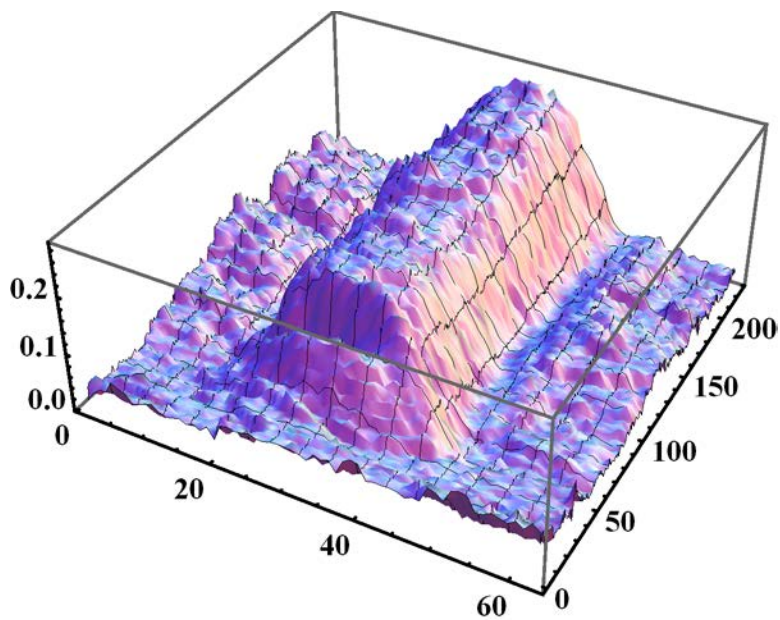
Figure B-48.   3-D Plot of |Z| Obtained from Raster Scan of 20-kHz Ferrite Core Probe over
Notch #1 in Vertical Direction at 40 kHz
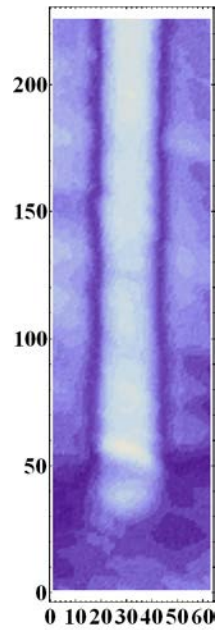
Figure B-49.   Density Plot of |Z| Obtained from Raster Scan of 20-kHz Ferrite Core Probe over
Notch #1 in Vertical Direction at 50 kHz
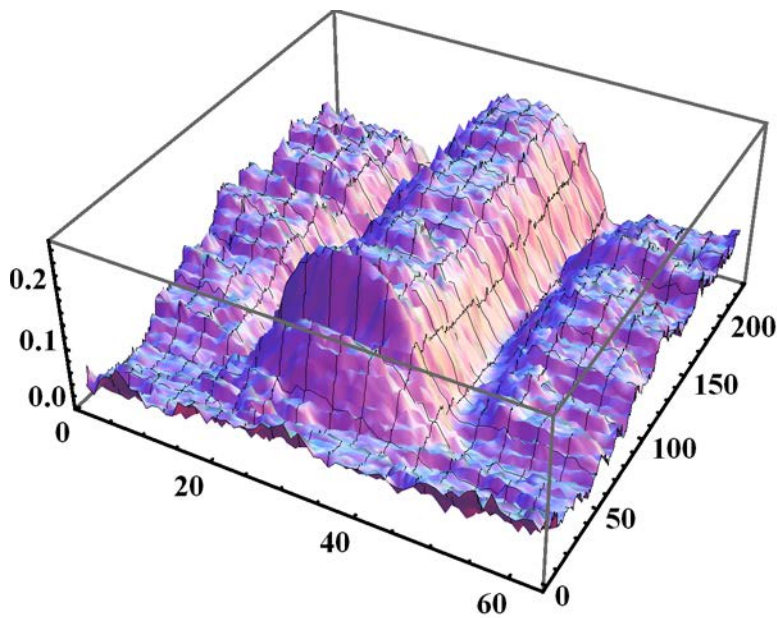
Figure B-50.   3-D Plot of |Z| Obtained from Raster Scan of 20-kHz Ferrite Core Probe over
Notch #1 in Vertical Direction at 50 kHz
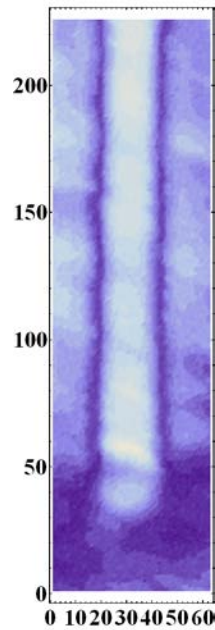
Figure B-51.   Density Plot of |*Z*| Obtained from Raster Scan of 20-kHz Ferrite Core Probe over
Notch #1 in Vertical Direction at 60 kHz
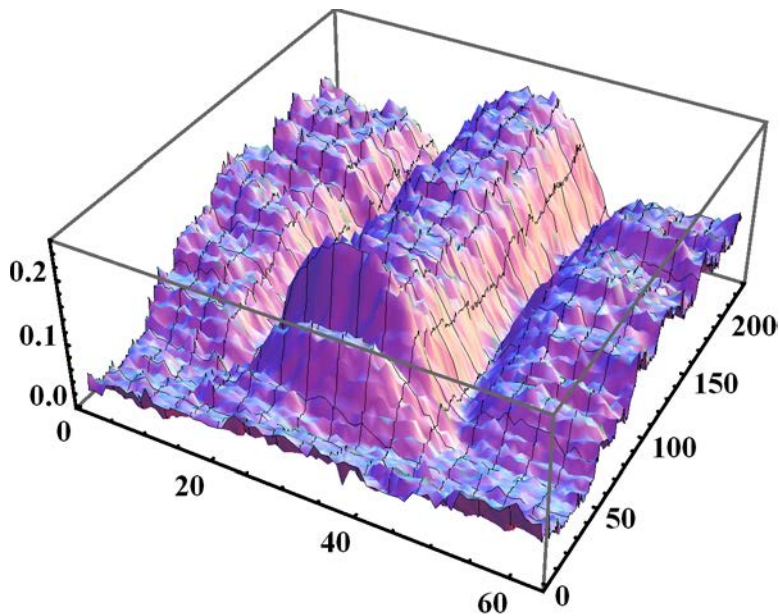
Figure B-52.   3-D Plot of |*Z*| Obtained from Raster Scan of 20-kHz Ferrite Core Probe over
Notch #1 in Vertical Direction at 60 kHz
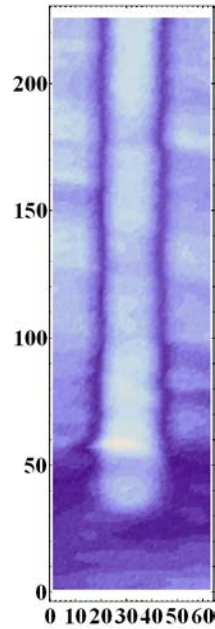
Figure B-53.   Density Plot of |*Z*| Obtained from Raster Scan of 20-kHz Ferrite Core Probe over
               Notch #1 in Vertical Direction at 70 kHz
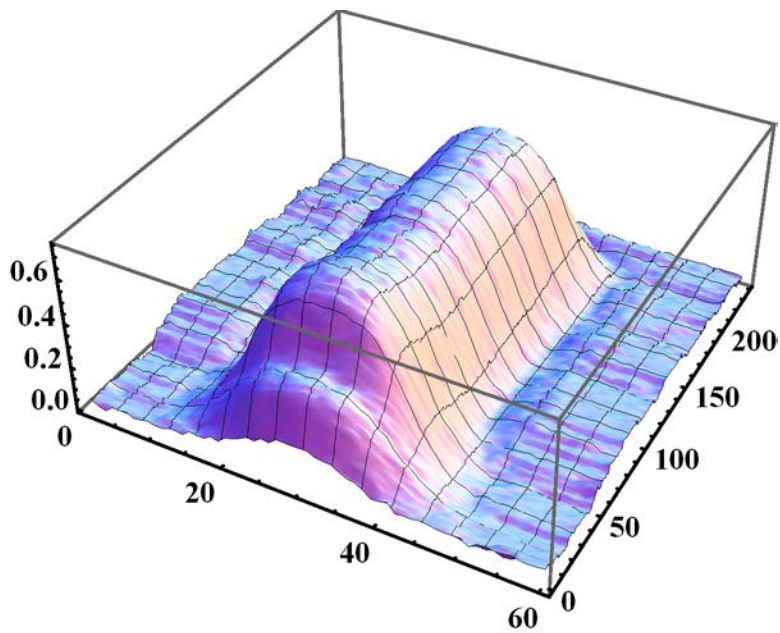
Figure B-54.   3-D Plot of |*Z*| Obtained from Raster Scan of 20-kHz Ferrite Core Probe over
   Notch #1 in Vertical Direction at 70 kHz
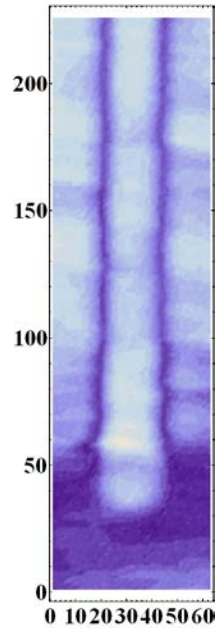
Figure B-55.   Density Plot of |Z| Obtained from Raster Scan of 20-kHz Ferrite Core Probe over
Notch #1 in Vertical Direction at 80 kHz
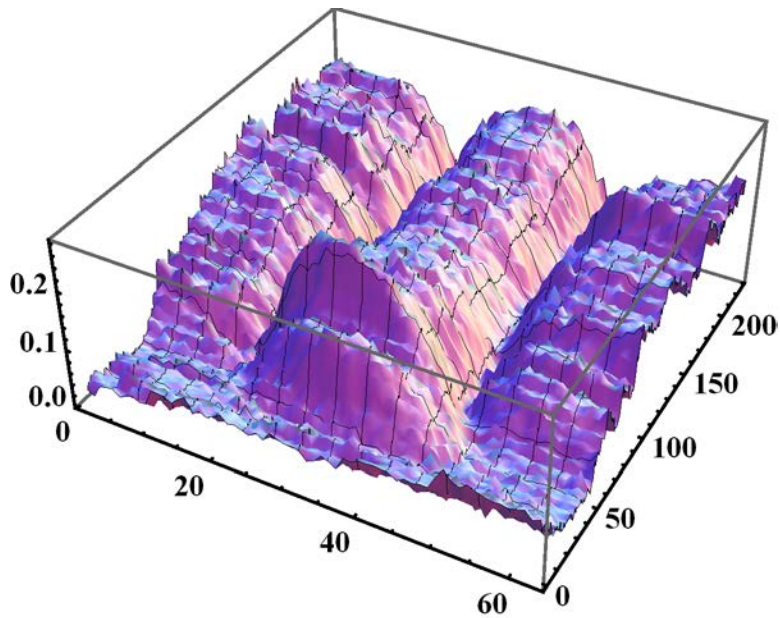

Figure B-56.   3-D Plot of |Z| Obtained from Raster Scan of 20-kHz Ferrite Core Probe over
Notch #1 in Vertical Direction at 80 kHz
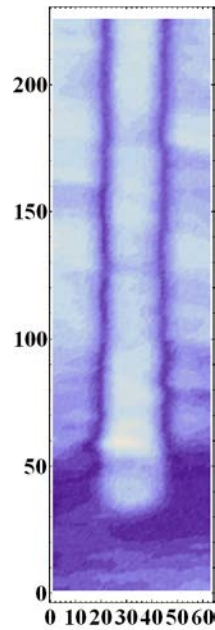
Figure B-57.   Density Plot of |Z| Obtained from Raster Scan of 20-kHz Ferrite Core Probe over Notch #1 in Vertical Direction at 90 kHz
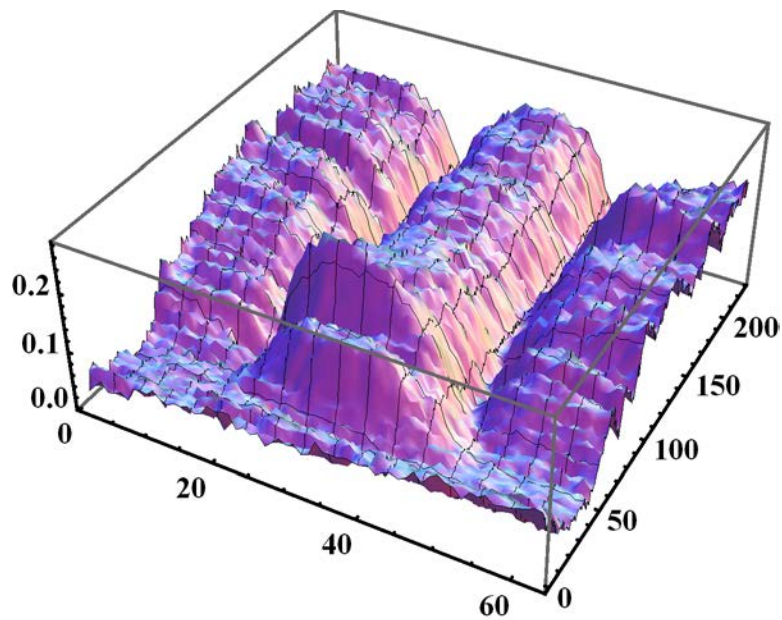

Figure B-58.   3-D Plot of |Z| Obtained from Raster Scan of 20-kHz Ferrite Core Probe over Notch #1 in Vertical Direction at 90 kHz
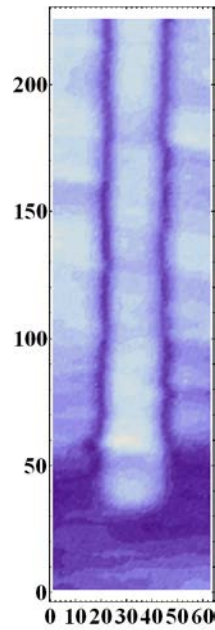
Figure B-59.   Density Plot of |Z| Obtained from Raster Scan of 20-kHz Ferrite Core Probe over
   Notch #1 in Vertical Direction at 100 kHz
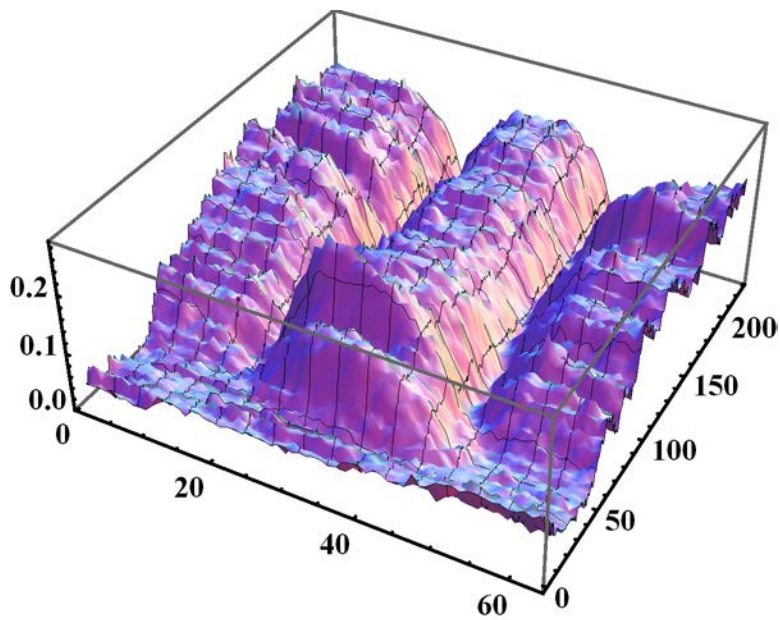
Figure B-60.   3-D Plot of |Z| Obtained from Raster Scan of 20-kHz Ferrite Core Probe over
   Notch #1 in Vertical Direction at 100 kHz

B.4 Data for EDM Notch #2
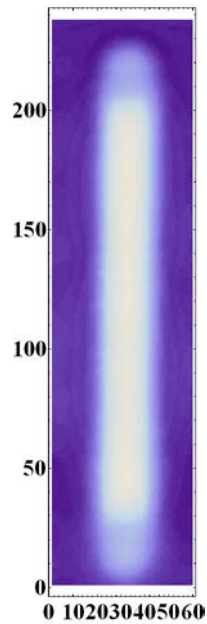
Figure B-61.   Density Plot of |Z| Obtained from Raster Scan of 20-kHz Ferrite Core Probe over
Notch #2 in Vertical Direction at 10 kHz
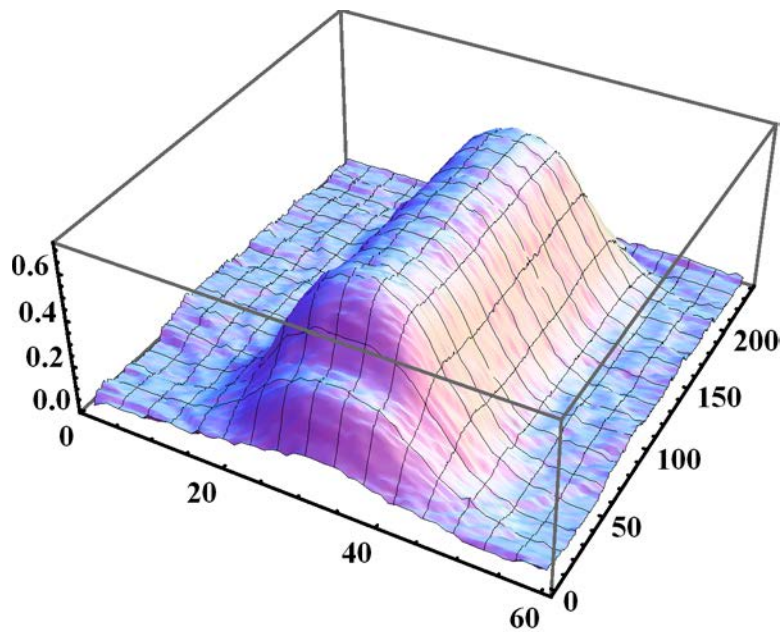
Figure B-62.   3-D Plot of |Z| Obtained from Raster Scan of 20-kHz Ferrite Core Probe over
Notch #2 in Vertical Direction at 10 kHz

Instrumentation: Nondestructive Examination for Verification of Canister and Cladding Integrity – FY2014 Status Update

B-32   September 12, 2014
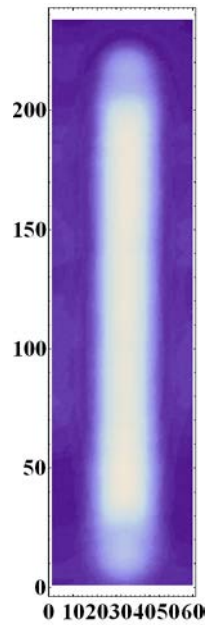
Figure B-63.   Density Plot of |Z| Obtained from Raster Scan of 20-kHz Ferrite Core Probe over Notch #2 in Vertical Direction at 20 kHz
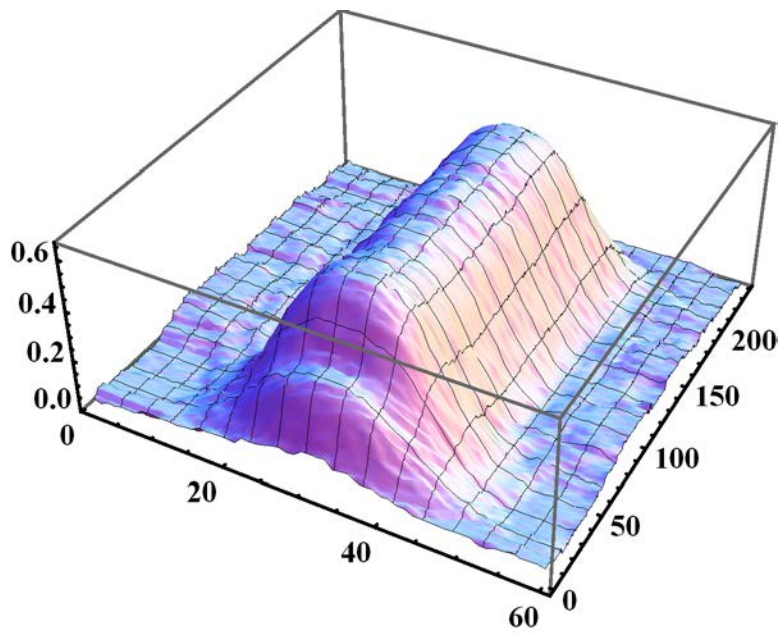

Figure B-64.   3-D Plot of |Z| Obtained from Raster Scan of 20-kHz Ferrite Core Probe over Notch #2 in Vertical Direction at 20 kHz
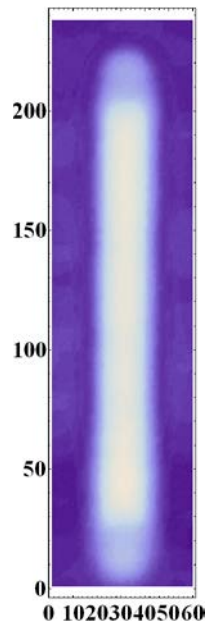
Figure B-65.   Density Plot of |Z| Obtained from Raster Scan of 20-kHz Ferrite Core Probe over Notch #2 in Vertical Direction at 30 kHz
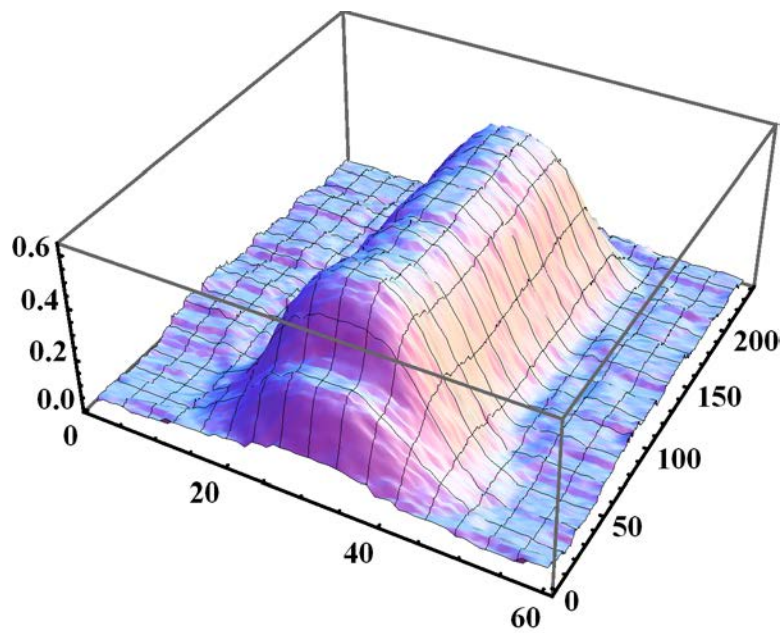
Figure B-66.   3-D Plot of |Z| Obtained from Raster Scan of 20-kHz Ferrite Core Probe over Notch #2 in Vertical Direction at 30 kHz

**Instrumentation: Nondestructive Examination for Verification of Canister and Cladding Integrity –
FY2014 Status Update**

B-34   September 12, 2014
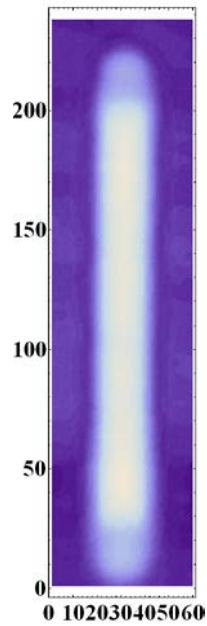
Figure B-67.   Density Plot of |Z| Obtained from Raster Scan of 20-kHz Ferrite Core Probe over
Notch #2 in Vertical Direction at 40 kHz
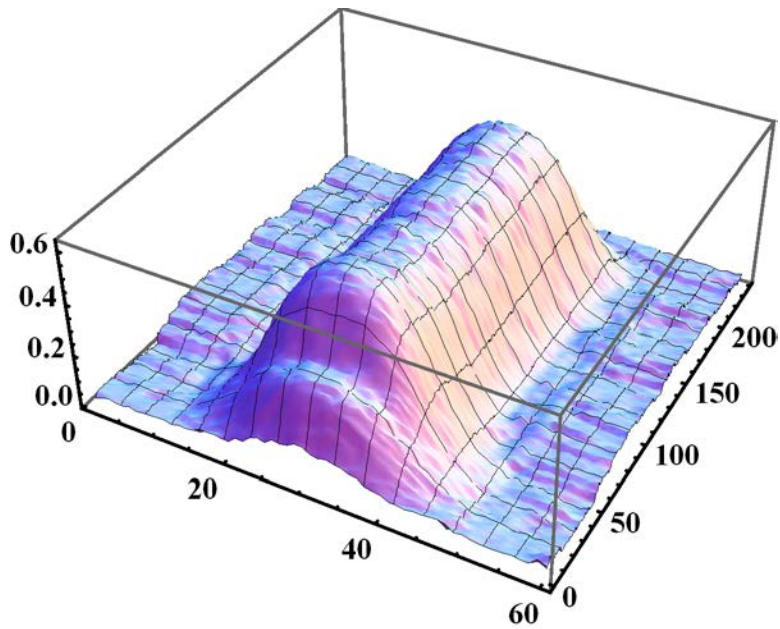
Figure B-68.   3-D Plot of |Z| Obtained from Raster Scan of 20-kHz Ferrite Core Probe over
Notch #2 in Vertical Direction at 40 kHz

Instrumentation: Nondestructive Examination for Verification of Canister and Cladding Integrity – FY2014 Status Update

September 12, 2014   B-35
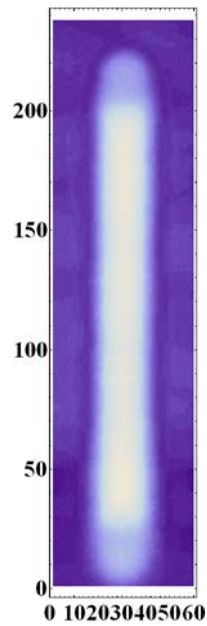
Figure B-69.   Density Plot of |Z| Obtained from Raster Scan of 20-kHz Ferrite Core Probe over Notch #2 in Vertical Direction at 50 kHz
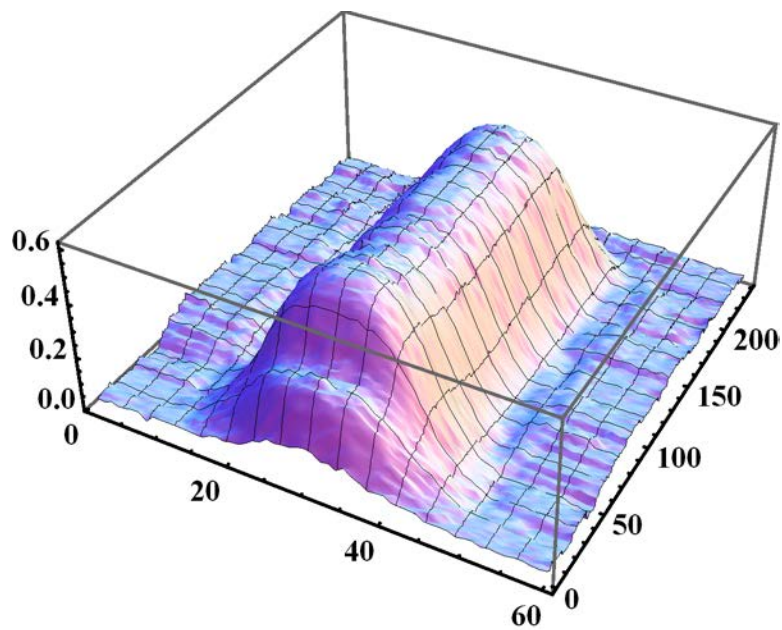
Figure B-70.   3-D Plot of |Z| Obtained from Raster Scan of 20-kHz Ferrite Core Probe over Notch #2 in Vertical Direction at 50 kHz

Instrumentation: Nondestructive Examination for Verification of Canister and Cladding Integrity – FY2014 Status Update

B-36   September 12, 2014
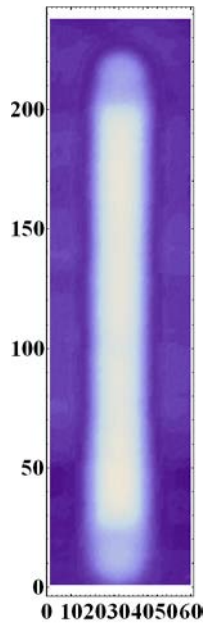
Figure B-71.   Density Plot of |Z| Obtained from Raster Scan of 20-kHz Ferrite Core Probe over Notch #2 in Vertical Direction at 60 kHz
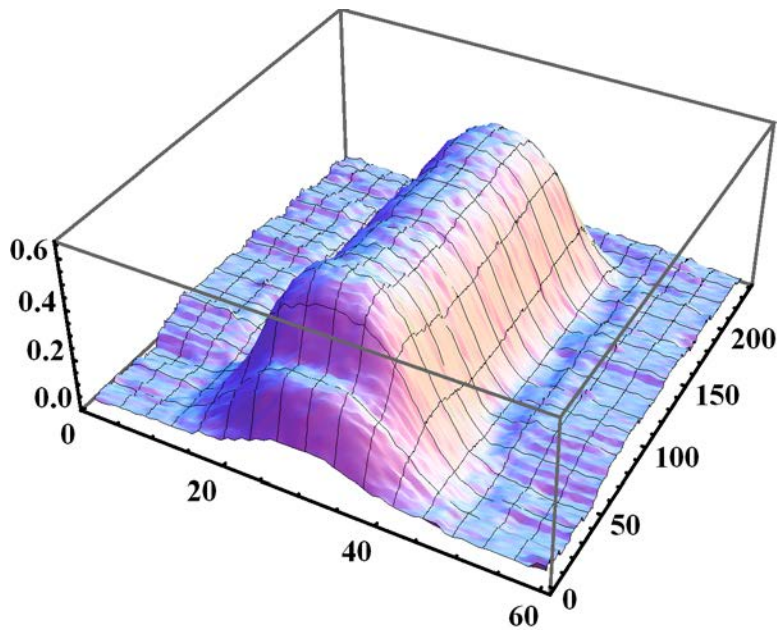
Figure B-72.   3-D Plot of |Z| Obtained from Raster Scan of 20-kHz Ferrite Core Probe over Notch #2 in Vertical Direction at 60 kHz
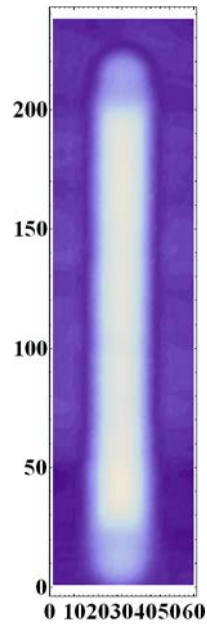
Figure B-73.   Density Plot of |Z| Obtained from Raster Scan of 20-kHz Ferrite Core Probe over
Notch #2 in Vertical Direction at 70 kHz
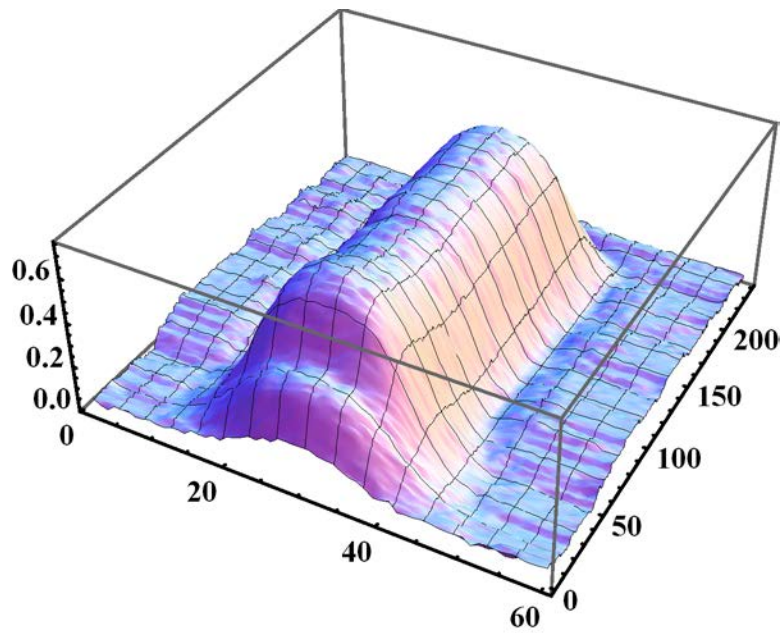
Figure B-74.   3-D Plot of |Z| Obtained from Raster Scan of 20-kHz Ferrite Core Probe over
Notch #2 in Vertical Direction at 70 kHz
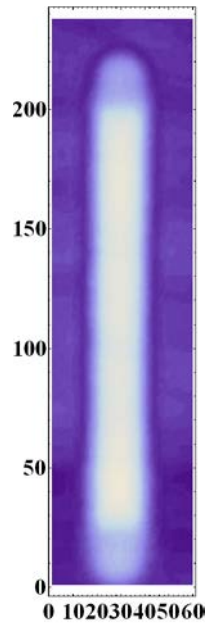
Figure B-75.   Density Plot of |Z| Obtained from Raster Scan of 20-kHz Ferrite Core Probe over Notch #2 in Vertical Direction at 80 kHz
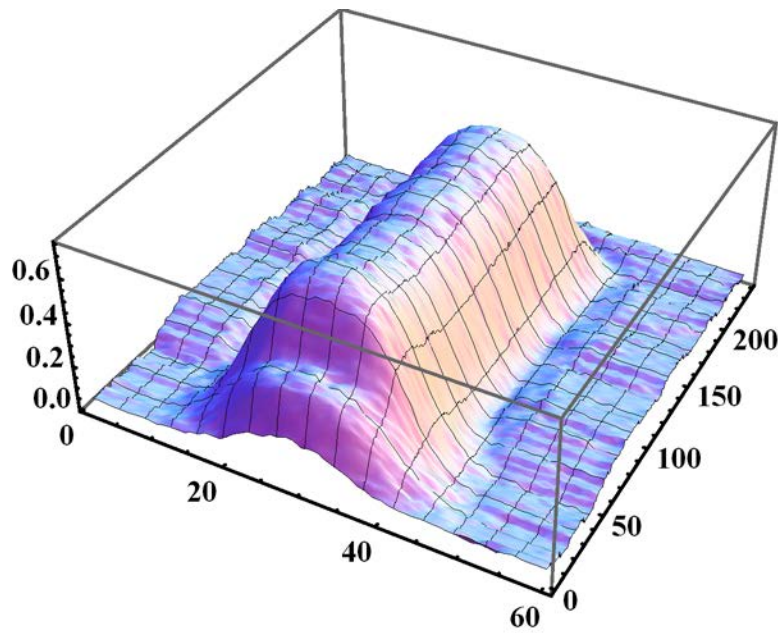

Figure B-76.   3-D Plot of |Z| Obtained from Raster Scan of 20-kHz Ferrite Core Probe over Notch #2 in Vertical Direction at 80 kHz
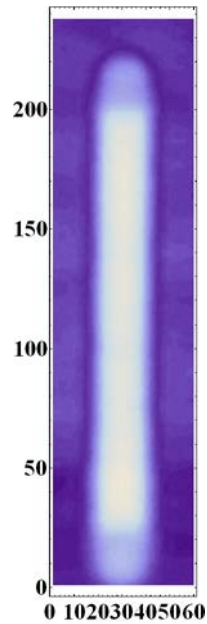
Figure B-77.   Density Plot of |Z| Obtained from Raster Scan of 20-kHz Ferrite Core Probe over Notch #2 in Vertical Direction at 90 kHz
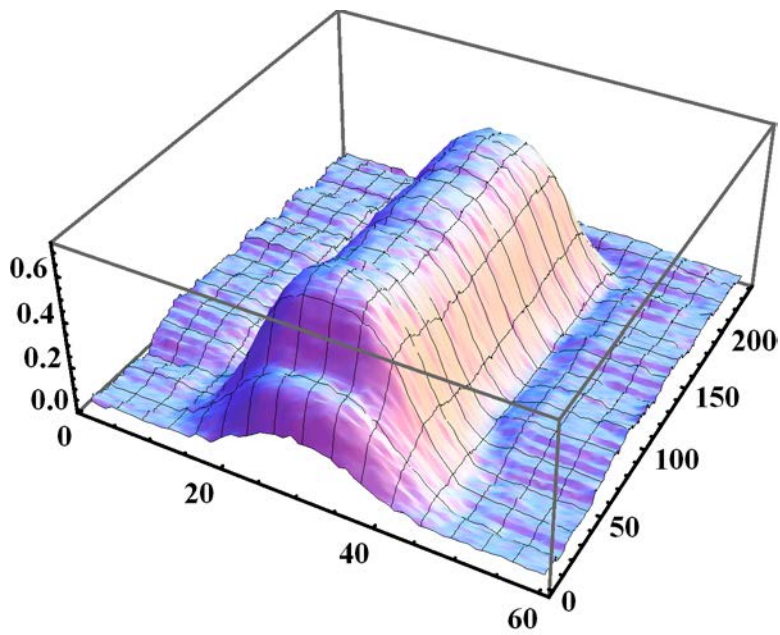

Figure B-78.   3-D Plot of |Z| Obtained from Raster Scan of 20-kHz Ferrite Core Probe over Notch #2 in Vertical Direction at 90 kHz
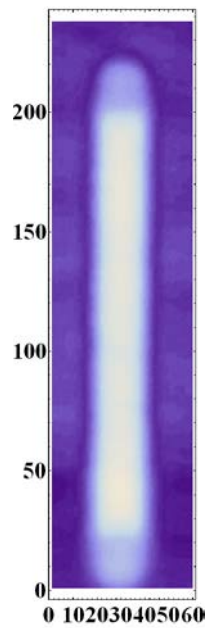
Figure B-79.   Density Plot of |Z| Obtained from Raster Scan of 20-kHz Ferrite Core Probe over
Notch #2 in Vertical Direction at 100 kHz
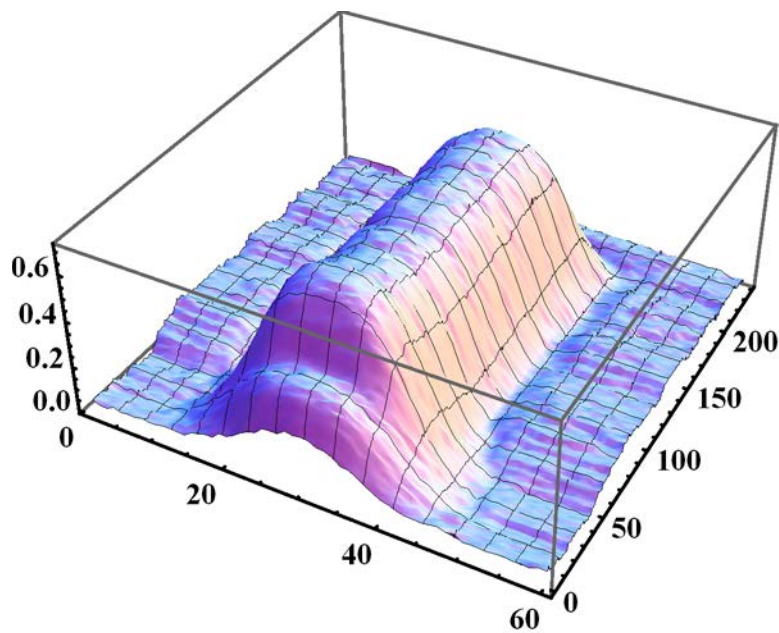
Figure B-80.   3-D Plot of |Z| Obtained from Raster Scan of 20-kHz Ferrite Core Probe over
Notch #2 in Vertical Direction at 100 kHz

B.5 Scan Data for Specimen B117
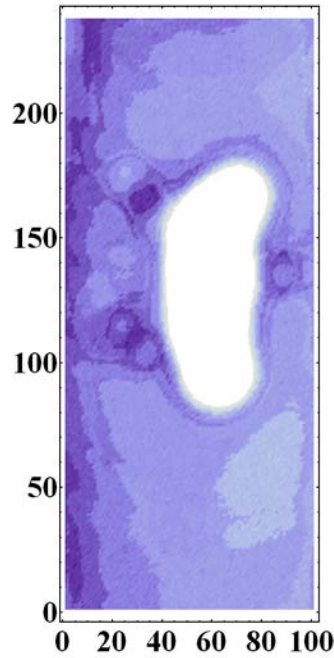
Figure B-81.   Density Plot of |Z| Obtained from Raster Scan of 20-kHz Ferrite Core Probe over
B117 in Vertical Direction at 10 kHz
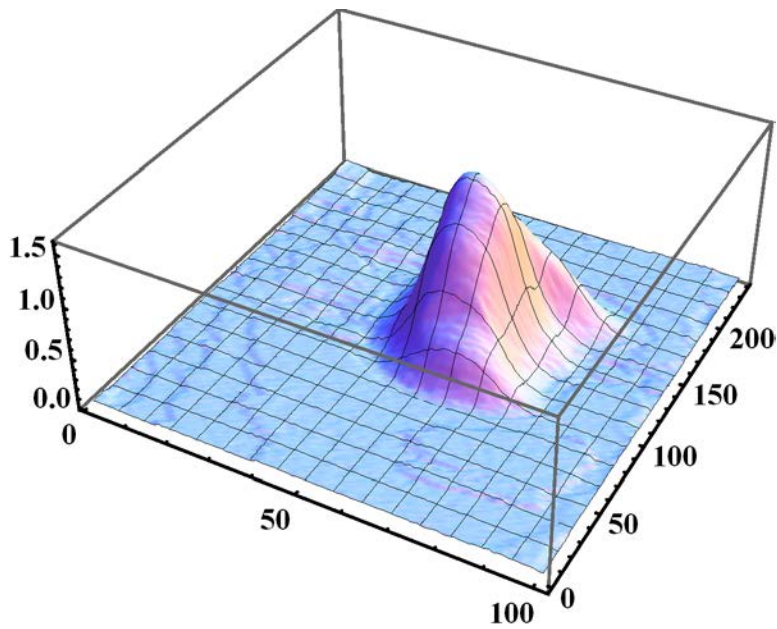
Figure B-82.   3-D Plot of |Z| Obtained from Raster Scan of 20-kHz Ferrite Core Probe over
B117 in Vertical Direction at 10 kHz
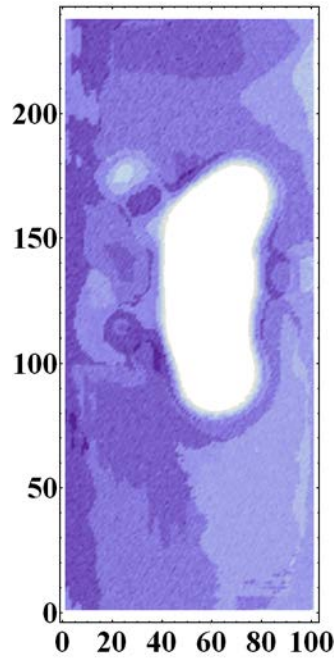
Figure B-83.   Density Plot of |Z| Obtained from Raster Scan of 20-kHz Ferrite Core Probe over
B117 in Vertical Direction at 20 kHz
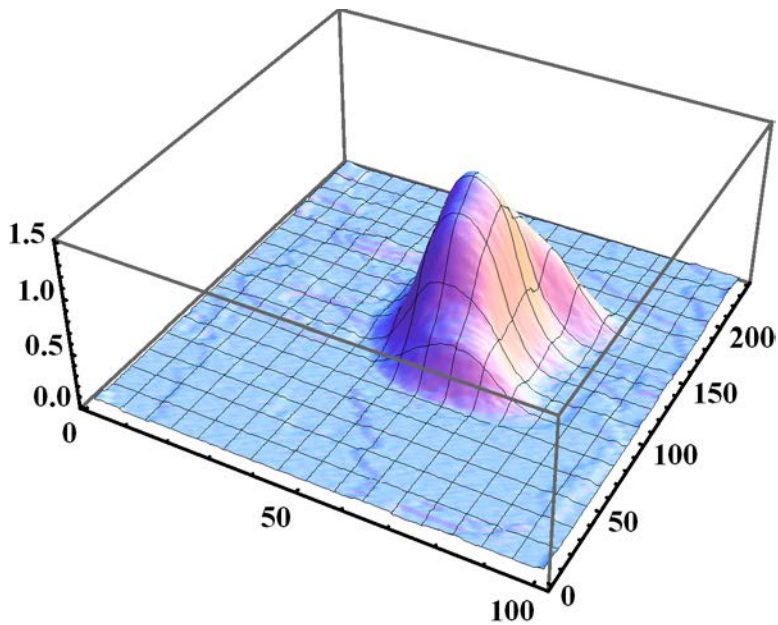
Figure B-84.   3-D Plot of |Z| Obtained from Raster Scan of 20-kHz Ferrite Core Probe over
B117 in Vertical Direction at 20 kHz
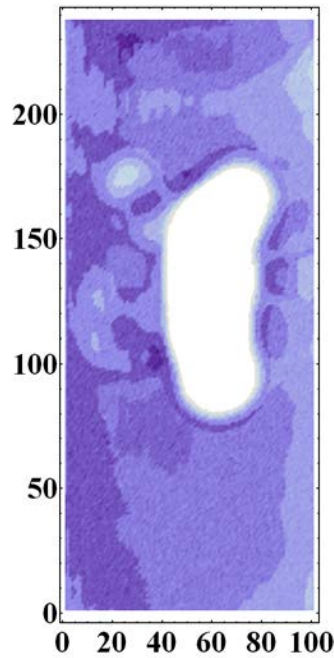
Figure B-85.   Density Plot of |Z| Obtained from Raster Scan of 20-kHz Ferrite Core Probe over B117 in Vertical Direction at 30 kHz
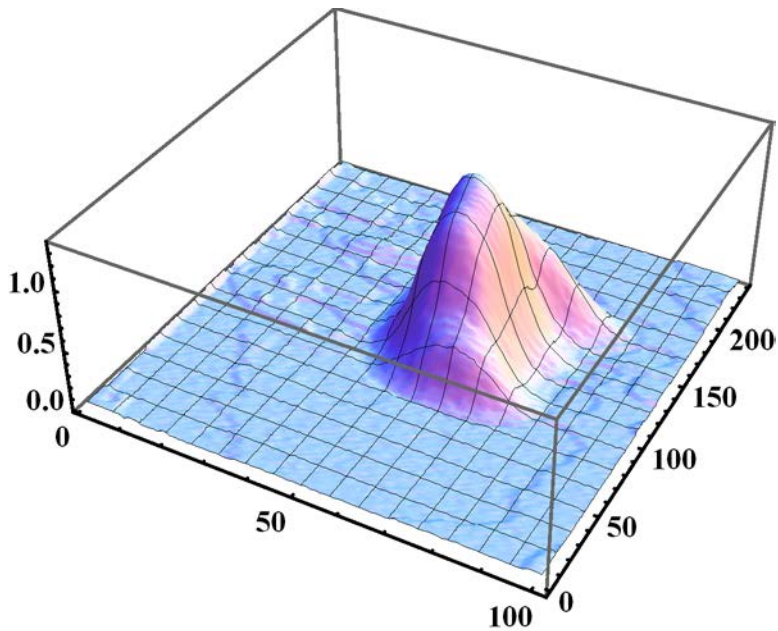
Figure B-86.   3-D Plot of |Z| Obtained from Raster Scan of 20-kHz Ferrite Core Probe over B117 in Vertical Direction at 30 kHz
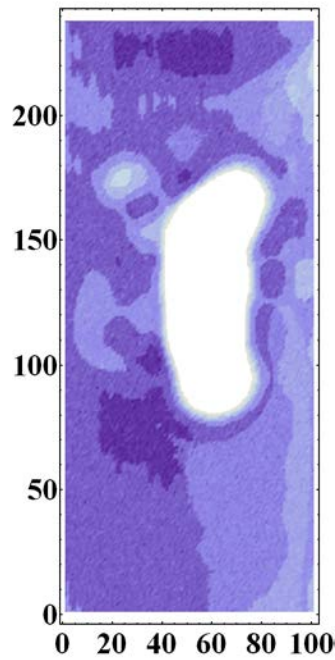
Figure B-87.   Density Plot of |Z| Obtained from Raster Scan of 20-kHz Ferrite Core Probe over
B117 in Vertical Direction at 40 kHz
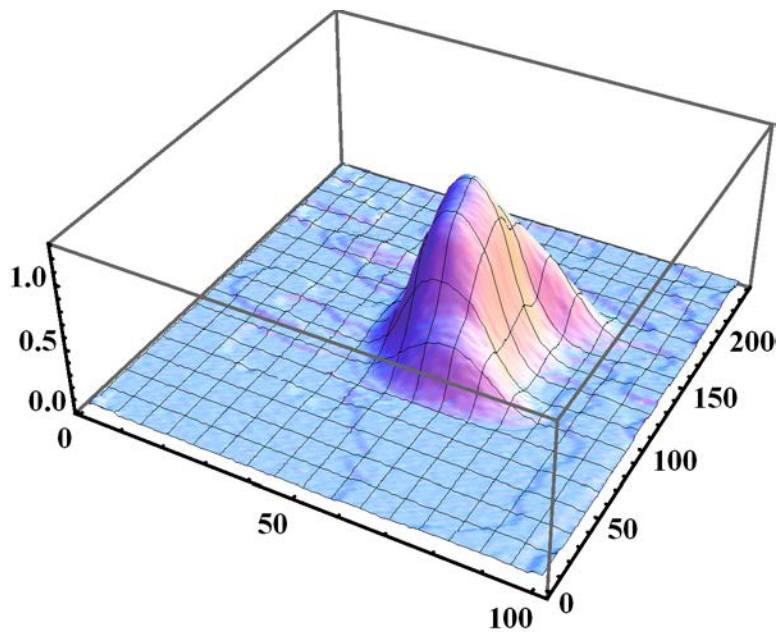
Figure B-88.   3-D Plot of |Z| Obtained from Raster Scan of 20-kHz Ferrite Core Probe over
B117 in Vertical Direction at 40 kHz
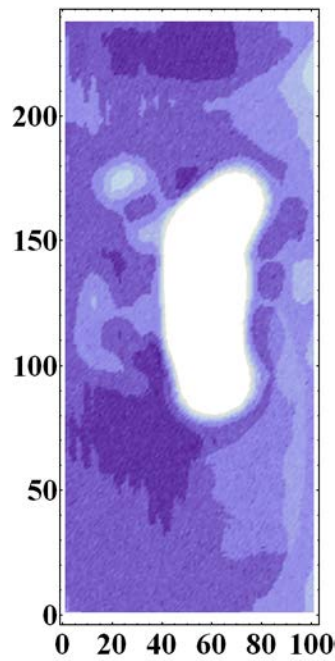
Figure B-89.   Density Plot of |Z| Obtained from Raster Scan of 20-kHz Ferrite Core Probe over
B117 in Vertical Direction at 50 kHz
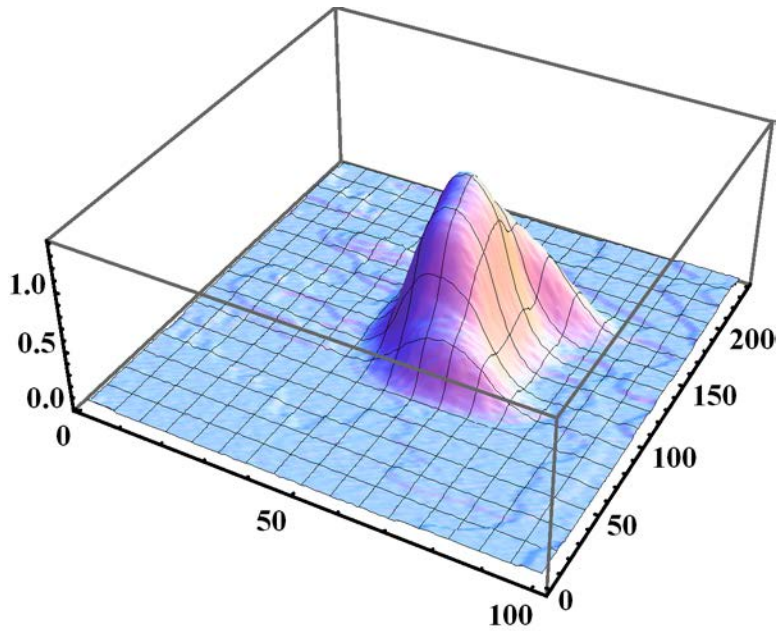
Figure B-90.   3-D Plot of |Z| Obtained from Raster Scan of 20-kHz Ferrite Core Probe over
B117 in Vertical Direction at 50 kHz
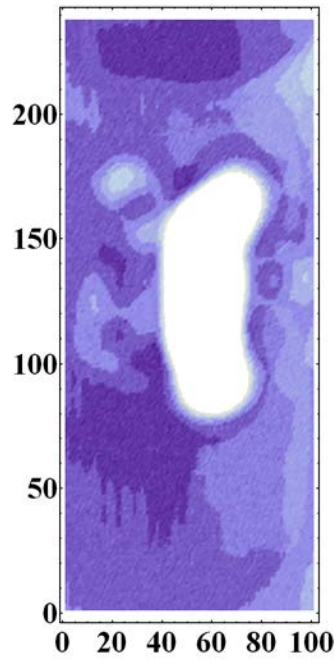
Figure B-91.   Density Plot of |Z| Obtained from Raster Scan of 20-kHz Ferrite Core Probe over
   B117 in Vertical Direction at 60 kHz
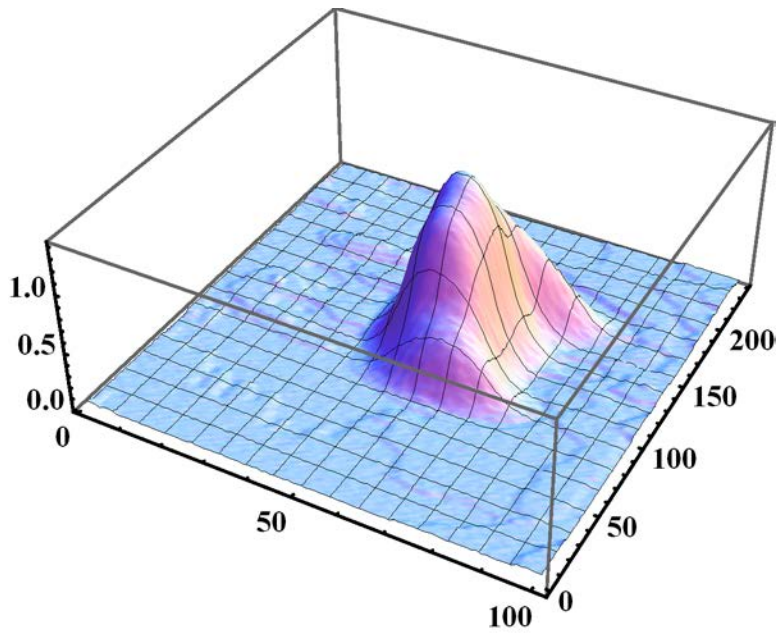
Figure B-92.   3-D Plot of |Z| Obtained from Raster Scan of 20-kHz Ferrite Core Probe over
   B117 in Vertical Direction at 60 kHz
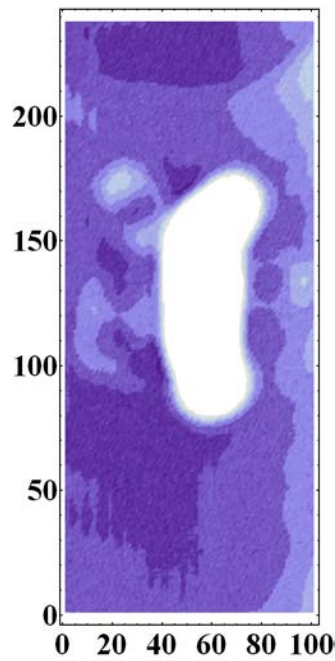
Figure B-93.   Density Plot of |Z| Obtained from Raster Scan of 20-kHz Ferrite Core Probe over B117 in Vertical Direction at 70 kHz
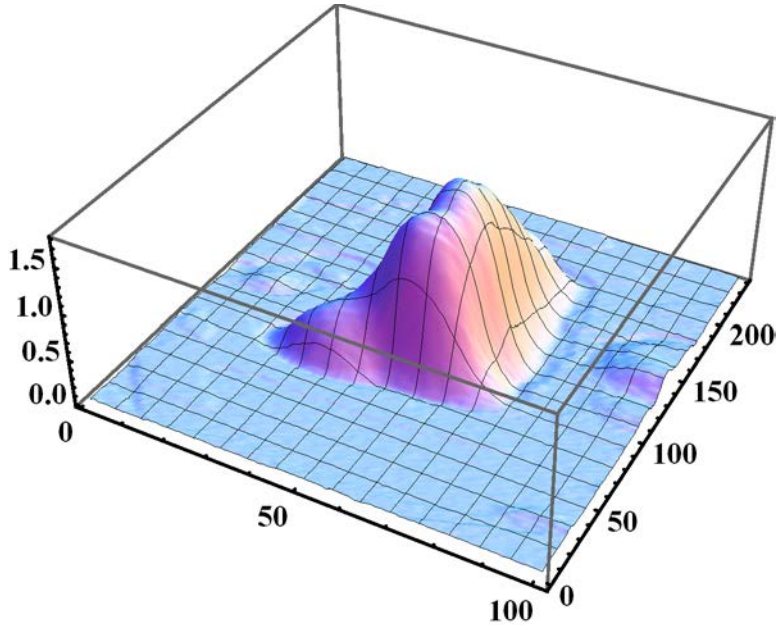

Figure B-94.   3-D Plot of |Z| Obtained from Raster Scan of 20-kHz Ferrite Core Probe over B117 in Vertical Direction at 70 kHz

**Instrumentation: Nondestructive Examination for Verification of Canister and Cladding Integrity –
FY2014 Status Update**

B-48   September 12, 2014
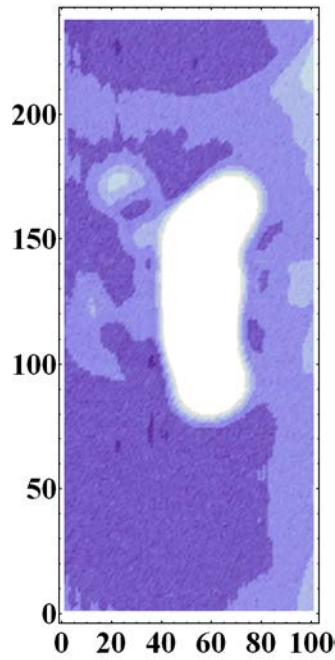
Figure B-95.   Density Plot of |Z| Obtained from Raster Scan of 20-kHz Ferrite Core Probe over
B117 in Vertical Direction at 80 kHz
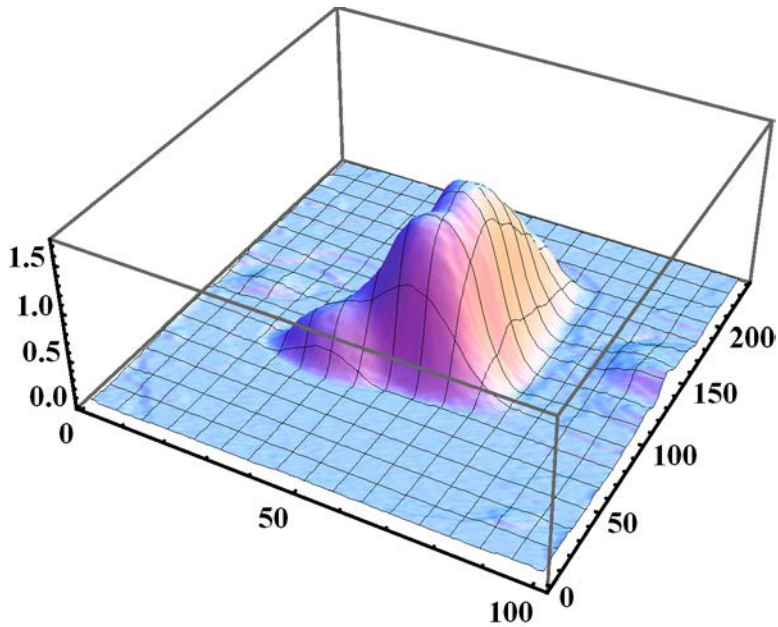
Figure B-96.   3-D Plot of |Z| Obtained from Raster Scan of 20-kHz Ferrite Core Probe over
B117 in Vertical Direction at 80 kHz
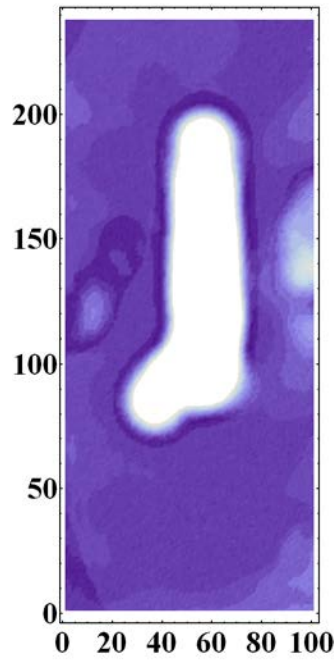
Figure B-97.   Density Plot of |Z| Obtained from Raster Scan of 20-kHz Ferrite Core Probe over B117 in Vertical Direction at 90 kHz
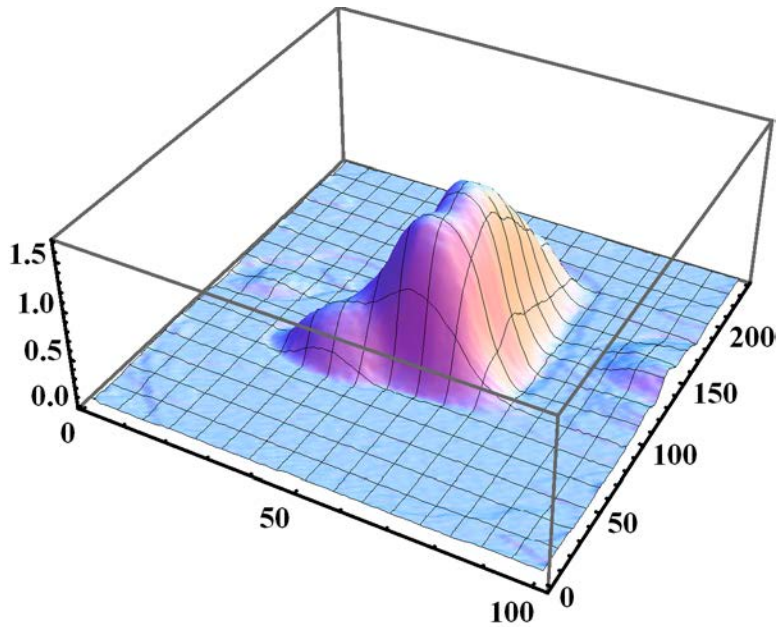

Figure B-98.   3-D Plot of |Z| Obtained from Raster Scan of 20-kHz Ferrite Core Probe over B117 in Vertical Direction at 90 kHz
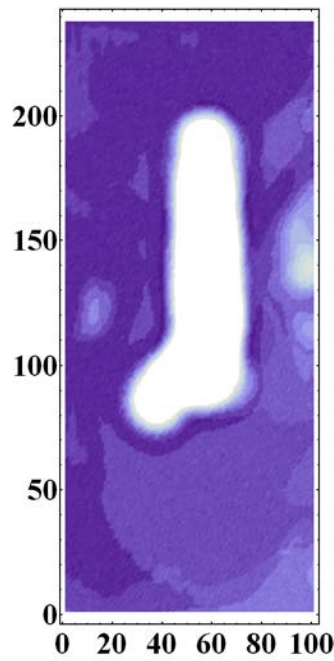
Figure B-99.   Density Plot of |Z| Obtained from Raster Scan of 20-kHz Ferrite Core Probe over
B117 in Vertical Direction at 100 kHz
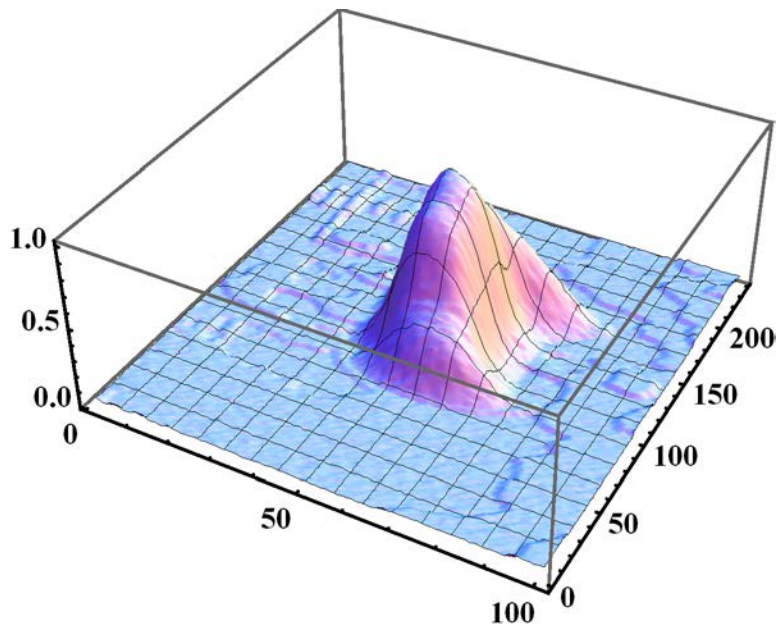
Figure B-100. 3-D Plot of |Z| Obtained from Raster Scan of 20-kHz Ferrite Core Probe over
B117 in Vertical Direction at 100 kHz

B.6 Scan Data for Specimen B118
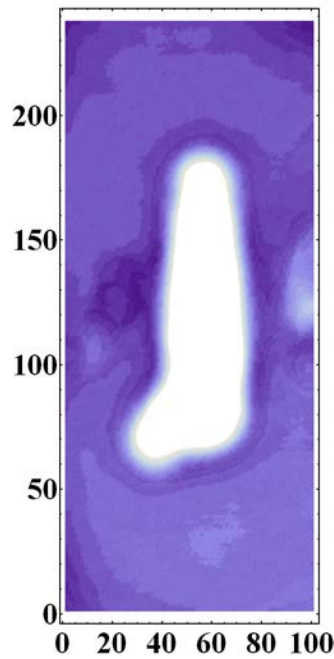
Figure B-101. Density Plot of |Z| Obtained from Raster Scan of 20-kHz Ferrite Core Probe over B118 in Vertical Direction at 10 kHz
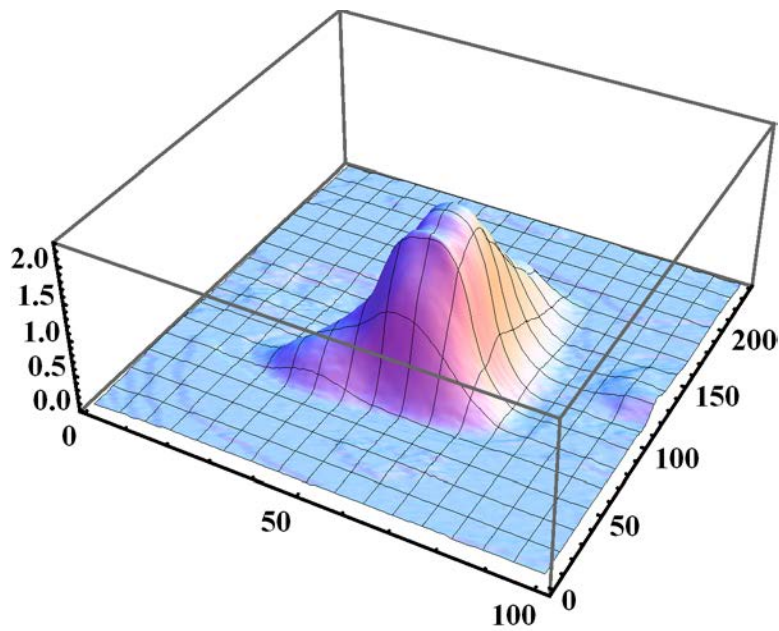
Figure B-102. 3-D Plot of |Z| Obtained from Raster Scan of 20-kHz Ferrite Core Probe over B118 in Vertical Direction at 10 kHz

Instrumentation: Nondestructive Examination for Verification of Canister and Cladding Integrity – FY2014 Status Update

B-52   September 12, 2014
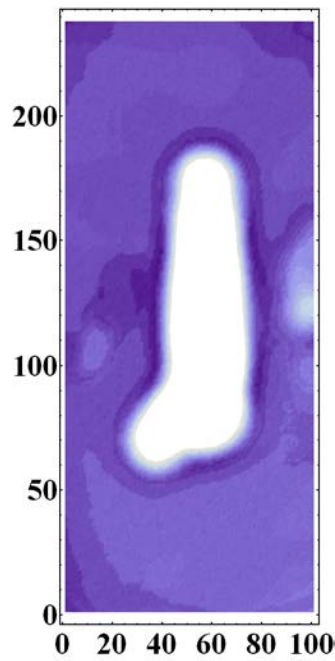
Figure B-103. Density Plot of |Z| Obtained from Raster Scan of 20-kHz Ferrite Core Probe over B118 in Vertical Direction at 20 kHz
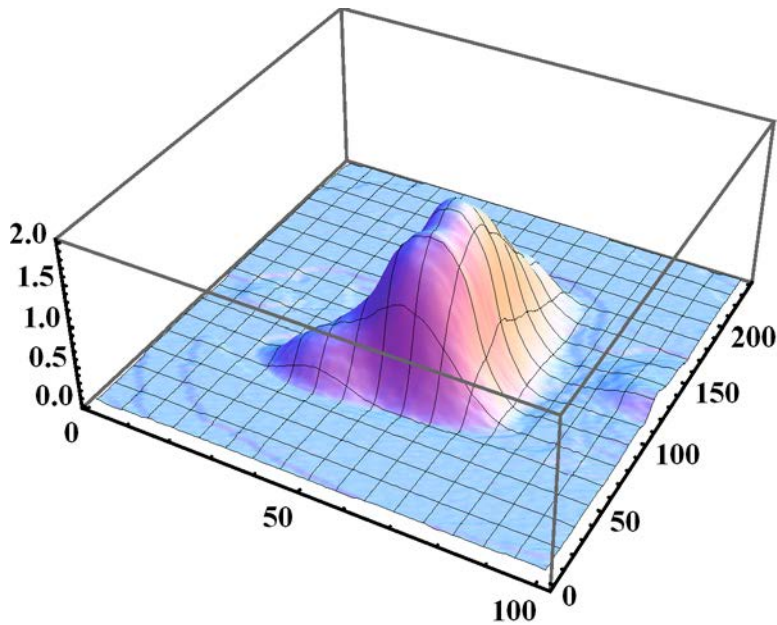
Figure B-104. 3-D Plot of |Z| Obtained from Raster Scan of 20-kHz Ferrite Core Probe over B118 in Vertical Direction at 20 kHz
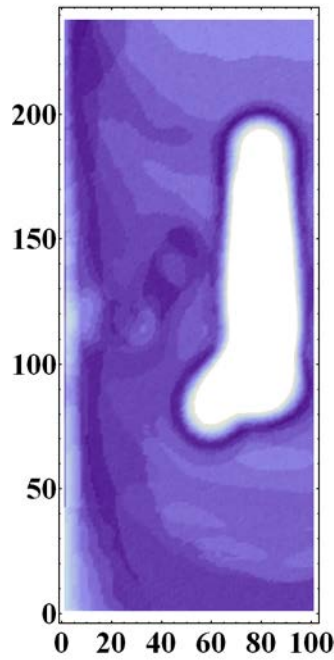
Figure B-105. Density Plot of |Z| Obtained from Raster Scan of 20-kHz Ferrite Core Probe over B118 in Vertical Direction at 30 kHz
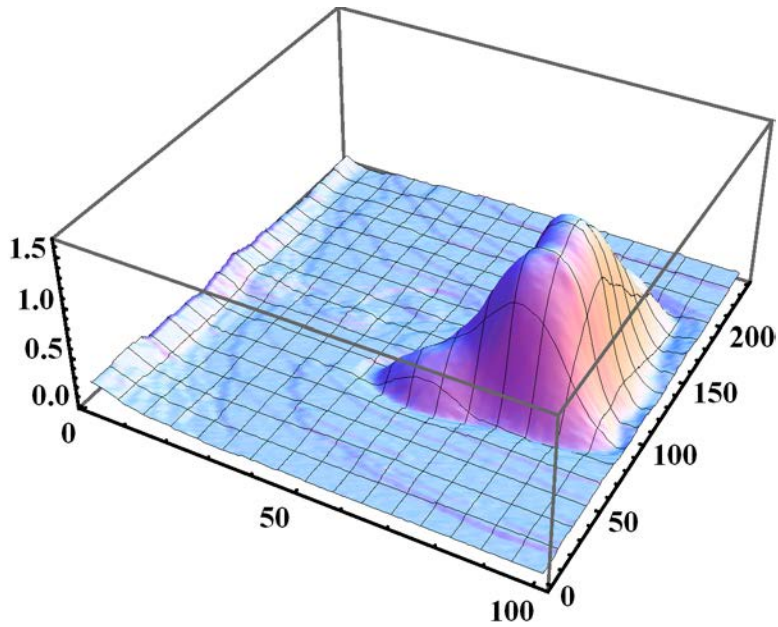

Figure B-106. 3-D Plot of |Z| Obtained from Raster Scan of 20-kHz Ferrite Core Probe over B118 in Vertical Direction at 30 kHz
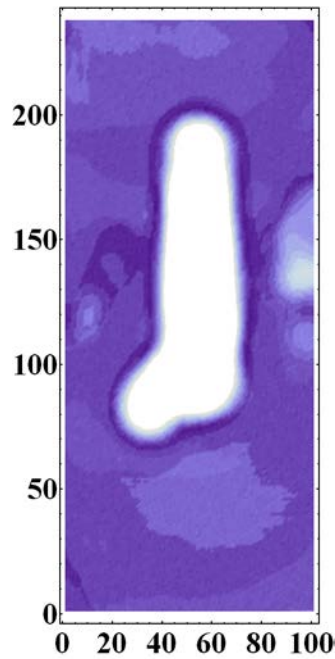
Figure B-107. Density Plot of |Z| Obtained from Raster Scan of 20-kHz Ferrite Core Probe over B118 in Vertical Direction at 40 kHz
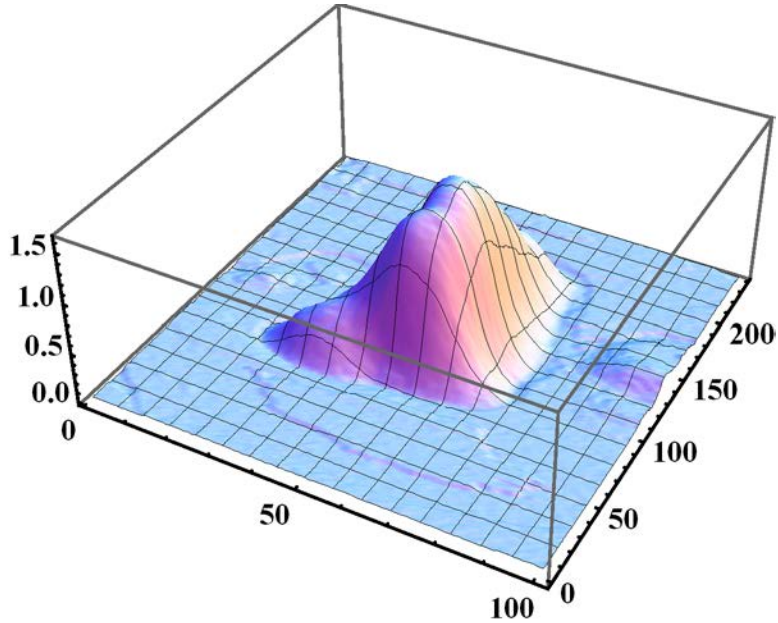
Figure B-108. 3-D Plot of |Z| Obtained from Raster Scan of 20-kHz Ferrite Core Probe over B118 in Vertical Direction at 40 kHz
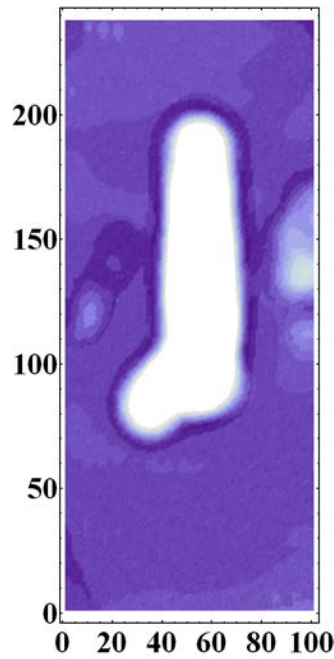
Figure B-109. Density Plot of |Z| Obtained from Raster Scan of 20-kHz Ferrite Core Probe over B118 in Vertical Direction at 50 kHz
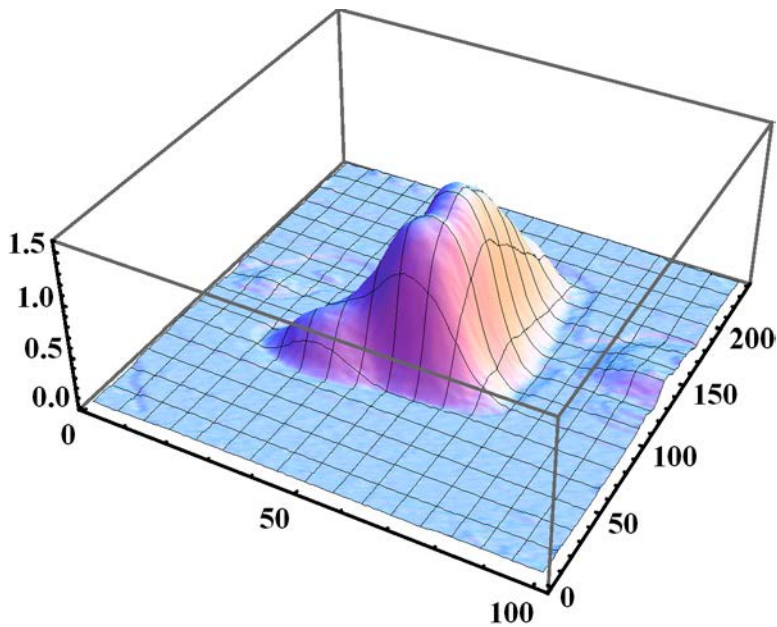

Figure B-110. 3-D Plot of |Z| Obtained from Raster Scan of 20-kHz Ferrite Core Probe over B118 in Vertical Direction at 50 kHz
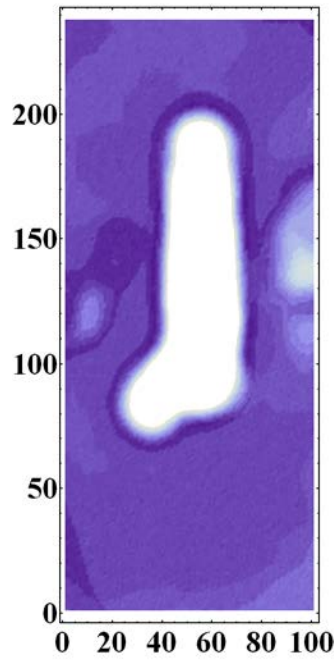
Figure B-111. Density Plot of |Z| Obtained from Raster Scan of 20-kHz Ferrite Core Probe over
B118 in Vertical Direction at 60 kHz
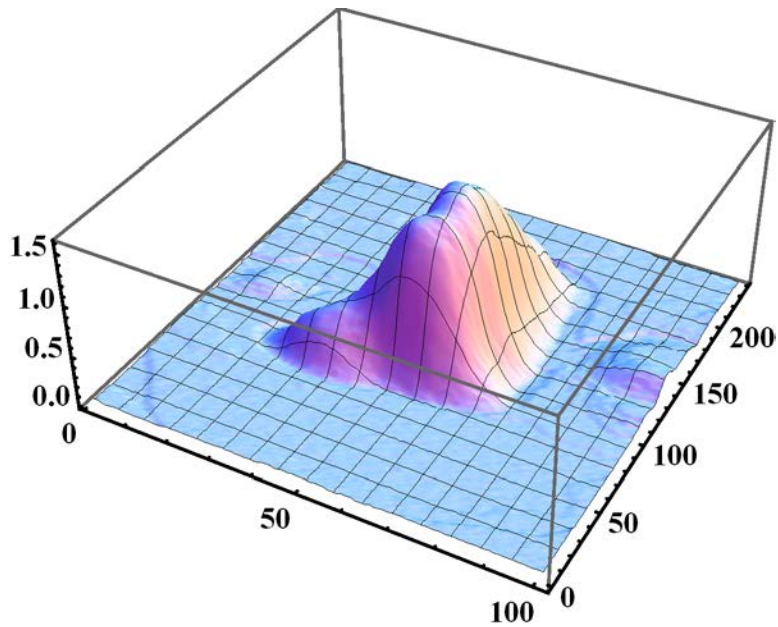
Figure B-112. 3-D Plot of |Z| Obtained from Raster Scan of 20-kHz Ferrite Core Probe over
B118 in Vertical Direction at 60 kHz
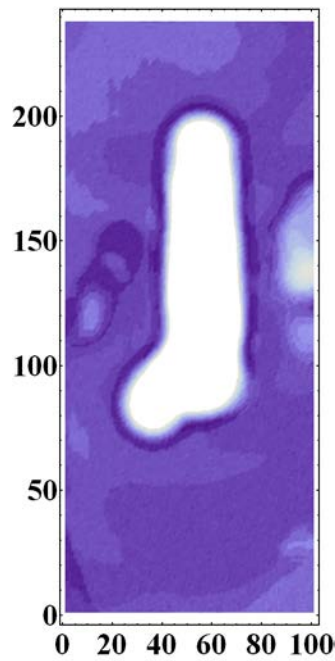
Figure B-113. Density Plot of |Z| Obtained from Raster Scan of 20-kHz Ferrite Core Probe over B118 in Vertical Direction at 70 kHz
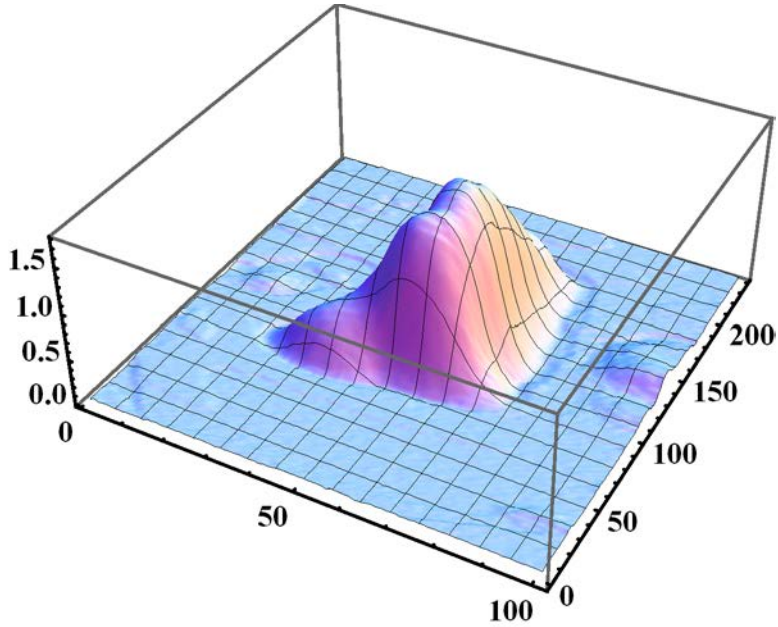
Figure B-114. 3-D Plot of |Z| Obtained from Raster Scan of 20-kHz Ferrite Core Probe over B118 in Vertical Direction at 70 kHz
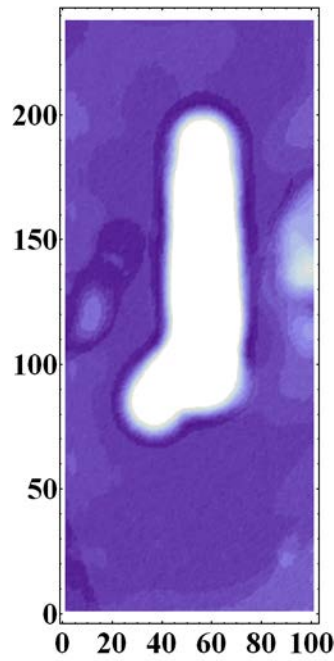
Figure B-115. Density Plot of |Z| Obtained from Raster Scan of 20-kHz Ferrite Core Probe over
            B118 in Vertical Direction at 80 kHz
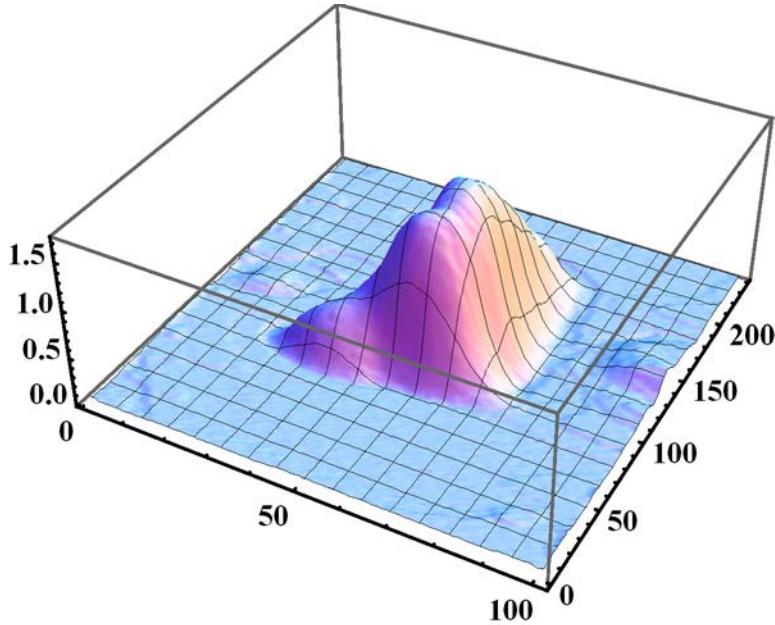
Figure B-116. 3-D Plot of |Z| Obtained from Raster Scan of 20-kHz Ferrite Core Probe over
            B118 in Vertical Direction at 80 kHz
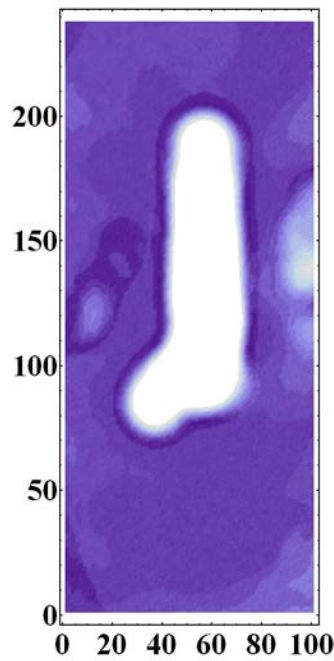
Figure B-117. Density Plot of |Z| Obtained from Raster Scan of 20-kHz Ferrite Core Probe over B118 in Vertical Direction at 90 kHz
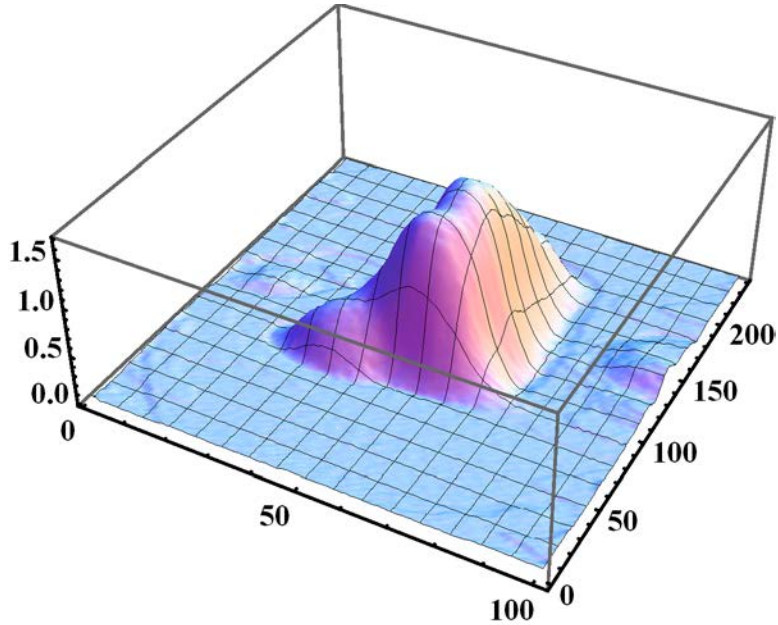

Figure B-118. 3-D Plot of |Z| Obtained from Raster Scan of 20-kHz Ferrite Core Probe over B118 in Vertical Direction at 90 kHz
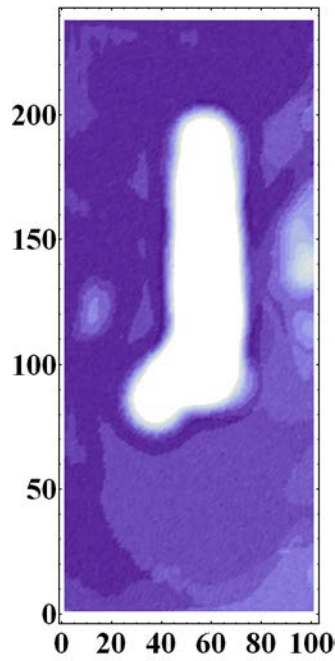
Figure B-119. Density Plot of |Z| Obtained from Raster Scan of 20-kHz Ferrite Core Probe over
B118 in Vertical Direction at 100 kHz
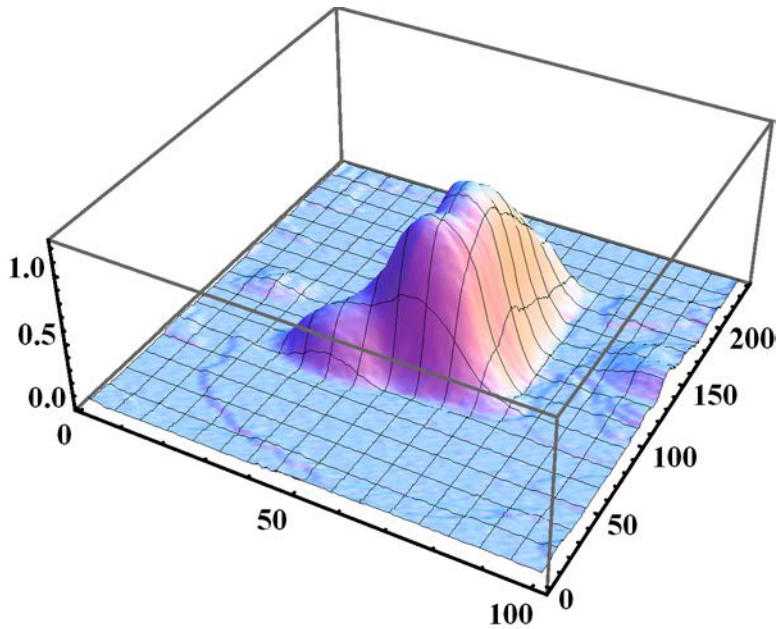
Figure B-120. 3-D Plot of |Z| Obtained from Raster Scan of 20-kHz Ferrite Core Probe over
B118 in Vertical Direction at 100 kHz